

NASA/TM-2017-219599



Simulating the Impact Response of Three Full-Scale Crash Tests of Cessna 172 Aircraft

Karen E. Jackson
Langley Research Center, Hampton, Virginia

Edwin L. Fasanella
National Institute of Aerospace, Hampton, Virginia

Justin D. Littell, Martin S. Annett and Chad M. Stimson
Langley Research Center, Hampton, Virginia

NASA STI Program . . . in Profile

Since its founding, NASA has been dedicated to the advancement of aeronautics and space science. The NASA scientific and technical information (STI) program plays a key part in helping NASA maintain this important role.

The NASA STI program operates under the auspices of the Agency Chief Information Officer. It collects, organizes, provides for archiving, and disseminates NASA's STI. The NASA STI program provides access to the NTRS Registered and its public interface, the NASA Technical Reports Server, thus providing one of the largest collections of aeronautical and space science STI in the world. Results are published in both non-NASA channels and by NASA in the NASA STI Report Series, which includes the following report types:

- **TECHNICAL PUBLICATION.** Reports of completed research or a major significant phase of research that present the results of NASA Programs and include extensive data or theoretical analysis. Includes compilations of significant scientific and technical data and information deemed to be of continuing reference value. NASA counter-part of peer-reviewed formal professional papers but has less stringent limitations on manuscript length and extent of graphic presentations.
- **TECHNICAL MEMORANDUM.** Scientific and technical findings that are preliminary or of specialized interest, e.g., quick release reports, working papers, and bibliographies that contain minimal annotation. Does not contain extensive analysis.
- **CONTRACTOR REPORT.** Scientific and technical findings by NASA-sponsored contractors and grantees.

- **CONFERENCE PUBLICATION.** Collected papers from scientific and technical conferences, symposia, seminars, or other meetings sponsored or co-sponsored by NASA.
- **SPECIAL PUBLICATION.** Scientific, technical, or historical information from NASA programs, projects, and missions, often concerned with subjects having substantial public interest.
- **TECHNICAL TRANSLATION.** English-language translations of foreign scientific and technical material pertinent to NASA's mission.

Specialized services also include organizing and publishing research results, distributing specialized research announcements and feeds, providing information desk and personal search support, and enabling data exchange services.

For more information about the NASA STI program, see the following:

- Access the NASA STI program home page at <http://www.sti.nasa.gov>
- E-mail your question to help@sti.nasa.gov
- Phone the NASA STI Information Desk at 757-864-9658
- Write to:
NASA STI Information Desk
Mail Stop 148
NASA Langley Research Center
Hampton, VA 23681-2199

NASA/TM-2017-219599



Simulating the Impact Response of Three Full-Scale Crash Tests of Cessna 172 Aircraft

Karen E. Jackson
Langley Research Center, Hampton, Virginia

Edwin L. Fasanella
National Institute of Aerospace, Hampton, Virginia

Justin D. Littell, Martin S. Annett and Chad M. Stimson
Langley Research Center, Hampton, Virginia

National Aeronautics and
Space Administration

Langley Research Center
Hampton, Virginia 23681-2199

July 2017

The use of trademarks or names of manufacturers in this report is for accurate reporting and does not constitute an official endorsement, either expressed or implied, of such products or manufacturers by the National Aeronautics and Space Administration.

Available from:

NASA STI Program / Mail Stop 148
NASA Langley Research Center
Hampton, VA 23681-2199
Fax: 757-864-6500

Table of Contents

	Page
1.0 ABSTRACT	1
2.0 INTRODUCTION	1
3.0 CRASH TEST SERIES	3
3.1 Crash Test 1	3
3.2 Crash Test 2	5
3.3 Crash Test 3	6
4.0 LS-DYNA SIMULATIONS OF THREE FULL-SCALE CRASH TESTS	8
4.1 Data Post-Processing	8
4.2 Test-Analysis Calibration Plan	9
4.3 Quasi-Static Test and Simulation of the Main Gear Strut	10
4.4 Modeling and Simulation of Test 1	11
4.4.1 Test 1 Inertial Properties	14
4.4.2 Test 1 Kinematic Assessment	15
4.4.3 Test 1 Time-History Comparisons	15
4.5 Modeling and Simulation of Test 2	23
4.5.1 Test 2 Inertial Properties	25
4.5.2 Test 2 Kinematic Assessment	25
4.5.3 Test 2 Soil Deformation	25
4.5.4 Test 2 Time-History Comparisons	25
4.6 Modeling and Simulation of Test 3	34
4.6.1 Test 3 Inertial Properties	35
4.6.2 Test 3 Kinematic Assessment	36
4.6.3 Test 3 Soil Deformation	37
4.6.4 Test 3 Time-History Comparisons	37
5.0 DISCUSSION OF RESULTS	52
5.1 Modeling Uncertainty	52
5.2 Modeling Calibration of Time History Responses	53
6.0 CONCLUSIONS	54
7.0 ACKNOWLEDGEMENTS	56
8.0 REFERNCES	56
APPENDIX A	59

List of Figures

	Page
Figure 1. Photographs of the three C-172 aircraft obtained for crash testing.	2
Figure 2. Pre-test photograph of C-172 crash Test 1.	3
Figure 3. Test 1 ELT configuration.	4
Figure 4. Post-test photograph.	4
Figure 5. Pre-test photograph of C-172 crash Test 2 airplane at impact attitude.	5
Figure 6. ELT configuration for Test 2.	6
Figure 7. Time sequence of events for Test 2.	6
Figure 8. Photo showing the Test 3 aircraft and highlighting configuration changes.	7
Figure 9. ELT configuration for Test 3.	7
Figure 10. Impact sequence for Test 3.	8
Figure 11. Pilot floor acceleration time histories from Test 1.	9
Figure 12. Integrated raw and filtered acceleration data.	9
Figure 13. Quasi-static loading test of C-172 main gear strut.	10
Figure 14. Results of quasi-static test and simulation of the main gear strut.	11
Figure 15. Model representing the Test 1 configuration, shown without the impact surface.	12
Figure 16. Cutaway views of the Test 1 model.	12
Figure 17. Cessna 172 nose gear.	13
Figure 18. Main gear model.	13
Figure 19. Time sequence of events comparison.	16
Figure 20. Test-analysis comparison of acceleration and velocity responses for the pilot floor.	17
Figure 21. Test-analysis comparison of acceleration and velocity responses for the copilot floor.	17
Figure 22. Comparisons of acceleration and velocity responses for the left doorframe.	18
Figure 23. Comparisons of acceleration and velocity responses for the right doorframe.	18

List of Figures (Continued)

	Page
Figure 24. Comparisons of acceleration and velocity responses for the DAS box/floor.	19
Figure 25. Comparisons of acceleration and velocity responses for the tail.	19
Figure 26. Test-analysis vertical acceleration and velocity responses of the left floor ELT.	20
Figure 27. Test-analysis vertical acceleration and velocity responses of the right floor ELT.	20
Figure 28. Test-analysis vertical acceleration and velocity responses of the left sidewall ELT.	21
Figure 29. Test-analysis vertical acceleration and velocity responses of the right sidewall ELT.	21
Figure 30. Test velocity response of the CG, as measured by photogrammetry, compared with the predicted velocity responses of the DAS box and the rear center ceiling support beam.	23
Figure 31. LS-DYNA model representing the Test 2 configuration.	24
Figure 32. Comparison of time sequence of events for Test 2.	26
Figure 33. Measured and predicted soil deformations for Test 2.	27
Figure 34. Forward and vertical accelerations on floor near pilot.	28
Figure 35. Forward and vertical accelerations on the floor near copilot.	28
Figure 36. Forward and vertical acceleration comparisons of the DAS Box.	29
Figure 37. Forward and vertical acceleration comparisons of the left doorframe.	29
Figure 38. Forward and vertical acceleration comparisons of the right doorframe.	30
Figure 39. Forward and vertical acceleration comparisons near the aircraft tail.	30
Figure 40. Test-analysis comparison of ELT1 forward acceleration responses for Test 2.	31
Figure 41. Test-analysis comparison of ELT2 forward and vertical acceleration responses for Test 2.	31
Figure 42. Test-analysis comparison of ELT3 forward and vertical acceleration responses for Test 2.	31
Figure 43. Test-analysis comparisons of ELT4 forward and vertical acceleration responses for Test 2.	32

List of Figures (Continued)

	Page
Figure 44. Test-analysis comparisons of ELT5 forward and vertical acceleration responses for Test 2.	32
Figure 45. Comparison of predicted global velocities at pilot floor location with photogrammetry.	33
Figure 46. Test 3 aircraft model.	35
Figure 47. Comparison of time sequence of events for Test 3.	36
Figure 48. Soil deformation pattern for Test 3.	37
Figure 49. Comparison of vertical and forward acceleration and velocity responses of the pilot floor in Test 3.	38
Figure 50. Comparison of vertical and forward acceleration and velocity responses of the copilot floor in Test 3.	39
Figure 51. Comparison of vertical and forward acceleration and velocity responses of the DAS box in Test 3.	40
Figure 52. Comparison of vertical and forward acceleration and velocity responses of the left doorframe in Test 3.	41
Figure 53. Comparison of vertical and forward acceleration and velocity responses of the right doorframe in Test 3.	42
Figure 54. Comparison of vertical and forward acceleration and velocity responses of the tail in Test 3.	43
Figure 55. Comparison of vertical and forward acceleration and velocity responses of the left floor ELT1 in Test 3.	44
Figure 56. Comparison of vertical and forward acceleration and velocity responses of the right aft sidewall ELT2 in Test 3.	45
Figure 57. Comparison of vertical and forward acceleration and velocity responses of the right forward sidewall ELT3 in Test 3.	46
Figure 58. Comparison of vertical and forward acceleration and velocity responses of the left aft sidewall ELT4 in Test 3.	47
Figure 59. Comparison of vertical and forward acceleration and velocity responses of the right floor ELT5 in Test 3.	48
Figure 60. Locations where 3-D photogramtry data were collected and analyzed.	50

List of Figures (Concluded)

	Page
Figure 61. Test-analysis comparisons of forward and vertical velocity responses of the doorframe.	51
Figure 62. Test-analysis comparisons of forward and vertical velocity responses of the tail.	51
Figure 63. DAS box instrumentation and nodal output comparisons.	53

List of Tables

	Page
Table 1. Material properties used in the airframe models.	14
Table 2. Test-analysis comparison of inertial properties for Test 1.	15
Table 3. Summary of test-analysis comparison metrics for Test 1.	22
Table 4. Test-analysis comparison of inertial properties for Test 2.	25
Table 5. Comparisons of test and model soil deformations for Test 2.	27
Table 6. Summary of test-analysis comparison metrics for Test 2.	33
Table 7. Test-analysis comparison of inertial properties for Test 3.	36
Table 8. Test-analysis comparison of Test 3 soil depths and track distances.	37
Table 9. Summary of test-analysis comparison metrics for Test 3.	49

List of Acronyms

3-D – Three dimensional
ANOVA – Analysis of Variance
ATD – Anthropomorphic Test Device
C-172 – Cessna 172 aircraft
CFC – Channel Filter Class
CFIT – Controlled Flight Into Terrain
CG – Center of Gravity
CNRB – Constrained Nodal Rigid Body
DAS – Data Acquisition System
delta-V – Change in velocity
ELT – Emergency Locator Transmitter
ELTSAR – Emergency Locator Transmitter Survivability and Reliability
ft – unit of length, foot or feet
g – unit of acceleration, ratio of measured or predicted acceleration to the acceleration of gravity
GA – General Aviation
GSFC - Goddard Space Flight Center
GUS – Gantry Unwashed Sand
Hz – unit of frequency, Hertz
in – unit of length, inch
LandIR – Landing and Impact Research
LaRC - Langley Research Center
lb – unit of force, pound
MCP – Model Calibration Plan
MPC – Magnitude-Phase-Comprehensive
NASA – National Aeronautics and Space Administration
RSVVP - Roadside Safety Verification and Validation Program
s – unit of time, second
SAE – Society of Automotive Engineers
SAR – Search and Rescue
SGC – Sprague and Geers Comprehensive
SGM – Sprague and Geers Magnitude
SGP – Sprague and Geers Phase
SMP – Shared Memory Parallelism
SPC – Single Point Constraint
US – United States

Simulating the Impact Response of Three Full-Scale Crash Tests of Cessna 172 Aircraft

Karen E. Jackson
NASA Langley Research Center
Hampton, VA 23681-2199

Edwin L. Fasanella
National Institute of Aerospace
Hampton, VA 23666

Justin D. Littell, Martin S. Annett, and Chad M. Stimson
NASA Langley Research Center
Hampton, VA 23681-2199

1.0 ABSTRACT

During the summer of 2015, a series of three full-scale crash tests were performed at the Landing and Impact Research Facility located at NASA Langley Research Center of Cessna 172 aircraft. The first test (Test 1) represented a flare-to-stall emergency or hard landing onto a rigid surface. The second test (Test 2) represented a controlled-flight-into-terrain (CFIT) with a nose down pitch attitude of the aircraft, which impacted onto soft soil. The third test (Test 3) also represented a CFIT with a nose up pitch attitude of the aircraft, which resulted in a tail strike condition. Test 3 was also conducted onto soft soil. These crash tests were performed for the purpose of evaluating the performance of Emergency Locator Transmitters and to generate impact test data for model calibration. Finite element models were generated and impact analyses were conducted to simulate the three impact conditions using the commercial nonlinear, transient dynamic finite element code, LS-DYNA[®]. The objective of this paper is to summarize test-analysis results for the three full-scale crash tests.

2.0 INTRODUCTION

The NASA Search and Rescue (SAR) Mission Office, located at NASA Goddard Space Flight Center (GSFC), initiated a study in 2013 with goals of collecting data for use in updating performance standards for the next generation of Emergency Locator Transmitters (ELTs) [1-6]. After a series of component and subsystem-level environmental tests in 2014, a series of three severe, but potentially survivable, full-scale crash tests of Cessna 172 (C-172) aircraft were performed at the Landing and Impact Research Facility (LandIR), located at NASA Langley Research Center (LaRC) in the summer of 2015. The first test represented a flare-to-stall emergency or hard landing onto a rigid surface. The second test represented a controlled-flight-into-terrain (CFIT) with a nose down pitch attitude of the aircraft, which impacted onto soft soil. The third test also represented a CFIT with a nose up pitch attitude of the aircraft, which resulted in an initial tail strike condition. Test 3 was also conducted onto soft soil. These crash tests were performed for the purpose of evaluating the system performance of ELTs and to generate impact test data for model calibration. Finite element models were generated using the commercial nonlinear, transient dynamic finite element code, LS-DYNA [7, 8] to simulate the three test conditions. Once calibrated, the models were then used to assess ELT responses under a variety of impact conditions not feasible for testing within resource constraints. Several of these simulations are documented in Appendix A. The main focus of this paper is to summarize test-analysis results for the three full-scale crash tests.

The crash test series conducted in the summer of 2015 generated data for use in updating the performance specifications for the next generation of ELT systems. ELT systems are present on all General Aviation (GA) aircraft and are intended for use in an emergency situation, such as a crash landing. The ELT system is designed to automatically sense a crash event and to transmit a distress signal to SAR personnel, who are dispatched to provide assistance. ELT systems must be designed to work in a wide range of scenarios; consequently, three different impact conditions were selected for the crash tests at the LandIR facility. Each of the C-172 test articles contained 4 or 5 individual ELTs that were mounted throughout the interior of the airframe prior to the crash tests.

The Cessna 172 Skyhawk is a four-seat, single engine, high-wing airplane, manufactured by the Cessna Aircraft Company [9]. More Cessna 172s have been built than any other aircraft, and the first production models were delivered in 1956 [10]. As of 2015, Cessna, and its partners, have built more than 43,000 airframes. The wide availability of these aircraft was one reason that they were selected for the test series. A second reason for the selection was that research showed no correlation between airplane make or model and ELT performance [1], indicating that the C-172 was as likely a candidate for the test series as any other aircraft. It is also noted that NASA had previously conducted a series of crash tests using C-172 aircraft in the 1970's [11-13] and these tests helped to guide the development of the lifting hardware used in the current tests.

Photographs of the three aircraft that were obtained for crash testing are shown in Figure 1. Test article one was a 1958 C-172, which was current on its annual inspection. Test article two was a 1958 C-175, which is the C-172 airframe, but contains a different engine and gearbox. The third test article was a 1974 C-172M, which was also current on its annual inspection. Test articles 1 and 3 were flying as late as the winter of 2014, before being transported to NASA LaRC for use as crash test articles.



Figure 1. Photographs of the three C-172 aircraft obtained for crash testing.

This paper will provide a brief description of each full-scale crash test, a summary of the finite element model development for each test, and test-analysis comparisons in several categories including inertial properties, kinematic assessment, soil deformation (where applicable), and acceleration- and velocity-time history responses for airframe structural and ELT locations. Appendix A provides results of simulations performed following model calibration to examine a variety of impact conditions not feasible for testing within programmatic resource constraints. This work was conducted under the Emergency Locator Transmitter Survivability and Reliability (ELTSAR) Study at NASA LaRC, which was sponsored by SAR at NASA GSFC.

3.0 CRASH TEST SERIES

Descriptions of the three full-scale crash tests are summarized in this section of the paper. The impact conditions for each test are provided, as well as a summary of kinematic responses and damage. For additional information, please see References 1- 6.

3.1 Crash Test 1

The first full-scale crash test of a C-172 aircraft (Test 1) was performed on July 1, 2015. A pre-test photograph of the C-172 aircraft used in Test 1 is shown in Figure 2. The aircraft contained two crew seats, two Hybrid II 50th percentile Anthropomorphic Test Devices (ATDs), an onboard data acquisition system (DAS) box, four ELTs that were mounted throughout the cabin and tail of the aircraft, and ballast weights to represent fuel loading in the wings. The locations of the ELTs installed onboard the Test 1 aircraft are shown in Figure 3. The total weight of the aircraft was approximately 2,000-lb. The left side of the aircraft was painted white and 1-in.-diameter black dots were added to provide a stochastic speckle pattern for the purpose of collecting three-dimensional (3-D) photogrammetry data during the test [6]. Sixty-four channels of data were collected at 10,000 samples per second using the onboard DAS. The DAS was located behind the pilot and co-pilot seats in the location where luggage would normally be stored, or passenger seats could be added. Thus, the DAS provided ballast to the airframe. Additional lead weight was added over the wing to simulate fuel weight. The lead, along with the main swing hardware accounted for approximately 100 lb of weight over each wing, which simulated fuel tanks above 75% full. Finally, onboard and external high-speed video coverage was obtained from internal and exterior cameras.



Figure 2. Pre-test photograph of C-172 crash Test 1.

The LandIR facility is used to conduct full-scale crash tests of aircraft using either a single (which introduces a pitch rate) or parallel (which removes the pitch rate) swing cabling system. For Test 1, a single set of swing cables was connected to the west end of the LandIR facility and was attached to hard points on the aircraft. Pullback cables were connected on one end to a movable overhead bridge located on the east side of the LandIR facility and on the other end to the test article. As the pullback cables are retracted using the bridge winch system, the aircraft is lifted into the air to a pre-determined drop height. Following a countdown, a pyrotechnic cutter severs the pullback cables, causing the test article to swing along a pendulum-like flight path from east to west onto a pre-determined impact location on the ground. Just prior to impact, the swing cables are pyrotechnically separated allowing the aircraft to impact the surface in a free (unconstrained) condition. Various combinations of swing cable length, impact location, drop height, impact surface conditions (rigid, soil or water) along with a test article's attitude can be prescribed, creating a wide

variety of impact conditions. Measured impact conditions for Test 1 were: forward velocity was 722.4-in/s (60.2-ft/s), vertical velocity was 276-in/s (23.0-ft/s), pitch rate was +16.5-degrees/s, and pitch attitude was 1.48° (nose up).

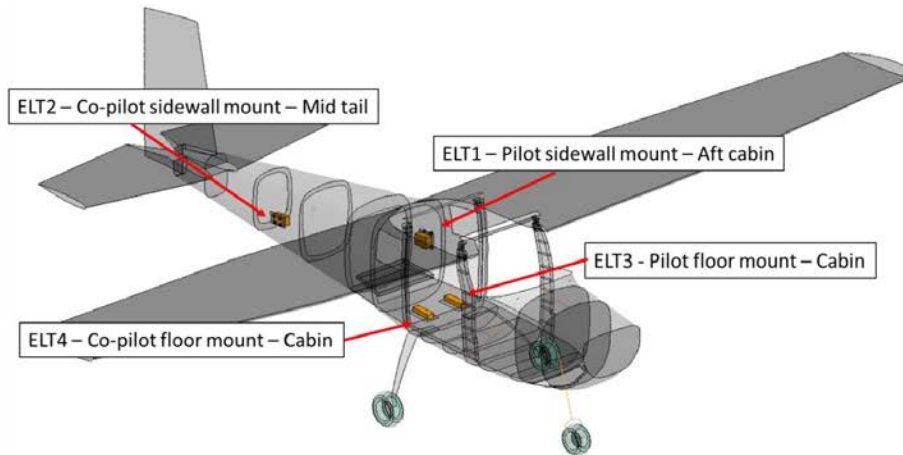


Figure 3. Test 1 ELT configuration.

Test 1 essentially represented a “hard” landing. Initially the nose gear tire impacted the concrete, followed closely by impact of the main gear tires. The main landing gear spread outward, as the nose gear stroked vertically. The only fuselage contact with the concrete surface was a slight impact of the rearmost portion of the lower tail. After this impact, the airframe rebounded upward. At 0.5-s following initial impact, the aircraft hit a net that was setup to limit forward travel of the aircraft. Some damage to the engine cowling and nose gear support structure was evident. Likely the engine cowling damage was caused by contact with the net straps. Damage to the nose gear support structure occurred during initial impact. However, following the test, the aircraft was rolled back to the storage facility using the nose and main landing gear tires, which were still inflated. A post-test photograph of the test article is shown in Figure 4. Evidence of damage to the wing caused by contact with the net can also be observed. It became apparent following Test 1 that capturing the behavior of the nose and main landing gear was essential to achieving accurate prediction of the airframe dynamic response. Consequently, landing gear component tests were conducted, as described in a later section of the paper.

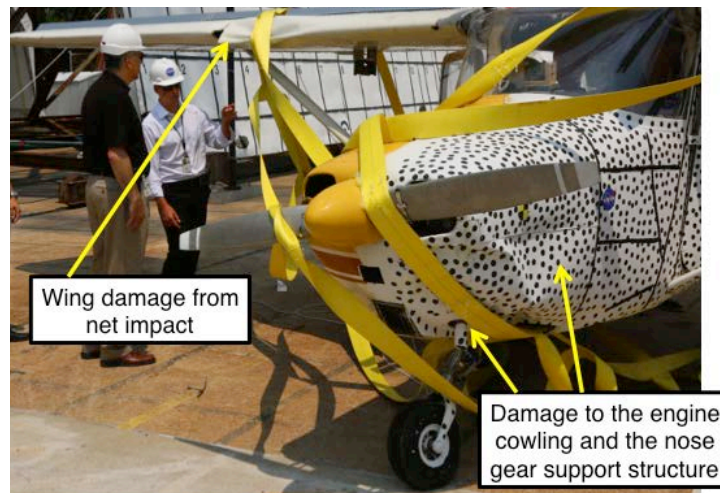


Figure 4. Post-test photograph.

3.2 Crash Test 2

A pre-test photograph of the C-172 aircraft for Test 2, nose down impact onto soil, is shown in Figure 5. The aircraft contained two crew seats, two ATDs, an onboard DAS box, five ELTs that were mounted throughout the cabin (see Figure 6), and ballast weights to represent fuel loading in the wings. The total weight of the aircraft was approximately 2,114-lb. The left side of the aircraft was painted white, with 1-in.-diameter black dots added to provide a speckle pattern for the purpose of collecting 3-D photogrammetry data during the test [6]. Sixty-four channels of data were collected at 10,000 samples per second using the onboard DAS. The DAS was located behind the pilot and co-pilot seats in the location where luggage would normally be stored, or passenger seats could be added. Thus, the DAS provided ballast to the airframe. Additional lead weight was added over the wing to simulate fuel. The lead, along with the main swing hardware, accounted for approximately 100 lb of weight over each wing, which simulated fuel tanks above 75% full. Onboard and external high-speed video coverage was obtained from internal and exterior cameras.

Prior to the impact test, the nose gear oleo-pneumatic strut was found to leak. Following unsuccessful attempts to repair the strut, the gear was locked into place at the innermost, fully deflected position. Finally, a 2-ft. high soil bed was spread above the concrete surface. The soil was a sand/clay mixture that was wetted one hour before the test. Details of the swing-cable methodology used for the crash test are provided in Reference 3. As in many high-wing crash tests into soft soil, the airplane flipped over and landed upside down at the end of the impact event, as shown in the test sequence of Figure 7. Also, the tail of the fuselage buckled early in the crash. Buckling initiated behind the bulkhead at the end of the floor, and by 0.240-s the buckle was fully formed.



Figure 5. Pre-test photograph of C-172 crash Test 2 aircraft at impact attitude.

Test 2 occurred on July 29, 2015, only four weeks following Test 1. The airplane Center-of-Gravity (CG) impacted the soil with a resultant velocity of 892.3-in/s (74.4-ft/s), consisting of 823.2-in/s (68.6-ft/s) forward and 344.4-in/s (28.7-ft/s) vertical velocity components. The impact attitude was 12.2° nose down with a pitch rate of +16.1 degrees/s. The airplane nose gear impacted the soil first, and then proceeded to immediately start plowing. After 0.111-s the left wing separated away from the fuselage, and 0.169-s after impact, buckling initiated in the tail near the station 108 frame section. The airplane started to flip over 0.240-s after the initial impact. At some point during the flip, the nose gear broke away from the nose section of the airplane. At 1.976-s after the impact, the airplane orientation was upside-down. The airplane rocked back and forth for a few seconds before finally coming to rest 6.790-s after impact. Figure 7 illustrates the impact sequence.

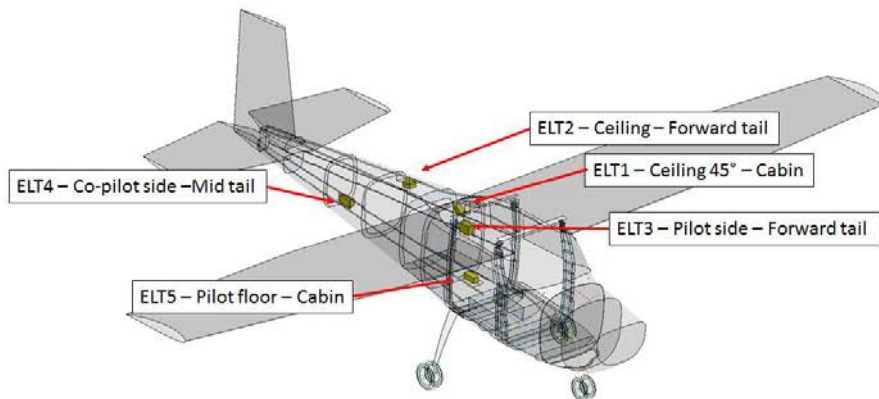


Figure 6. ELT configuration for Test 2.

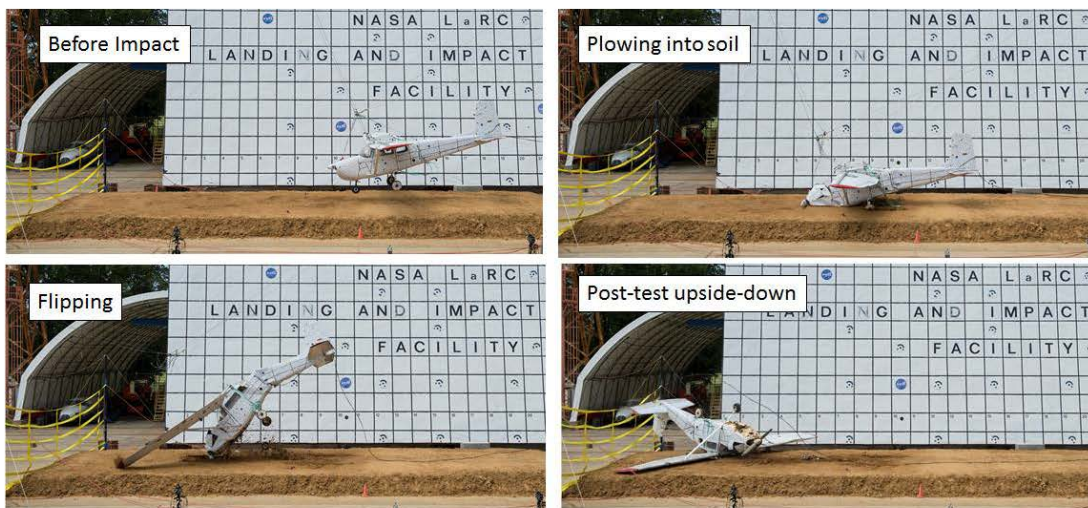


Figure 7. Time sequence of events for Test 2.

3.3 Crash Test 3

The Test 3 aircraft had a different configuration than the Test 1 and Test 2 airframes. The most noticeable difference was that the Test 3 aircraft had a swept tail, rather than the straight tail seen in the Test 1 and 2 airframes. The Test 3 aircraft also contained a rear window that was not included in the previous airframe designs. Finally, another difference was that the main landing gear in the Test 3 article consisted of tubular steel design, rather than the leaf spring configuration seen in the Test 1 and Test 2 aircraft. These changes are highlighted in Figure 8.

The Test 3 aircraft was equipped with two standard crew seats, two ATDs, an onboard DAS box, five ELTs that were mounted throughout the cabin (see Figure 9), and ballast weights to represent fuel loading in the wings. The total weight of the aircraft was approximately 2,072-lb. The left side of the aircraft was painted white, with 1-in.-diameter black dots added to provide a speckle pattern for the purpose of collecting 3-D photogrammetry data during the test [6]. Sixty-four channels of data were collected at 10,000 samples per second using the onboard DAS. The DAS was located behind the pilot and co-pilot seats in the location where luggage would normally be stored. Thus, the DAS provided ballast to the airframe. Additional lead weight was added over the wing to simulate fuel. The lead, along with the main swing hardware, accounted for approximately 100 lb of weight over each wing, which simulated fuel tanks above 75% full.

Test 3 occurred on August 26, 2015, only four weeks following Test 2. The airplane CG impacted the soil with a resultant velocity of 739.2-in/s (61.6-ft/s), consisting of 682.8-in/s (56.9-ft/s) forward and 283.2-in/s (23.6-ft/s) vertical velocity components. The pitch attitude at impact was 8.0° (nose up) with a pitch rate of 13.3 degrees/s. There was a slight amount of roll (right side high) and yaw (nose left) at impact. Due to these conditions, the pilot main gear impacted the soil initially. The tail contacted the soil 0.030-s after initial gear impact and the nose contacted the surface 0.116-s after impact. Similar to Test 2, the nose gear penetrated the soil surface and acted as a pivot point for the airplane to rotate around. The airplane started to exhibit noticeable rotation shortly after nose contact. At 0.138-s after impact, tail failure occurred behind the rear window, causing a large fracture at the tail-cabin junction to appear. The airplane landed upside-down 1.53-s after impact and rocked back and forth for an additional 3 seconds. The airplane came to rest approximately 5-s after initial impact. This sequence is depicted in Figure 10.

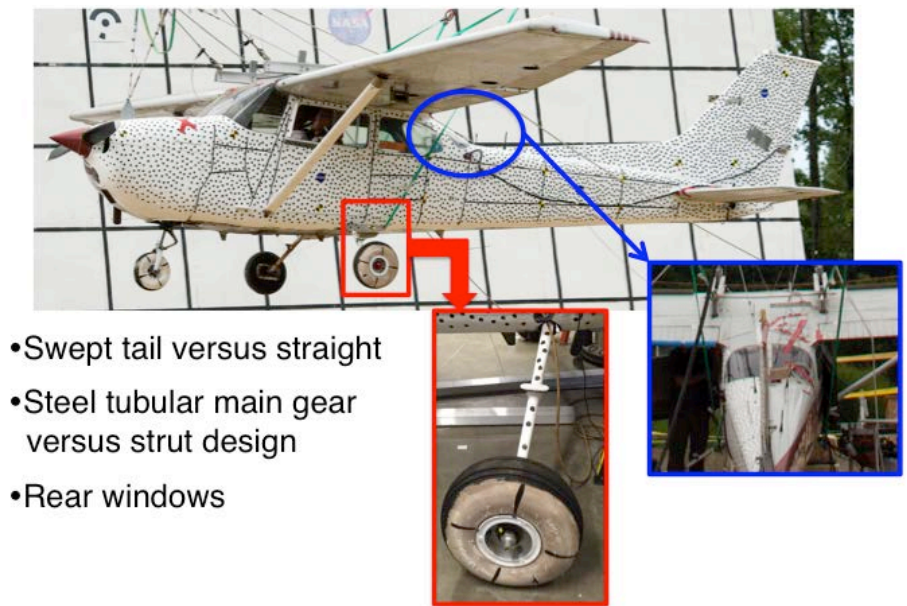


Figure 8. Photo showing the Test 3 aircraft and highlighting configuration changes.

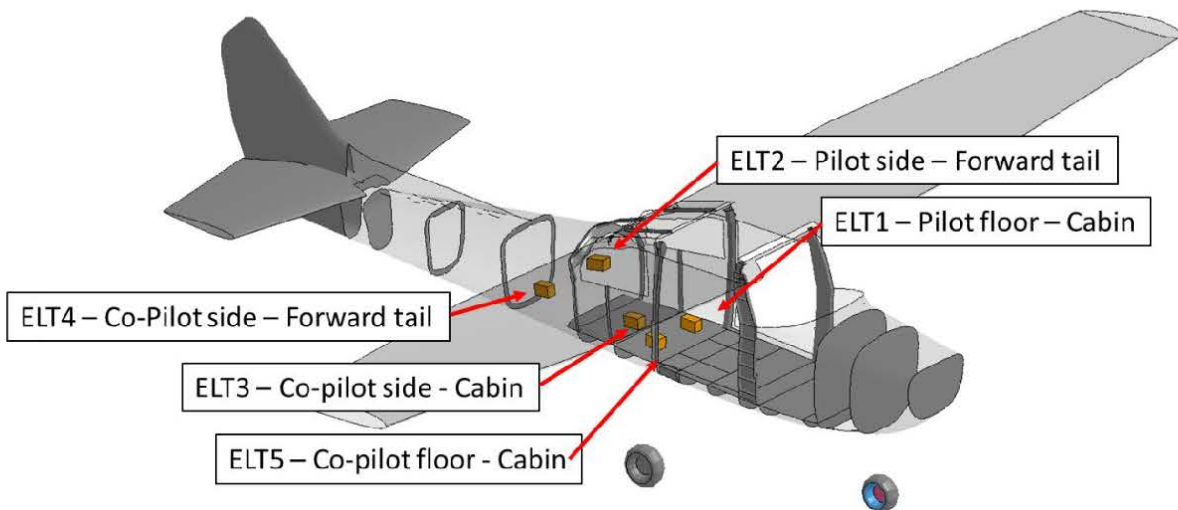


Figure 9. ELT configuration for Test 3.

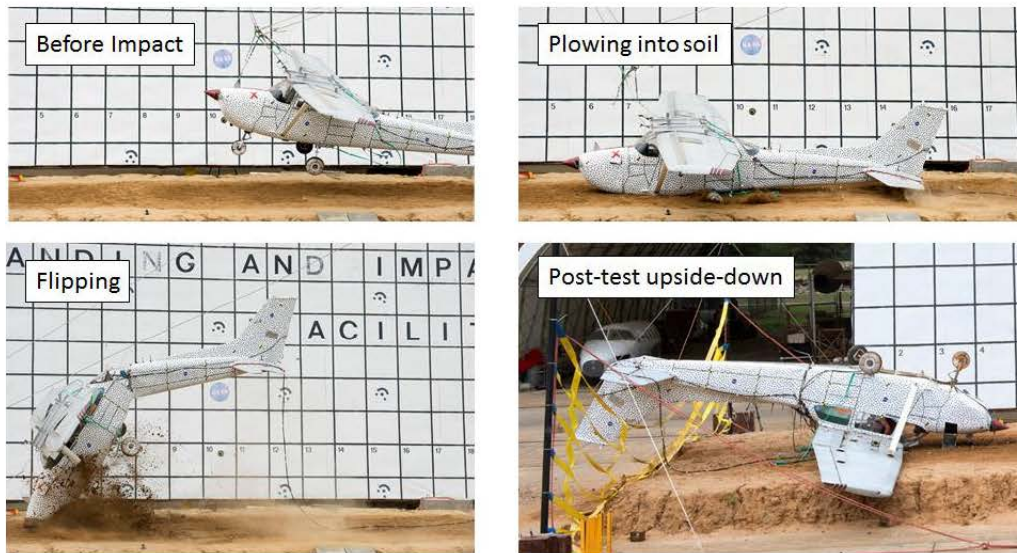


Figure 10. Test 3 sequence of events.

4.0 LS-DYNA SIMULATIONS OF THREE FULL-SCALE CRASH TESTS

Development of the LS-DYNA finite element models was complicated by the fact that no prior geometry or static loads models of the C-172 airframe existed and no engineering drawings were available. The original model was generated using a 3-D laser scan of the test article. The resulting point cloud of the outer mold line was used to tune the baseline geometry model. Extensive hand measurements, plus references to the maintenance manual [9], were required to define the internal structural geometry. The final geometry model was discretized into a finite element model. Note that a consistent set of units for length, force, and time (in-lb-s) was used in each model. In the next sections of the paper, the finite element model development for each test is described followed by test-analysis comparisons made in several categories including: inertial properties, kinematic assessment of the time sequence of events, soil deformation (for Test 2 and Test 3 only), and time-history responses. Prior to presenting these results, it is useful to describe data post-processing, or filtering, and to define the test-analysis calibration metrics established by the ELTSAR management team.

4.1 Data Post-Processing

Following each of the three full-scale crash tests, the test data were evaluated for quality using the procedures described in the Appendix of Reference 14. Prior to generating time-history response plots, both the experimental and analytical acceleration data had to be filtered. As an example, three plots of the pilot floor acceleration time-history responses from Test 1 are shown in Figure 11. The data were collected at 10,000 samples per second. It is obvious that the raw test data, plotted in Figure 11(a), contains high-frequency oscillations that obscure the underlying crash pulse. Next, the raw test data is filtered using a Society of Automotive Engineers (SAE) Channel Filter Class (CFC) 60-Hz low-pass filter [15], which is commonly used to filter crash test data. The underlying crash pulse is now visible, as shown in Figure 11(b); however, many oscillations still exist in the data. For this reason, the raw acceleration data were filtered using an SAE CFC20 low-pass filter. Now, the fundamental acceleration pulse is evident, without distracting oscillations, as shown in Figure 11(c).

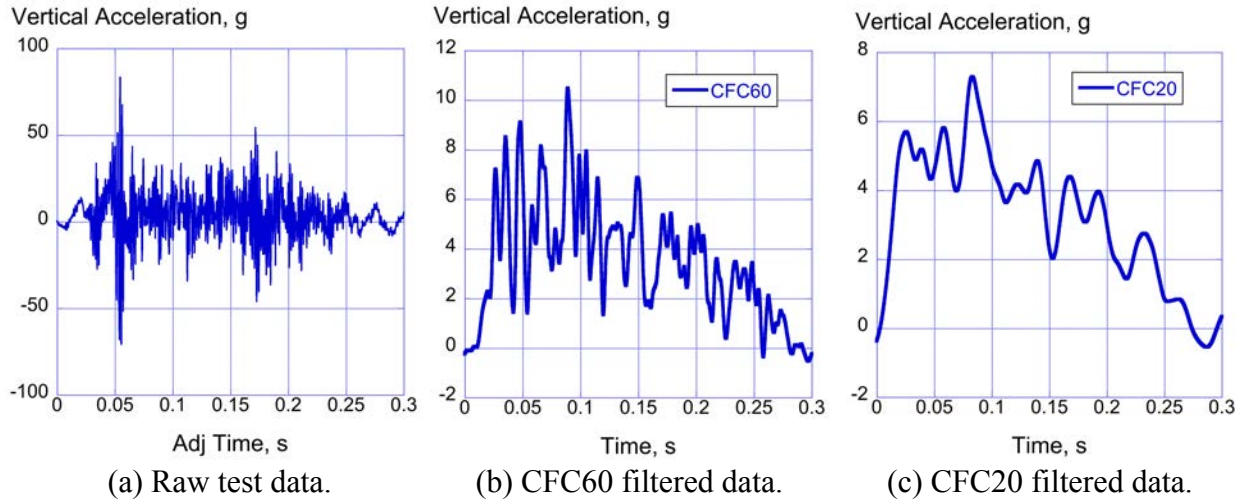


Figure 11. Pilot floor acceleration time histories from Test 1.

Often the process of filtering can distort acceleration data. It is always a good check to compare the integrated raw acceleration data (velocity) with the integrated filtered acceleration data. As an example, each of the data plots shown in Figure 11 were integrated and the results are plotted in Figure 12. Each of the integrated acceleration curves provides an identical response. These results show that the SAE CFC20 filter does not alter the underlying response and is, therefore, an appropriate filter for this application. Consequently, all acceleration data presented in this paper were filtered using an SAE CFC20 low-pass filter [15].

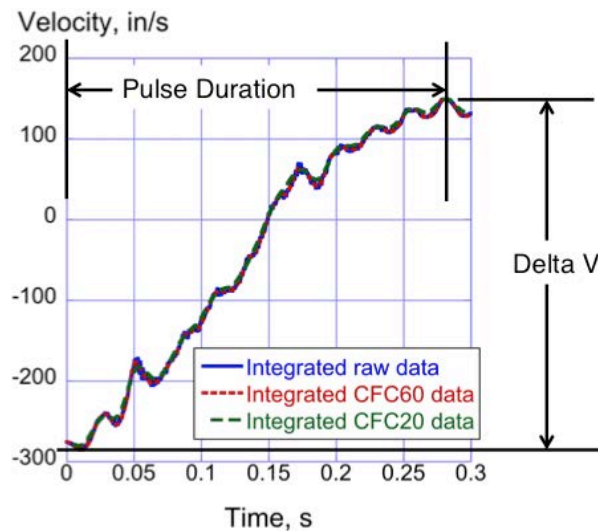


Figure 12. Integrated raw and filtered acceleration data.

4.2 Test-Analysis Calibration Plan

As part of the ELTSAR Study, a Peer Review was conducted in the Fall 2015 to assess progress in model development and calibration. One recommendation of the Peer Review Committee was to generate a Model Calibration Plan (MCP) that contained specific metrics. The MCP recommended a multi-step process. The first step involved model checkout and included a test-analysis

comparison of inertial properties. The second step required a comparison of test and model kinematics. During this check, the overall behavior of the model is compared with the test, including items such as pulse duration, stopping distance and crater depth in soil, time sequence of events, and rebound. The next step is to check major failure locations. Does the model predict failure, matching the amount of damage, and the location and time that it occurs? Finally, the last step involved detailed quantitative comparison of time history responses. Numerous metrics could be applied; however, the ELTSAR management team recommended a comparison of average acceleration, pulse duration, and change in velocity (delta-V) for selected data channels. Note that the pulse duration and delta-V parameters are identified in Figure 12. For this test-analysis calibration effort, the vertical pulse duration is defined as the time of maximum rebound velocity minus the initial time of impact. Most often, the forward pulse duration corresponds to the vertical pulse duration. The vertical delta-V parameter is defined as the maximum rebound velocity minus the initial velocity. These metrics, along with average accelerations, are tabulated for each test and simulation and the level of agreement is assessed based on percentage differences. In general, agreement within $\pm 10\%$ is considered excellent, within $\pm 20\%$ is good, and differences over $\pm 20\%$ indicate that model improvements are needed. Note that average accelerations were used since the primary interest was in characterizing the “typical” crash environments experienced at ELT locations. In contrast, peak acceleration values are subject to local dynamics that may vary widely at different locations. The channels chosen for test-analysis comparisons were selected because they represent prospective ELT locations and other end-to-end hard points on the airframe that help characterize the overall response.

4.3 Quasi-Static Test and Simulation of the Main Gear Strut

Based on test kinematic responses, it became apparent that the success of the simulation effort for Tests 1 and 2 depended in large measure on accurate prediction of the response of the main gear. Consequently, a separate set of main gear struts was purchased and a quasi-static loading test was performed. A photograph of the test set-up is depicted in Figure 13(a). The top end of the strut was fixed to a back-stop, while the bottom end was loaded vertically using a jack. The surface of the strut was painted with a speckle pattern to capture fringe plots of displacement. During the test, applied force and displacement were recorded. A finite element model was developed of the main gear strut, as shown in Figure 13(b).

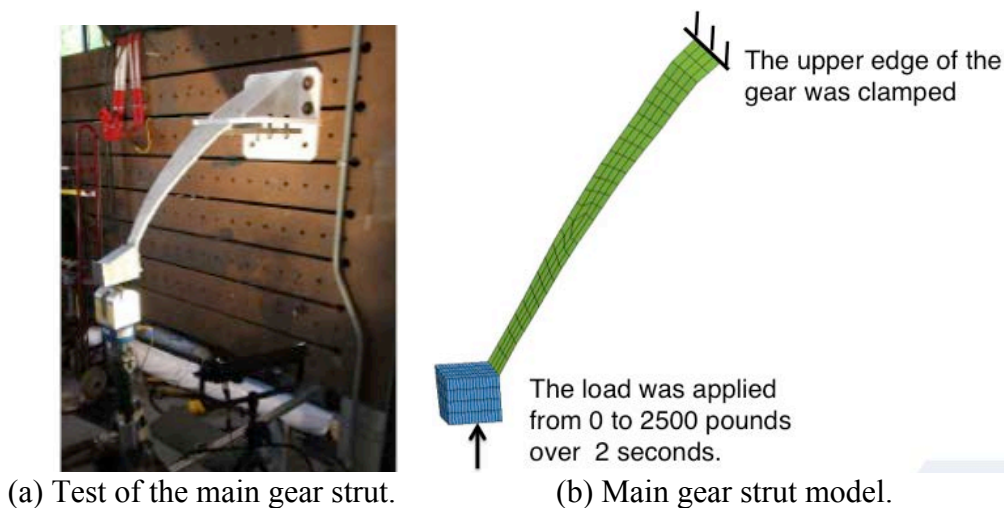


Figure 13. Quasi-static loading test of C-172 main gear strut.

In the model, the nodes forming the upper end of the strut were fixed and the bottom nodes were free to move horizontally. The block attached to the bottom of the strut was given a defined vertical load ranging from 0- to 2500-lb over a 2-s time duration. Results of the quasi-static test are shown in Figure 14. A contour plot of vertical displacement at a load of 2500-lb is shown in Figure 14(a). A fringe plot of predicted vertical displacement at a load of 2500-lb is shown in Figure 14(b). These two plots are similar and indicate a maximum vertical displacement of 2.87-in. for the test and a maximum of 2.96-in. for the model. These results verify that the elastic modulus of the material model representing spring steel is correct at 3.0E07-psi. Unfortunately, the testing did not continue into the plastic regime allowing determination of the yield stress, strain hardening modulus, or failure strain. As a result, handbook values for these parameters were used in the model.

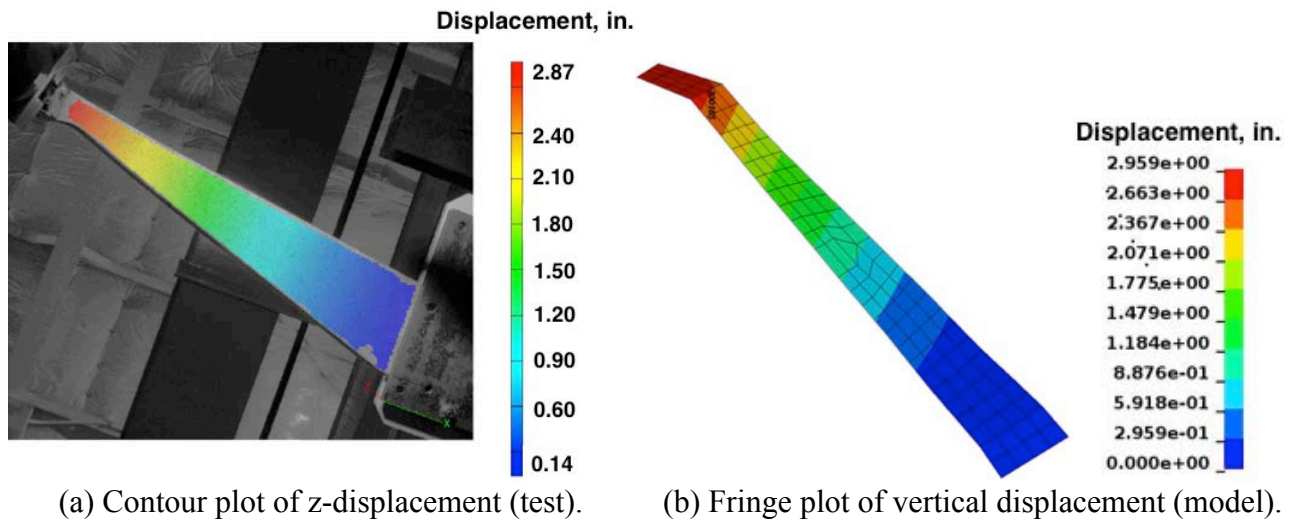


Figure 14. Results of quasi-static test and simulation of the main gear strut.

In addition to the quasi-static loading test of the main gear strut, dynamic drop tests were performed on the nose gear assembly. These tests were performed to characterize the velocity-dependent load-deflection properties of the oleo-pneumatic shock strut.

4.4 Modeling and Simulation of Test 1

The model representing the Test 1 configuration is shown in Figure 15. This model contains 135,637 nodes; 252 beam elements; 139,973 shell elements; 908 solid elements; 1 discrete beam; 44 parts; 8 Constrained Nodal Rigid Bodies (CNRBs); 16 different materials; 1,524 concentrated masses; 1 card defining gravity; and 1 rigid wall. The CG of the aircraft model was assigned the same initial velocity conditions as measured for the test (722.4-in/s forward velocity and 276-in/s vertical velocity). In addition, a pitch angular velocity of +16.5-degrees/s was assigned about the CG of the model representing the measured condition. The aircraft was also pitched by 1.5° (nose up) to match the orientation of the test article at impact. The concrete impact surface, which is not depicted in Figure 15, was modeled as a horizontal rigid wall, located just below the model. Most of the shell elements used in the model were assigned a Belytschko-Tsay (Type 2) formulation; however, the 0.7-in.-thick shell elements forming the main gear struts (leaf springs) were assigned a fully integrated formulation (Type 16). A nominal shell element edge length of approximately 1-in. was used. In addition, four ELTs were included in the Test 1 model and they were represented as rigid boxes made of solid elements. Two ELTs were located on the floor behind the pilot and co-

pilot seats and two were mounted to the left and right sidewalls of the tail, as shown in the cutaway views of the model in Figures 16(a) and (b). The ELT boxes were connected to the floor and sidewall through coincident nodes. Other ballast including the wing fuel, engine, propeller, DAS box, two seats, and the two ATD occupants were simulated as concentrated masses.

As stated in Reference 9, the landing gear of the Cessna 172 is a tricycle type with a steerable nose wheel, and two main gear wheels. Shock absorption is provided by spring-steel main landing gear struts and the nose gear oleo-pneumatic shock strut. A schematic drawing of the nose gear is shown in Figure 17(a) along with a depiction of the model of the nose gear in Figure 17(b). In the model, the nose gear wheel was represented as a collection of several parts including the tire, axle, rim, hub, and yoke. The nose gear wheel and the main landing gear wheels were free to rotate about their respective axles in the model. The oleo-pneumatic shock strut was represented as a telescoping beam that was attached on one end to the wheel yoke and on the other to a CNRB that was attached to the firewall at several locations. The telescoping beam was assigned estimated load-displacement properties for the given impact velocity condition. The material property assigned to the beam was *MAT_GENERAL_SPRING_DISCRETE_BEAM. A depiction of the main gear model is shown in Figure 18. The large structure that connects the wheel assembly to the subfloor, called the main gear leaf spring or strut, is represented using Type 16 shell elements that are 0.7-in. thick. The main gear leaf springs are curved slightly to match the shape of the actual main gear structure, and steel plates were added near the top of the leaf springs for use in lifting the aircraft during the test. Finally, the leaf springs were assigned material properties representing spring steel using the *MAT_PLASTIC_KINEMATIC card in LS-DYNA.

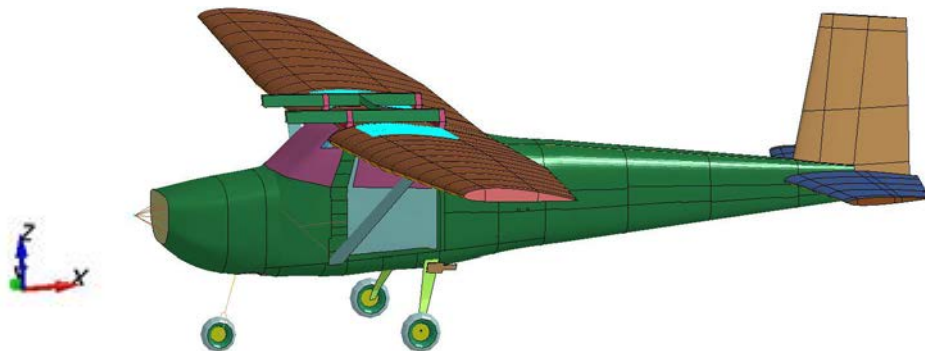


Figure 15. LS-DYNA model representing the Test 1 configuration.

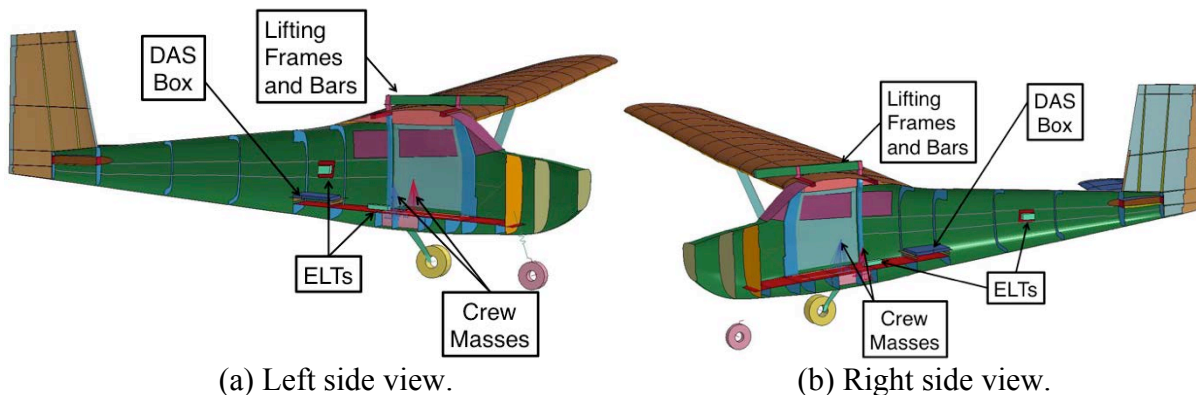


Figure 16. Cutaway views of the Test 1 model.

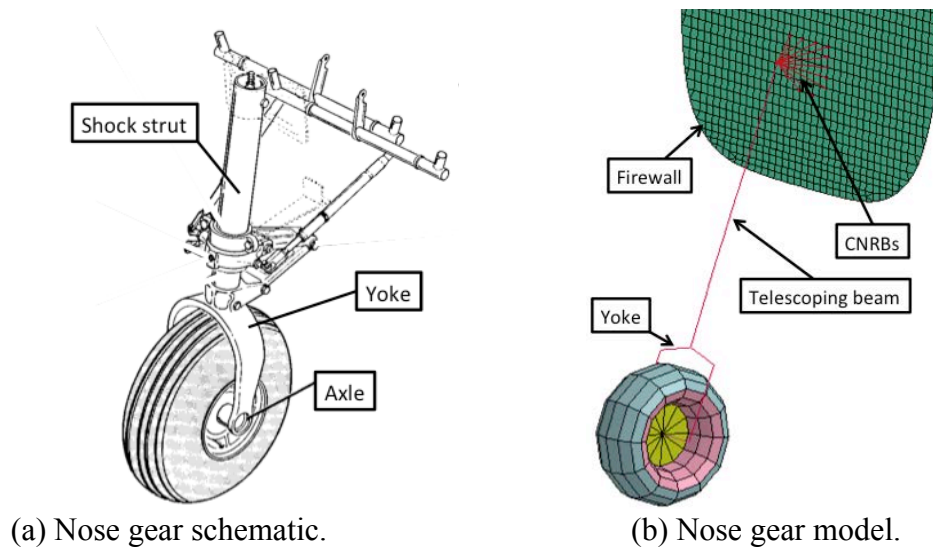


Figure 17. Cessna 172 nose gear.

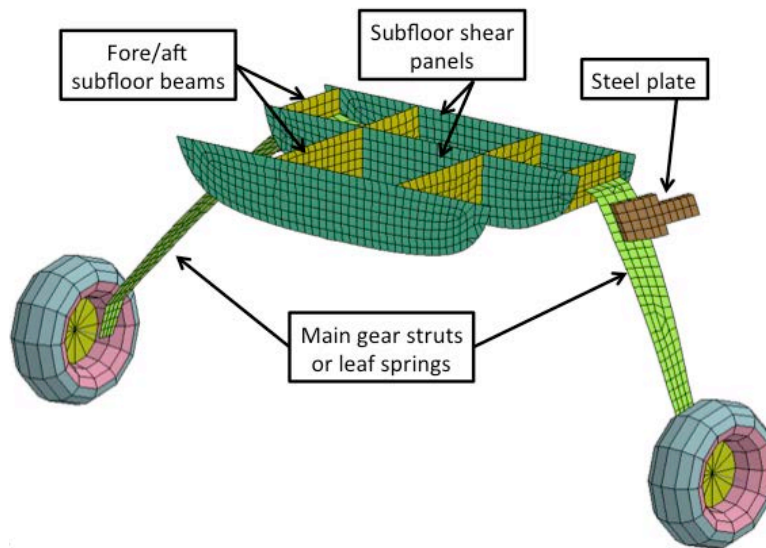


Figure 18. Main gear model.

Material properties are listed in Table 1 that were assigned to various parts within the airframe model. The C-172 aircraft were constructed primarily of aluminum and two different aluminum material models were defined. Material 1 was represented using `*MAT_PLASTIC_KINEMATIC`, which is a material model used to simulate elastic-plastic-strain hardening response with a defined failure strain. This material was assigned to shell elements representing the outer skin, fuselage frames, floor, subfloor shear panels, wing skin, wing ribs, wing spars, doors, and tail. A second aluminum material (Material No. 11) was defined as `*MAT_ELASTIC` with the same density, modulus, and Poisson's Ratio as Material 1. This material was added due to the fact that some beam elements cannot be assigned `*MAT_PLASTIC_KINEMATIC`. Material 2 was input to represent the properties of polycarbonate, which was assigned to shell elements representing the windows. Material 4 represented spring steel and was assigned to shell elements representing the main landing gear struts. This material was also represented as `*MAT_PLASTIC_KINEMATIC`. A second elastic material model was input for steel (Material No. 5) and it was assigned to various parts within the model including the firewall, tire rims, tire yokes, and onboard lifting hardware. A

rigid material (*MAT_RIGID) was input (Material No. 12) that was assigned to solid elements representing the ELTs and the DAS box. Finally, an elastic material model was developed for the tire rubber (Material No. 51). Most of these material models were generated using handbook data; however, it is useful to note that, following Test 1, several coupons were cut from straight sections of the aircraft skin. These coupons were tested in tension and the resulting data provided excellent agreement with the Material No. 1 input data.

Table 1. Material properties used in the airframe models.

No.	Material Name	Density, lb-s ² /in ⁴	Young's Modulus, psi	Poisson's Ratio	Yield Stress, psi	Tangent Modulus, psi	Failure Strain, in/in
1	Aluminum	2.525E-4	1.0E07	0.3	40,000	1.4E05	0.25
2	Polycarbonate	1.124E-4	5.0E05	0.3	-	-	-
4	Spring Steel	7.359E-4	3.0E07	0.3	2.4E05	1.4E05	0.2
5	Steel	7.359E-4	3.0E07	0.3	-	-	-
11	Aluminum	2.525E-4	1.0E07	0.3	-	-	-
12	Rigid Material	1.563E-4	1.0E-7	0.2	-	-	-
51	Tire Rubber	1.200E-4	1.0E06	0.4	-	-	-

The finite element model representing Test 1 was executed for 0.325-s on a Linux workstation computer with 8 processors, running LS-DYNA V971 R712 Shared Memory Parallelism (SMP) double precision, and required 4 hours and 15 minutes clock time to reach normal termination. Nodal output requests for the simulation included acceleration- and velocity-time histories at locations matching accelerometers mounted in the test article. Due to the fact that the pitch attitude of the aircraft remained small (within $\pm 1.5^\circ$) during the pulse duration of interest, acceleration and velocity data were output from the model in the global coordinate system which is depicted in Figure 15.

Test-analysis comparisons are presented in three categories: model and test article inertial properties, kinematic assessment of the time sequence of events, and time-history plots of vertical acceleration and velocity. For the acceleration time histories, both the test data and analytical predictions were filtered using a SAE CFC 20-Hz low-pass filter [15]. Note that the primary loading during the first 0.35-s of the impact event was in the vertical direction. During this time period, forward accelerations were extremely low, until the aircraft impacted the catch net at approximately 0.5-s. Consequently, forward acceleration and velocity comparisons are not shown for Test 1. However, since the average forward acceleration responses were below the threshold of ELT activation, these results are discussed in Appendix A.

4.4.1 Test 1 Inertial Properties

Prior to full-scale crash testing, the fully loaded Test 1 aircraft was tested to determine its total weight and CG locations. As an initial check of model fidelity, a comparison of inertial properties was made and the results are shown in Table 2. Note that the CG subscripts refer to the coordinate axes shown in Figure 15. It should also be noted that the x-direction CG values are measured from the firewall, the y-direction CG values are measured from the centerline of the aircraft, and the z-direction CG values are measured relative to the ground.

Table 2. Test-analysis comparison of inertial properties for Test 1.

Parameter	Model	Test	Difference	% Difference
Total weight, lb.	1,998.1	2,000.0	1.9	0.1
CG _x , in.	43.3	44.5	1.2	2.7
CG _y , in.	-0.05	0.00	0.05	-
CG _z , in.	51.1	46.3	-4.8	10.4

As indicated in Table 2, the model weight was within 2-lb of the 2,000-lb test article weight, and the model CG locations were within 2- to 5-inches of the test values. These results are an indication that the model represented the inertial properties of the test article reasonably well.

4.4.2 Test 1 Kinematic Assessment

A comparison of the time sequence of events is shown in Figure 19. This figure highlights four major events occurring during the time sequence including: initial nose gear impact, the time of maximum main gear spread, time of tail impact, and time of maximum rebound velocity, i.e. the tires are no longer in contact with the impact surface. For the test, the event timing was determined based on photogrammetric analysis. A side view of the model is shown at the time of each event. Photographs taken from a side view camera are shown for the test for the first three events; however, by the time of maximum rebound velocity, the aircraft had traveled outside the field of view of this camera. Consequently, an image was used from another camera for the fourth event. The model predicts the time of maximum main gear spread within 0.005-s. However, the predicted time of tail impact is 0.155-s compared with 0.125-s for the test, a difference of 0.03-s. Also, the time of rebound differs between the test and the model by 0.044-s. It should be noted that the time of tail impact is confirmed based on an acceleration response obtained from that location. However, the time of rebound for the test is difficult to determine precisely from the camera views. The timing differences between the test and model may be attributed to several factors including inaccurate nose gear estimated load-deflection properties, the offset in the vertical CG location, and uncertainty in the moments of inertia of the model. However, despite these differences, the model captured the kinematics of the test reasonably well.

4.4.3 Test 1 Time-History Comparisons

Vertical acceleration time-history comparisons are shown in Figures 20(a)-25(a) matching various accelerometer locations within the test article. For these plots, the raw acceleration test data were filtered using the SAE CFC20 filter [15]. The analytical data were output from LS-DYNA in the global coordinate system, which is depicted in Figure 15, and filtered using the same SAE CFC20 filter. In addition, vertical velocity responses are shown for each location and are plotted in Figures 20(b)-25(b). For these plots, the raw acceleration data were integrated to obtain the test velocity responses, and the analytical responses were output directly from the simulation. In addition, test-analysis vertical acceleration and velocity responses of the four ELTs that were mounted in the aircraft are shown in Figures 26-29. As an indication of the level of test-analysis comparisons, average accelerations were determined for both the test and predicted responses based on pulse durations determined from the velocity plots. Table 3 summarizes the test-analysis comparison metrics including average acceleration, pulse duration, and delta-V for both the structural and ELT data.

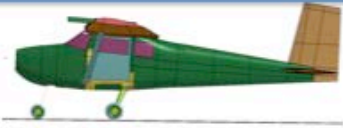







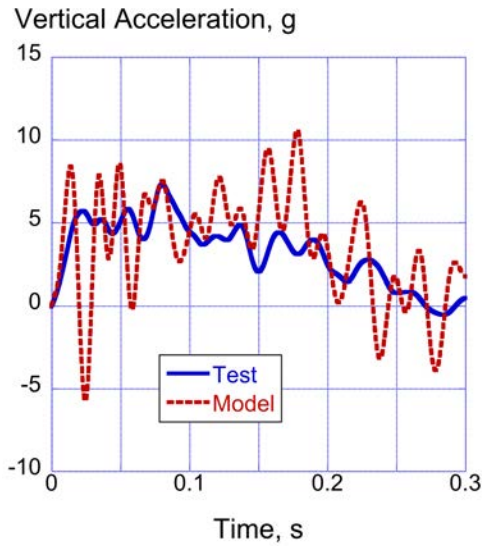
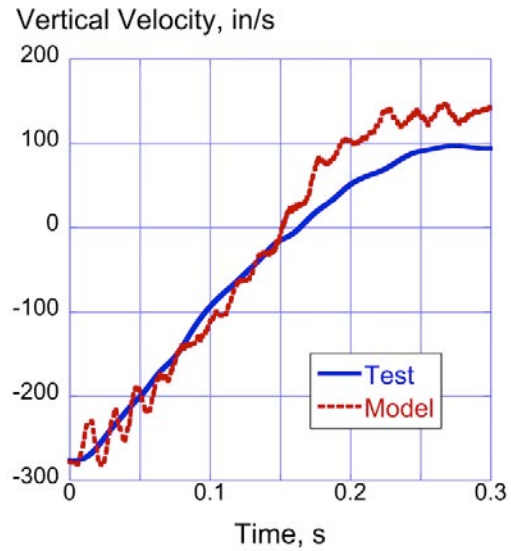
Event	Model	Test
Initial Impact	 T= 0.0-s	 T= 0.0-s
Time of max main gear spread	 T= 0.085-s	 T= 0.09-s
Time of tail impact	 T= 0.155-s	 T= 0.125-s
Time of initial rebound	 T= 0.322-s	 T= 0.366-s

Figure 19. Time sequence of events comparison.

Several observations can be made by examining the comparison plots of vertical structural acceleration responses shown in Figures 20-25. First, even though the test and analysis data were filtered using an SAE CFC20 filter [15], the acceleration responses still contain a high level of oscillations, making it difficult to extract an underlying acceleration pulse. Yet, the data in these plots were analyzed, as shown in Table 3. Average acceleration values for the test were generally low in magnitude, ranging from 3.57-g at the pilot floor location to 4.98-g in the tail. The predicted average accelerations showed excellent agreement with the test data, also indicating a range of 3.67-g for the pilot floor location and 4.96-g at the tail. For all of the parameters that were compared in Table 3 for structural airframe locations, the maximum percentage difference was 9.9%. Comparisons of vertical velocity responses were particularly close, with the model capturing the significant change in slope of the vertical velocity response of the tail, as shown in Figure 25. Likewise, comparisons of the floor- and sidewall-mounted ELT vertical acceleration and velocity responses were in close agreement. Note that the ELT acceleration responses shown in Figures 26-29 contain many oscillations, despite filtering at 20-Hz. These oscillations may be attributed to the method used to mount the ELTs. Additional information on this test-analysis comparison effort may be found in Reference 16.

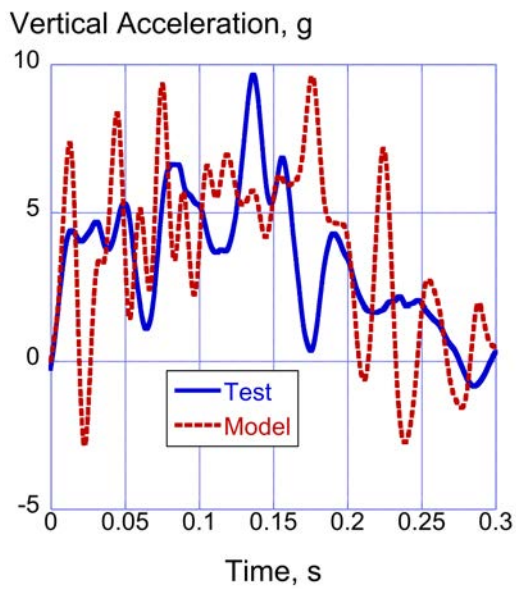


(a) Vertical acceleration.

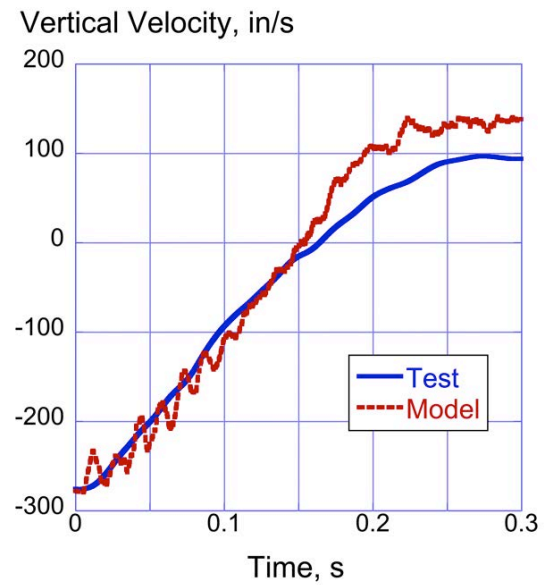


(b) Vertical velocity.

Figure 20. Test-analysis comparison of acceleration and velocity responses for the Test 1 pilot floor.

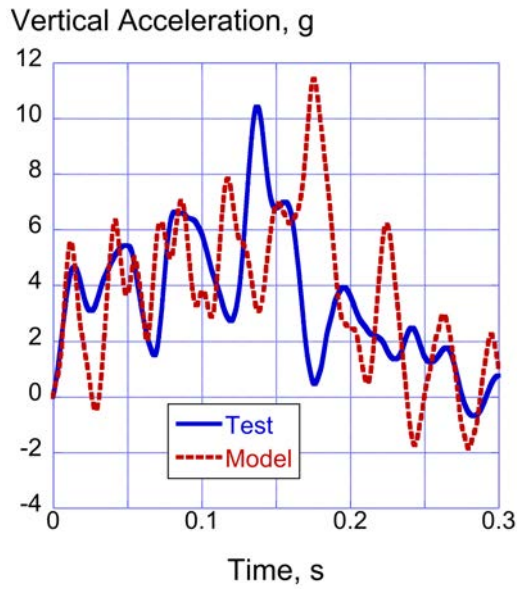


(a) Vertical acceleration.

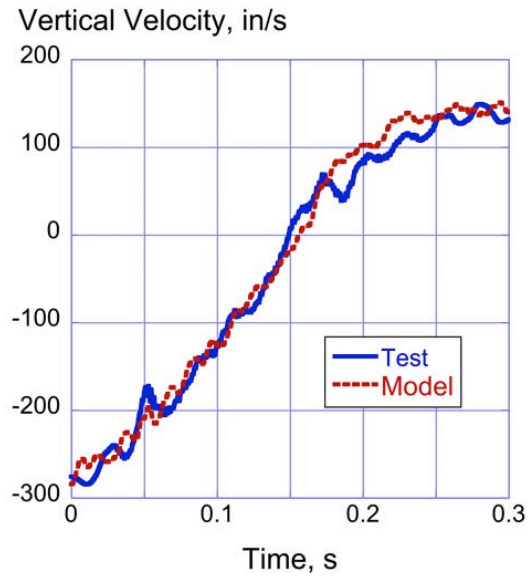


(b) Vertical velocity.

Figure 21. Test-analysis comparison of acceleration and velocity responses for the copilot floor.

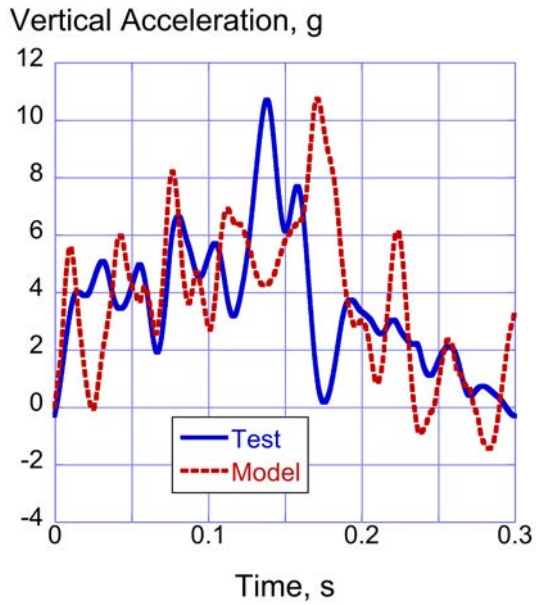


(a) Vertical acceleration.

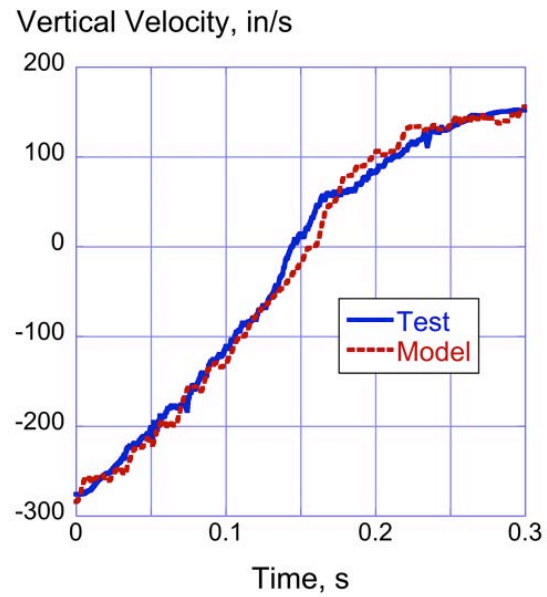


(b) Vertical velocity.

Figure 22. Comparisons of acceleration and velocity responses for the left doorframe.

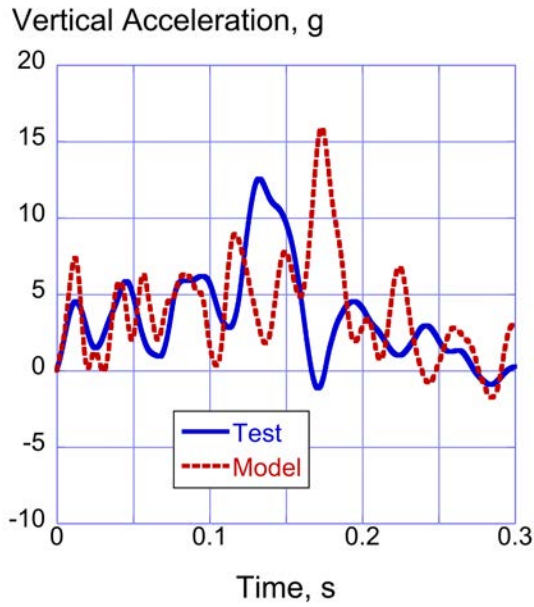


(a) Vertical acceleration.

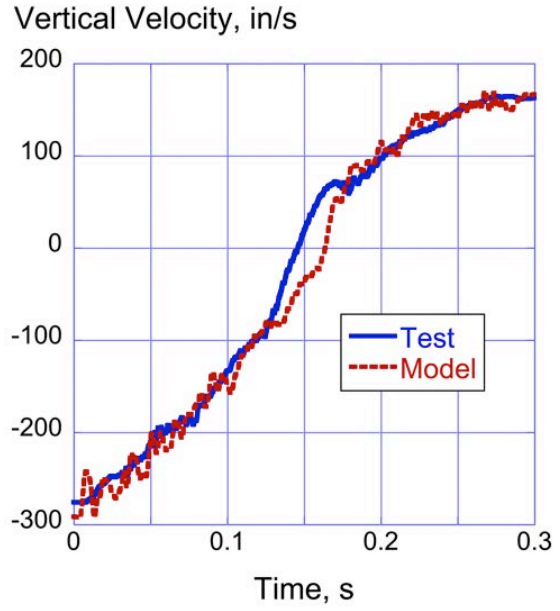


(b) Vertical velocity.

Figure 23. Comparisons of acceleration and velocity responses for the right doorframe.

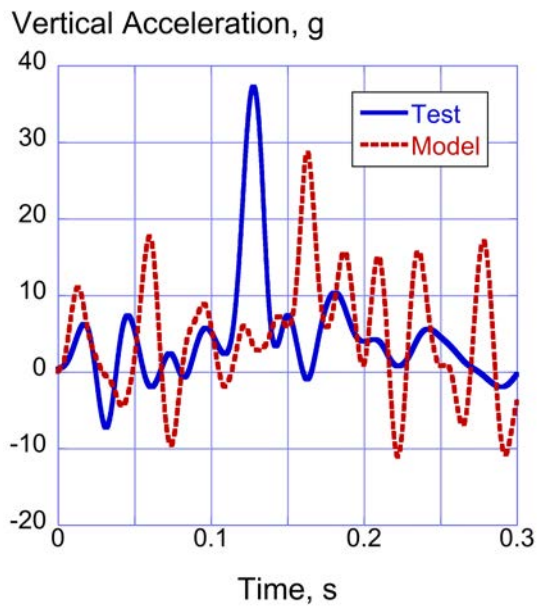


(a) Vertical acceleration.

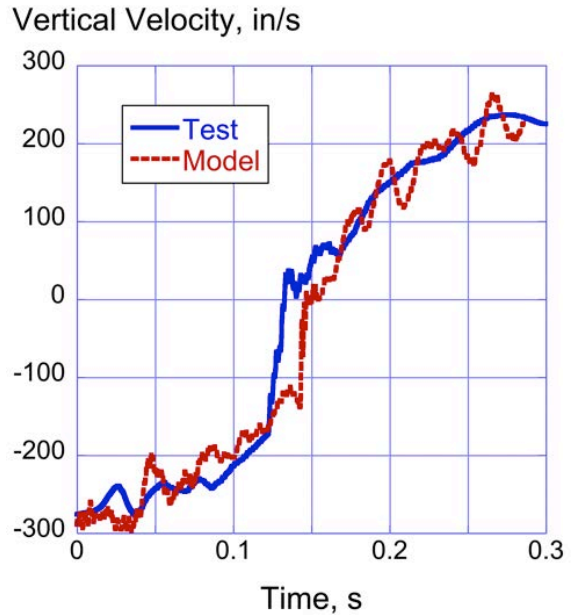


(b) Vertical velocity.

Figure 24. Comparisons of acceleration and velocity responses for the DAS box/floor.

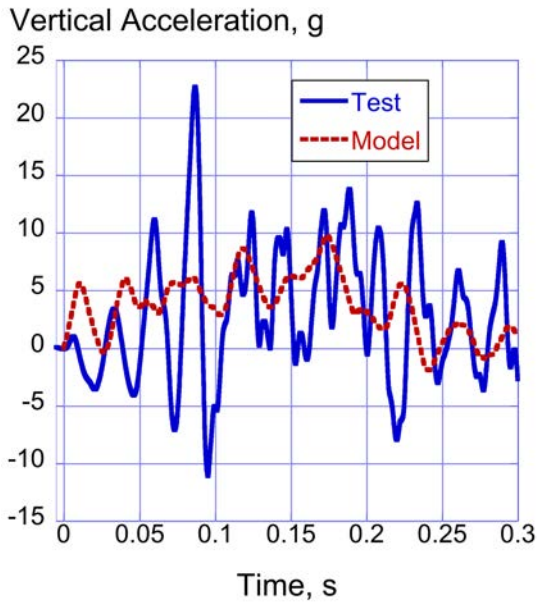


(a) Vertical acceleration.

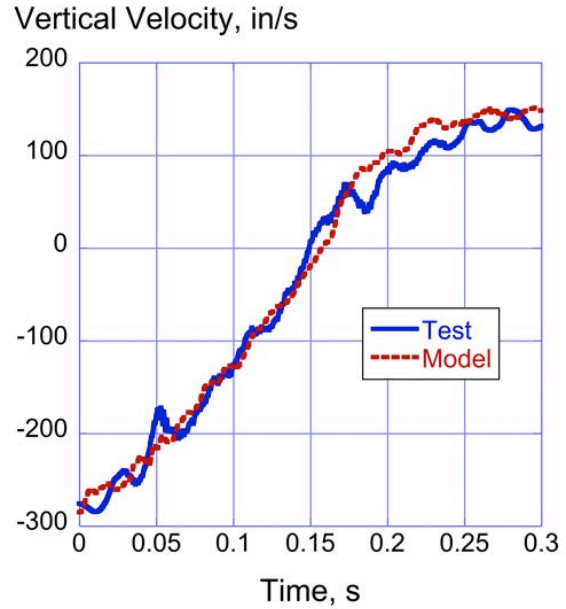


(b) Vertical velocity.

Figure 25. Comparisons of acceleration and velocity responses for the tail.

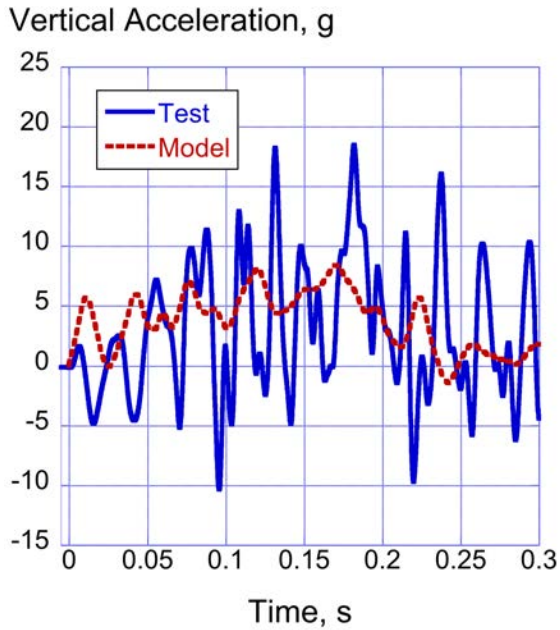


(a) Acceleration responses.

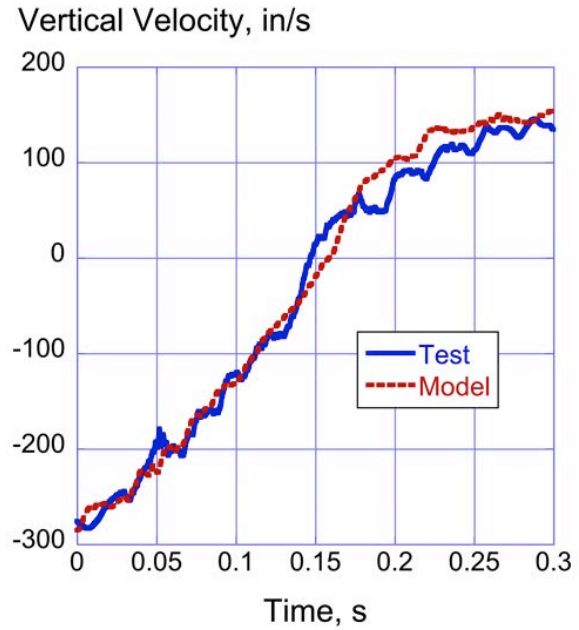


(b) Velocity responses.

Figure 26. Test-analysis vertical acceleration and velocity responses of the left floor ELT.

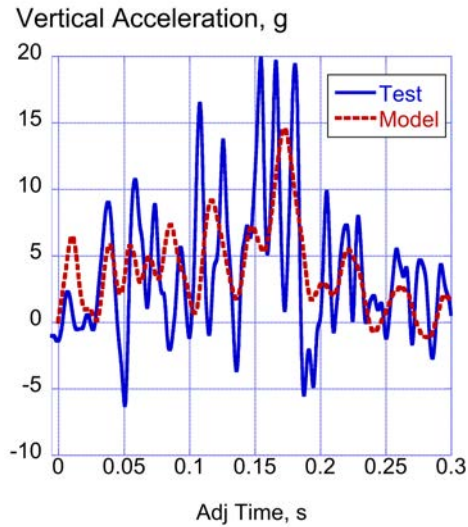


(a) Acceleration responses.

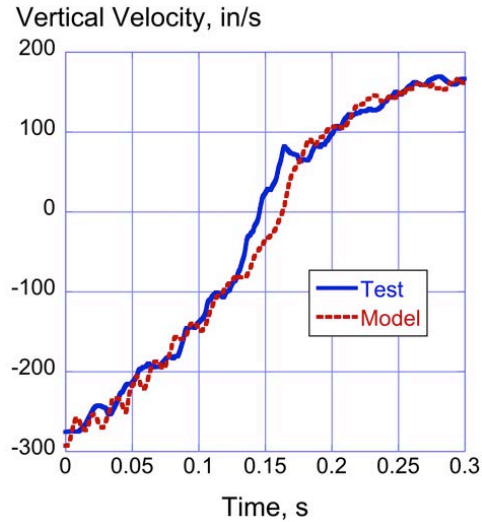


(b) Velocity responses.

Figure 27. Test-analysis vertical acceleration and velocity responses of the right floor ELT.

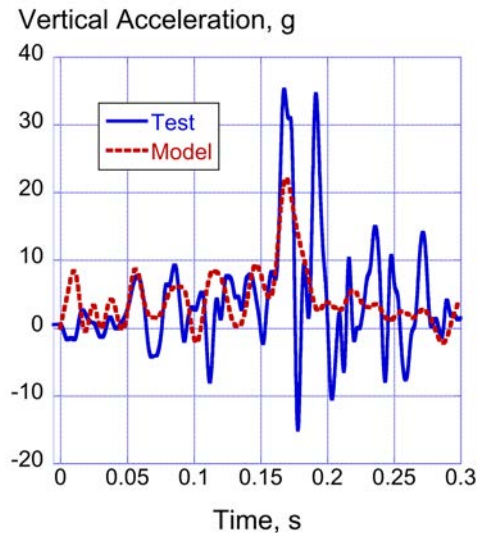


(a) Acceleration responses.

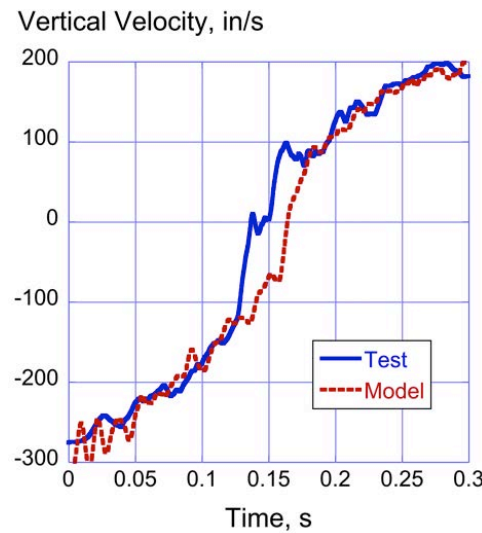


(b) Velocity responses.

Figure 28. Test-analysis vertical acceleration and velocity responses of the left sidewall ELT.



(a) Acceleration responses.



(b) Velocity responses.

Figure 29. Test-analysis vertical acceleration and velocity responses of the right sidewall ELT.

As mentioned previously, one of the test-analysis response metrics compared and included in this paper was the change in velocity (ΔV). The ΔV metric represents the total change in vertical velocity, from initial velocity to maximum rebound velocity. This metric is important because the mechanism for sensing crash pulses, g-switches in most ELTs, is designed to activate in accordance with a ΔV specification, as discussed in Appendix A and in Reference 17. All ΔV values were well predicted by the model, as indicated in Table 3.

Finally, a plot of measured vertical velocity of the CG is shown in Figure 30, along with predicted velocity responses from two nearby locations, the DAS box and the rear center ceiling beam. These channels were selected since no direct nodal output was obtained from the CG in the simulation. The experimental data were determined based on photogrammetry and the response contains some “noise” due to differentiation of digital displacement data to obtain velocity. However, the

agreement between the test response and the two selected channels is excellent. Both the test and predicted responses cross zero velocity at or near 0.15-s and both achieve maximum rebound of approximately 125- to 150-in/s by 0.25- to 0.3-s.

Table 3. Summary of test-analysis comparison metrics for Test 1.

Location	Parameter	Test	Model	% Difference
Pilot Floor	Avg. Vt. Acceleration, g	3.57	3.67	-2.8
	Pulse duration, s	0.27	0.29	-7.4
	delta-V, in/s	376.0	413.2	-9.9
Co-pilot floor	Avg. Vt. Acceleration, g	4.0	3.78	5.5
	Pulse duration, s	0.27	2.8	-3.7
	delta-V, in/s	376.0	412.2	-9.6
Lt. Doorframe	Avg. Vt. Acceleration, g	3.83	4.1	-7.0
	Pulse duration, s	0.2725	0.272	0.2
	delta-V, in/s	402.4	426.4	-6.0
Rt. Doorframe	Avg. Vt. Acceleration, g	3.79	3.96	-4.5
	Pulse duration, s	0.281	0.279	0.7
	delta-V, in/s	424.6	418.5	1.4
DAS Box	Avg. Vt. Acceleration, g	3.75	3.95	-5.3
	Pulse duration, s	0.282	0.293	-3.9
	delta-V, in/s	439.8	440.0	-0.05
Tail	Avg. Vt. Acceleration, g	4.98	4.96	0.4
	Pulse duration, s	0.266	0.269	-1.1
	delta-V, in/s	541.3	533.2	1.5
Lt. Floor ELT	Avg. Vt. Acceleration, g	3.9	3.14	19.5
	Pulse duration, s	0.28	0.266	5.0
	delta-V, in/s	424.6	434.0	-2.2
Rt. Floor ELT	Avg. Vt. Acceleration, g	3.84	3.0	23.1
	Pulse duration, s	0.288	0.3	-4.2
	delta-V, in/s	421.8	428.7	-1.6
Lt. Sidewall ELT	Avg. Vt. Acceleration, g	4.0	3.9	2.5
	Pulse duration, s	0.28	0.298	-6.4
	delta-V, in/s	445.4	439.9	1.2
Rt. Sidewall ELT	Avg. Vt. Acceleration, g	4.18	4.33	-3.6
	Pulse duration, s	0.277	0.295	-6.5
	delta-V, in/s	474.6	476.0	-0.3

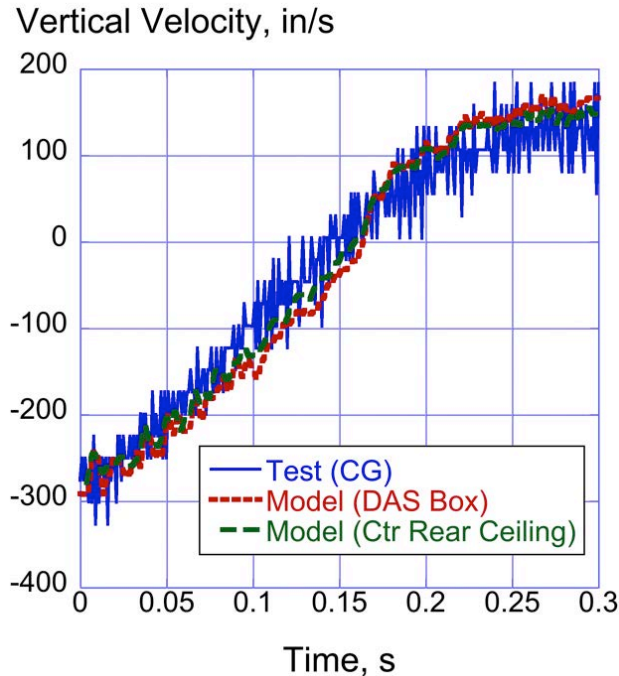


Figure 30. Test velocity response of the CG, as measured by photogrammetry, compared with the predicted velocity responses of the DAS box and the rear center ceiling support beam.

4.5 Modeling and Simulation of Test 2

Since both the Test 1 and Test 2 aircraft were straight tail configurations, the LS-DYNA structural model for Test 2 was derived from the Test 1 simulation model [16]. However, many changes to the model were required to match the Test 2 aircraft configuration and to capture the complex impact scenario. The Test 2 model with the airplane in the 12.2° nose down impact condition is shown in Figure 31 [18]. The rigid wall in the Test 1 model was replaced with a layered soil bed constructed of solid elements. A material model (*MAT_SOIL_AND_FOAM) was assigned to each of the two layers of soil. The material properties of the top layer, Gantry Unwashed Sand (GUS), had previously been calibrated and documented at a specific density and moisture content by a commercial company [19], and was used in a prior simulation described in Reference 20. The softer bottom layer soil properties were reported in Reference 21. An important modification made to the material model was to increase the unloading modulus to prevent excessive rebound [19]. Note that changes in the moisture and density of the soil can vary the bearing strength considerably. Thus, a dynamic cone penetrometer was used to determine the bearing strength as a function of soil depth. Since water accumulated at the bottom of the soil, the bottom layer of soil was made much softer than the top layer. It should also be noted that all nodes forming the bottom and side surfaces of the layered soil block were fixed (i.e., no translational or rotational motion allowed) using Single Point Constraints (SPC) in the LS-DYNA model.

A spinner and propeller were added to the Test 2 model as these structures were noted to penetrate into the soil, as shown in Figure 31. Other changes included more detailed material models of the airplane structure that included plasticity and failure. The *MAT_PLASTIC_KINEMATIC representation, which allows for the full regime of properties from elastic through yielding and plasticity to failure was used for most of the metallic parts in the model. The occupant masses, represented by CNRBs attached to the seat tracks, were moved forward by 10-in. to match the test

condition. Also, an 8-in. x 12-in. hole was created on one side of the tail section to represent the hole produced by a pre-existing access panel that popped off upon first impact. Other changes made to the model included the addition of a fifth ELT, and the addition of an automatic single surface contact. Finally, prior to Test 2, the actual nose gear was essentially locked into place due to leakage problems. Consequently, the nose gear in the model was fixed using CNRBs. This oversimplification likely caused the predicted initial vertical accelerations to be higher than those measured. Also, the wing failure that occurred at 0.111-s after impact in Test 2 was not simulated due to time constraints.

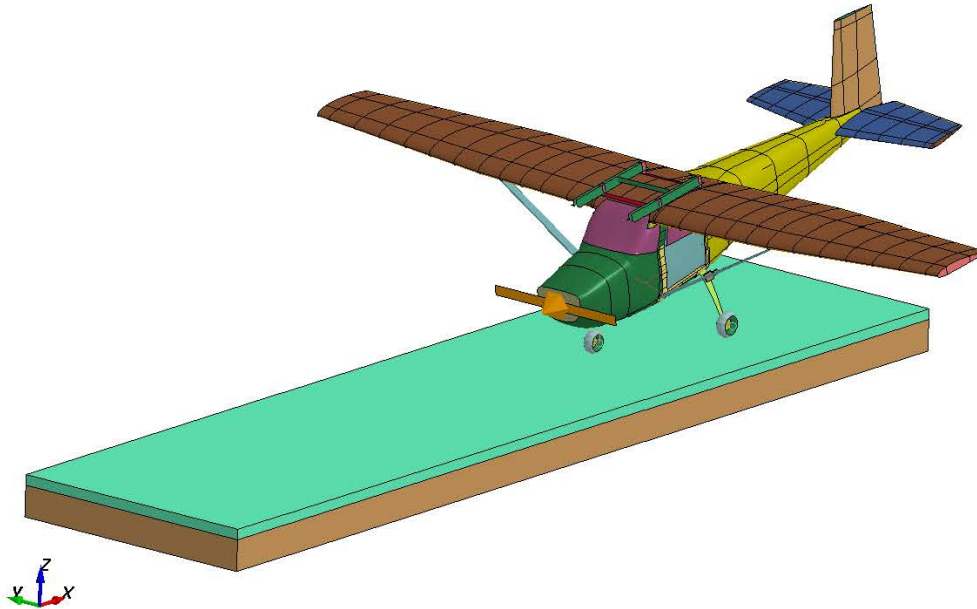


Figure 31. LS-DYNA model representing the Test 2 configuration.

The final model contained over 200,000 elements with a nominal element edge length of 1-in. and was simulated for 0.35-s with a time step of approximately 1.5×10^{-7} seconds. The velocity conditions were specified at the model CG using an *INITIAL_VELOCITY_GENERATION card. This card allows input of the initial forward and vertical velocities, which were the same as measured for the test (823.2-in/s forward velocity and 344.4-in/s vertical velocity). In addition, a pitch angular velocity of +16.1-degrees/s was assigned about the CG of the model representing the measured condition. The aircraft was also pitched by 12.2° (nose down) to match the orientation of the test article at impact. The wing fuel, engine, two seats, and the two dummy occupants were simulated as concentrated masses. The model was executed on a Linux workstation computer with 8 processors, running LS-DYNA V971 R7.1.2 SMP double precision, and required approximately 19 hours of clock time to simulate 0.35 seconds. Additional information on this test-analysis comparison effort may be found in Reference 18.

Test-analysis comparisons are presented in four categories: inertial properties, a kinematic assessment of the time sequence of events, soil deformations, and time-history plots of forward and vertical acceleration. For the LS-DYNA acceleration time histories, the analytical responses were output in local coordinate systems, defined at the accelerometer locations, and were filtered using a SAE CFC 20-Hz low-pass filter [15]. Note that in LS-DYNA, a local coordinate system can be defined at any node within the model. If data are requested in the local coordinate system, then it will include the influence of rotation at the nodal location.

In addition, the vertical and forward velocities near the CG, based on photogrammetric analysis, are plotted versus the predicted responses, as output in the global coordinate system. Photogrammetry provides more accurate velocity data than integration of accelerometers that involve complex rotations at large angles such as were observed during Test 2. Note that the gravity vector skews the acceleration data as the local axis in the airplane rotates. Although the gravity effect is at most a one-g effect, it can produce a bogus velocity when the local accelerometer data are integrated over durations of several tenths of seconds. Consequently, analytical velocity data were output in the global axis system and differentiated photogrammetry data were used to generate the test velocities.

4.5.1 Test 2 Inertial Properties

As a preliminary check of model fidelity, the inertial properties of the test article and the model are compared in Table 4. The largest difference is in the location of the vertical CG. However, the location of the vertical CG is quite difficult to measure accurately. Note that the x-coordinate of the CG is measured from the firewall, the y-coordinate of the CG is measured along the centerline of the aircraft, and the z-coordinate of the CG is measured relative to the ground. As can be seen in Table 4, the model closely matches the test measurements, with the largest percentage difference equal to 3.3%.

Table 4. Test-analysis comparison of inertial properties for Test 2.

Parameter	Model	Test	Difference	% DIFF
Weight, lb	2120	2114	6.0	0.3
CGx, in.	39.1	39.5	0.4	1.0
CGy, in.	-0.04	0.0	0.04	-
CGz, in.	49.7	48.1	1.6	3.3

4.5.2 Test 2 Kinematic Assessment

A comparison of the time sequence of events is shown in Figure 32. This figure highlights four major events during the time sequence including: initial nose gear impact, the time of main gear impact, time of cowling impact, and the end time of the major crash acceleration pulse at 0.240-s. A side view of the model is shown at the time of each event for comparison. The model captures the kinematics of the test quite well.

4.5.3 Test 2 Soil Deformation

The tire tracks in the soil (see Figure 33(a)) can be compared with model predictions, as shown in Figure 33(b). The numerical comparisons and percent differences are summarized in Table 5. As can be seen, the model predicted the soil deformations quite well considering the complexity of the test conditions and the simplicity of the soil model.

4.5.4 Test 2 Time-History Comparisons

Filtered forward and vertical acceleration time-history comparisons are shown in Figures 34-39 matching various structural accelerometer locations within the test article. Note that predicted accelerations were output in the local coordinate system defined at each accelerometer location in the model.

The forward acceleration responses obtained during the test exhibit a large negative (rearward) pulse, beginning at approximately 0.05-s, and achieving a maximum value of between 17- to 33-g at 0.13-s. The predicted responses generally match this overall behavior. For the pilot floor location

(see Figure 34(a)), the predicted response overshoots the test response, even though the timing of the two peaks is close. For the DAS box location (see Figure 36(a)), the predicted response lags the test response in time and has a lower magnitude peak (25-g compared with 34-g). The predicted forward acceleration response of the tail, shown in Figure 39(a), exhibits behavior that is different from the other predicted responses due to the buckling of the tail. The predicted response begins with a negative acceleration pulse, but at 0.1-s the curve changes direction due to the tail deformation, which occurs more rapidly than is seen in the test response.









Event	Model	Test
Initial Impact	 T= 0.0-s	 T= 0.0-s
Time of main gear impact	 T= 0.024s	 T= 0.026-s
Time of engine cowling impact	 T= 0.075 s	 T= 0.071 -s
End of major crash pulse	 T= 0.240s	 T=0.240-s

Figure 32. Comparison of time sequence of events for Test 2.

As shown in Figures 34(b)-38(b), the vertical acceleration responses obtained during the test generally exhibit a low-magnitude (0- to 5-g) initial oscillatory response, typically for the first 0.03- to 0.07-s, followed by a higher-magnitude acceleration pulse with peak values of 14- to 19-g. The peak accelerations occur at approximately 0.1-s. Following the peak, the test responses decrease back to low-magnitude values. Unlike the test, the predicted responses generally exhibit a higher magnitude initial response, starting at 10-g and increasing to 15-g. Peak values of between 16- and 20-g are obtained, before the acceleration responses decrease to low-magnitude values. Thus, the model matched the peak accelerations of the test response quite well. The difference in the initial acceleration responses may be attributed to several factors including: propeller, engine cowling, and nose gear contact forces, soil variability, and lumped masses to represent the seats and dummies. However, the likely culprit for the disparity is the nose gear modeling approach given that it was locked into place with CNRBs. In the test, the locked nose gear broke loose from its mounting, which would have required more detailed modeling than time and resources allowed. The vertical acceleration responses of the tail, shown in Figure 39(b), are somewhat different from the other

responses. The model over predicts the test response for the first 0.06-s, but then shows generally good agreement. The exact buckling response of the tail highly influences this behavior.

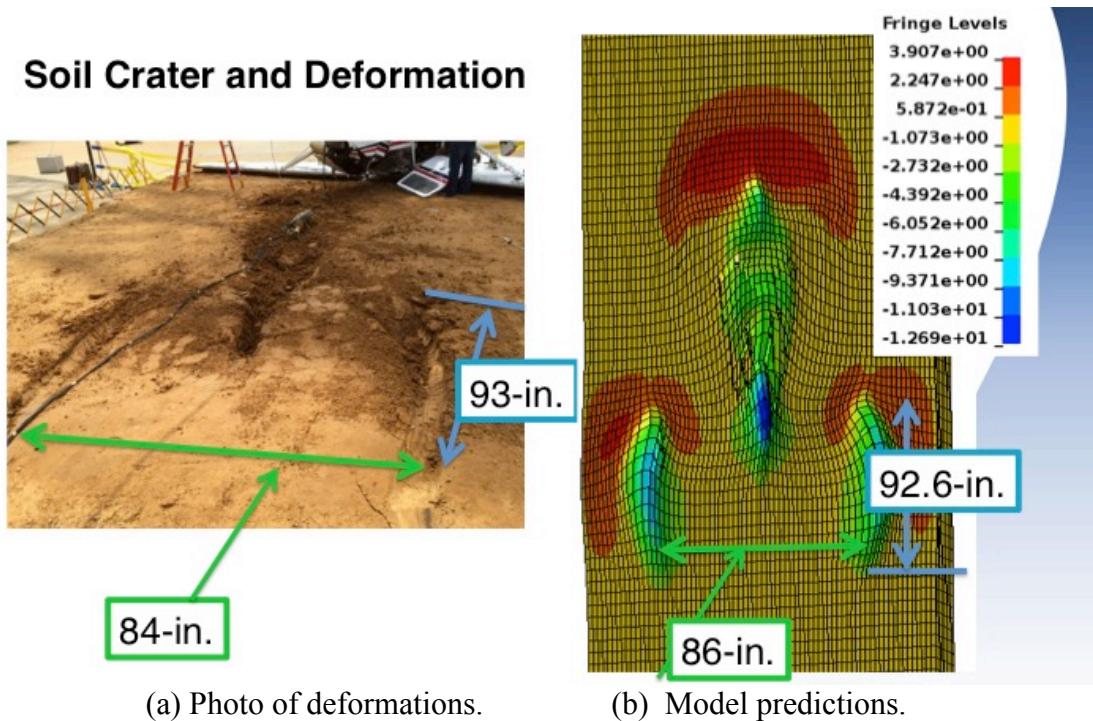
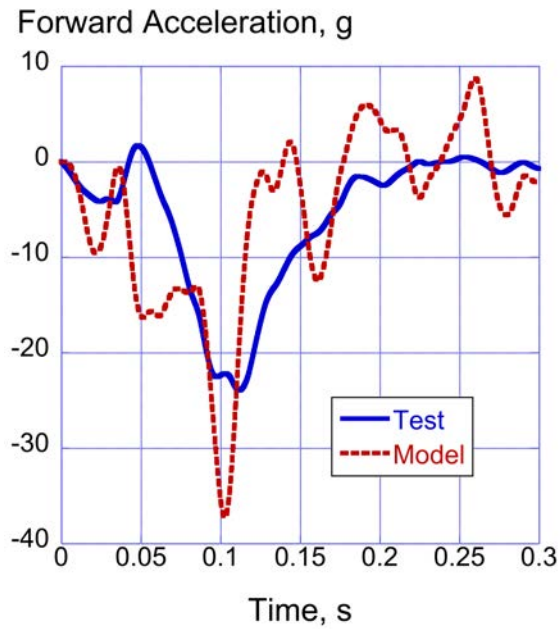


Figure 33. Measured and predicted soil deformations for Test 2.

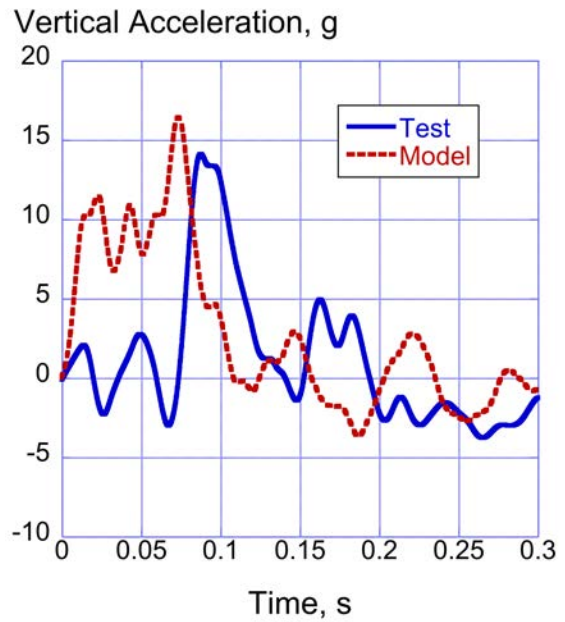
Table 5. Comparisons of Test and Model Soil Deformations for Test 2.

Parameter	Test	Model	% Difference
Nose gear hole depth, in.	10	11.5	13.0
Max depth of main gear tire depression, in.	7.5-8.0	8.0	-
Main gear left tire to right tire width (initial), in.	84	86	1.7
Distance from nose gear hole to propeller post-test, in.	116	120	3.3

In addition to the structural accelerometer comparisons for Test 2, plots of forward and vertical acceleration responses of the ELTs are provided in Figures 40-44, corresponding to ELT locations 1 through 5, as illustrated in Figure 6. As with the structural acceleration comparisons, the LS-DYNA predicted responses were output in the local axis system defined for each ELT. Also, values of pulse duration were estimated for both the test and predicted responses and these values were used to determine average accelerations. The pulse duration and average acceleration values are listed in Table 6. The results for the ELTs are similar to the structural acceleration responses. Note that the ELT1 accelerometer data in the vertical local axis was not reported as it contained anomalies. Thus, Figure 40 shows only forward acceleration comparisons.

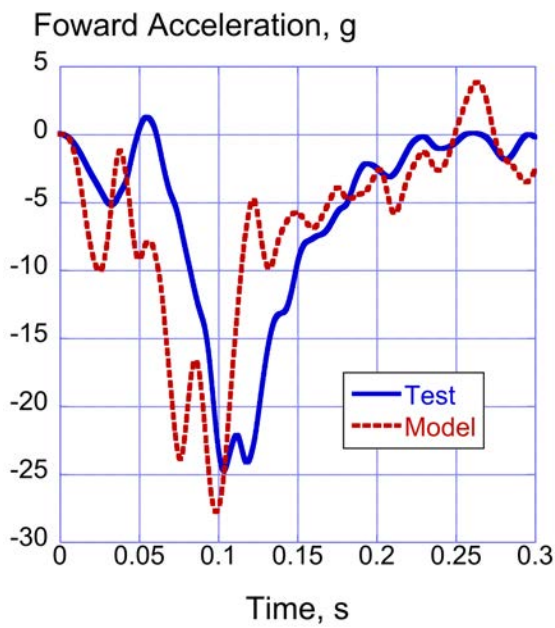


(a) Forward acceleration.

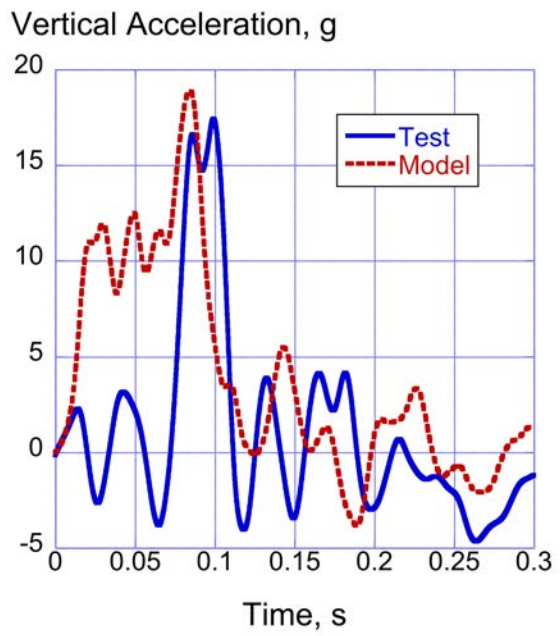


(b) Vertical acceleration.

Figure 34. Forward and vertical accelerations on the floor near the pilot in Test 2.

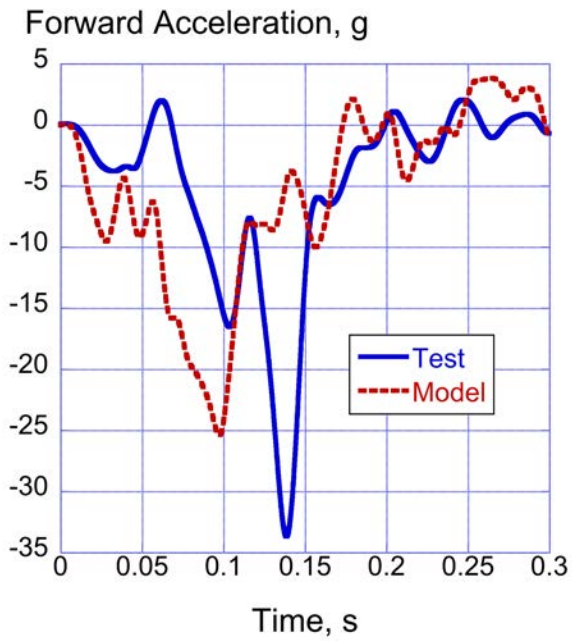


(a) Forward acceleration.

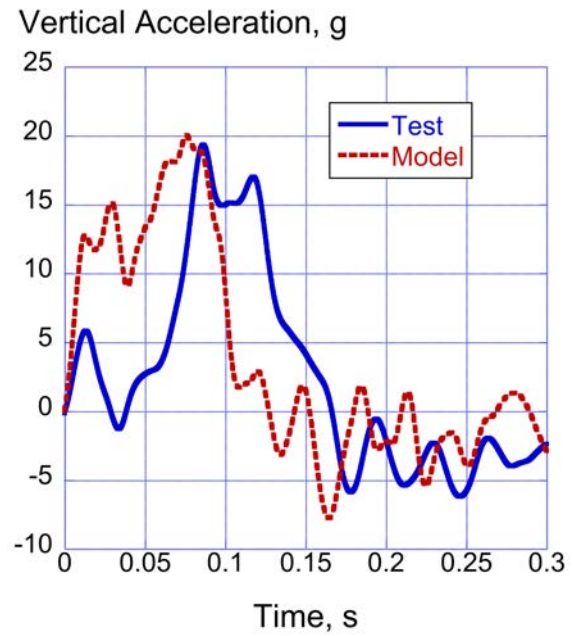


(b) Vertical acceleration.

Figure 35. Forward and vertical accelerations on the floor near the copilot in Test 2.

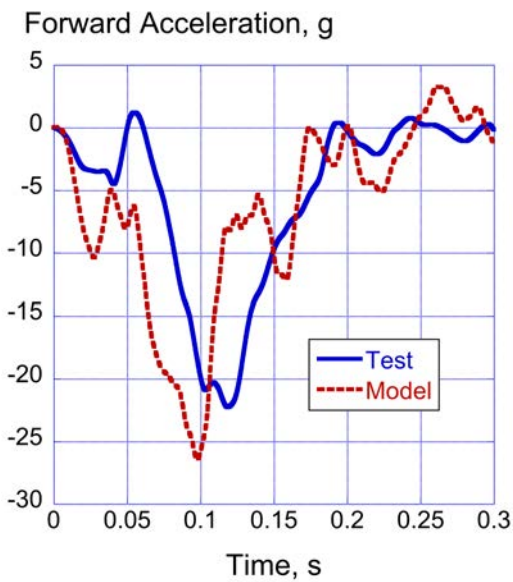


(a) Forward acceleration.

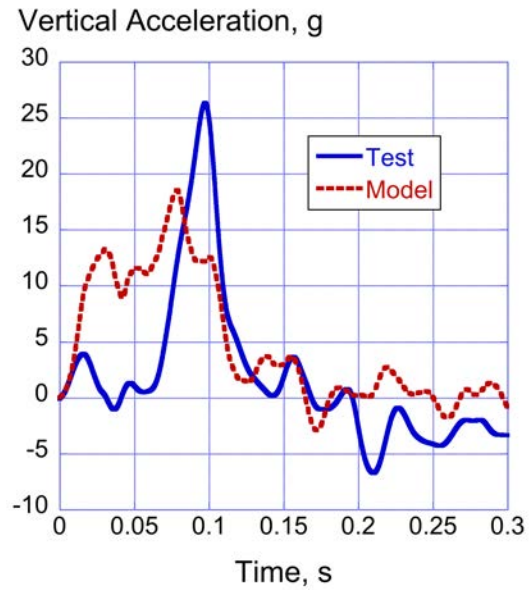


(b) Vertical acceleration.

Figure 36. Forward and vertical acceleration comparisons of the DAS Box in Test 2.

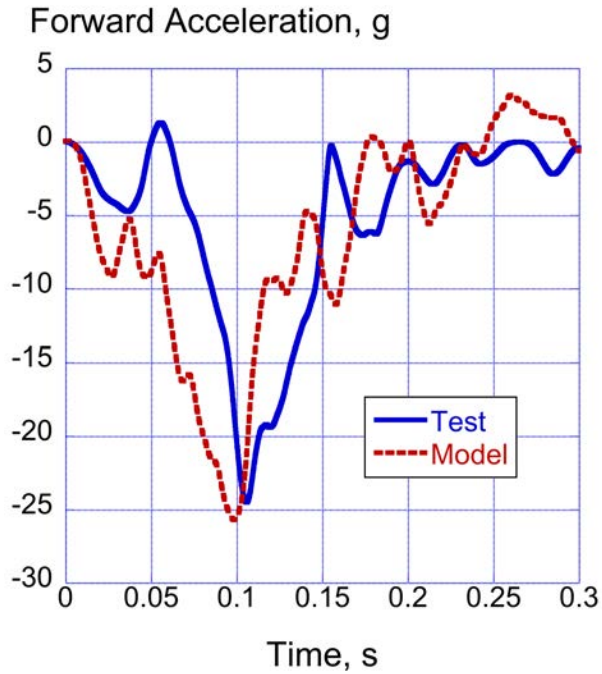


(a) Forward acceleration.

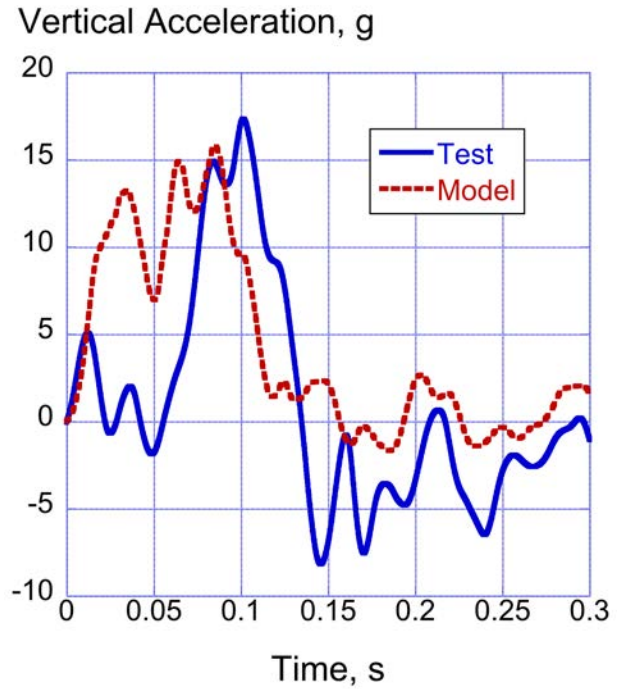


(b) Vertical acceleration.

Figure 37. Forward and vertical acceleration comparisons of the left doorframe in Test 2.

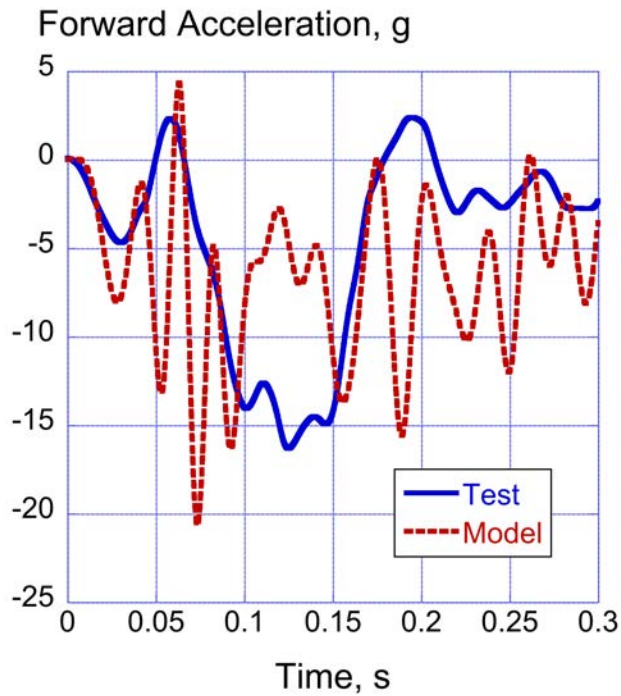


(a) Forward acceleration.

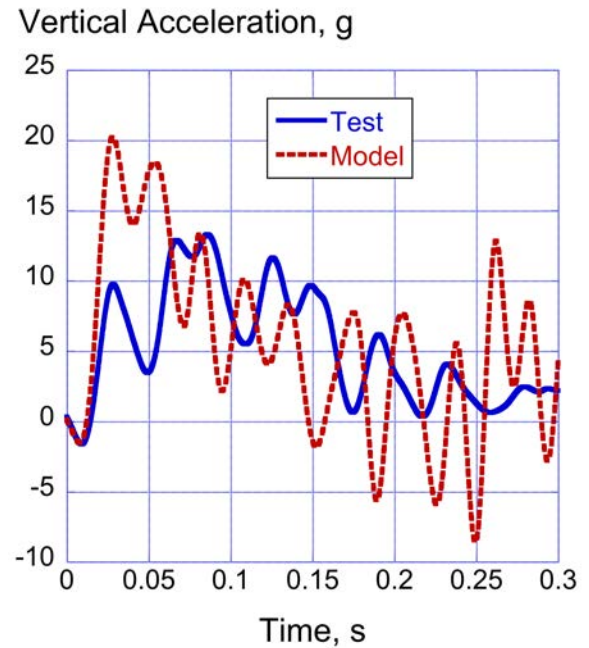


(b) Vertical acceleration.

Figure 38. Forward and vertical acceleration comparisons of the right doorframe in Test 2.



(a) Forward acceleration.



(b) Vertical acceleration.

Figure 39. Forward and vertical acceleration comparisons near the aircraft tail in Test 2.

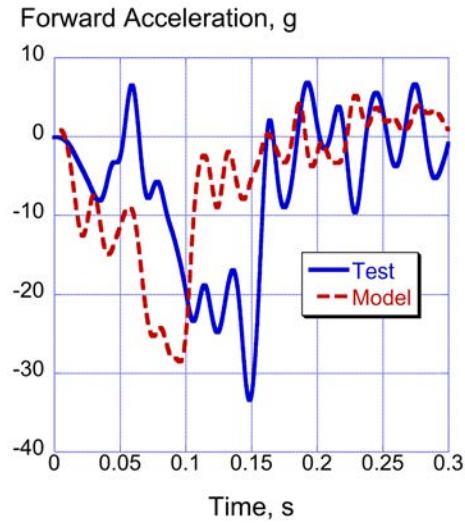
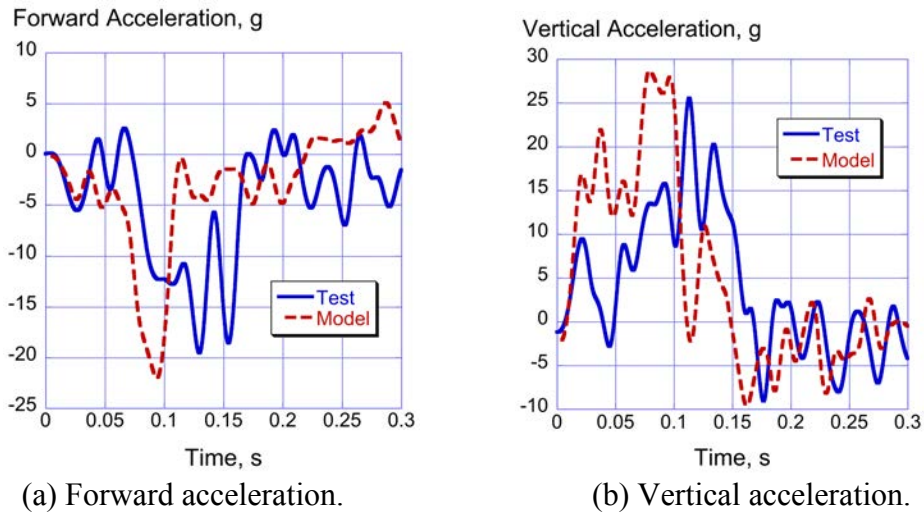


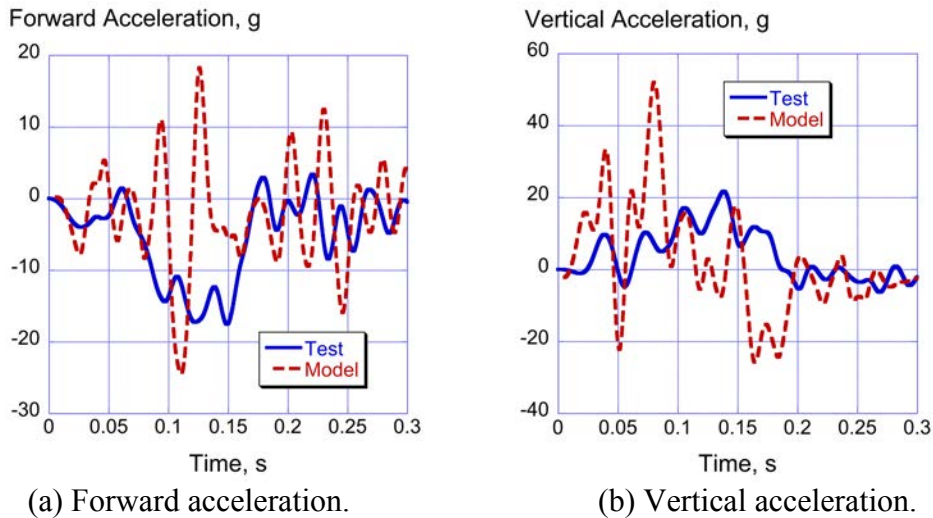
Figure 40. Test-analysis comparison of ELT1 forward acceleration responses for Test 2.



(a) Forward acceleration.

(b) Vertical acceleration.

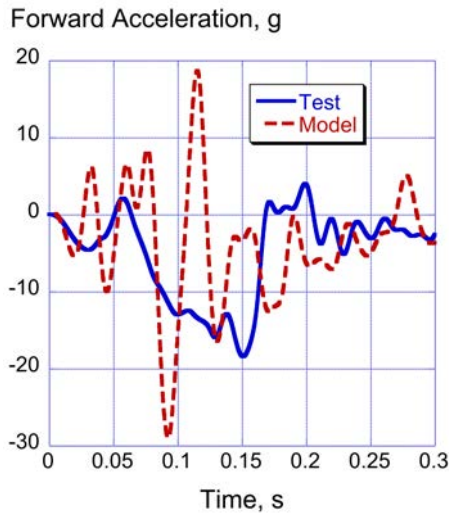
Figure 41. Test-analysis comparison of ELT2 forward and vertical acceleration responses for Test 2.



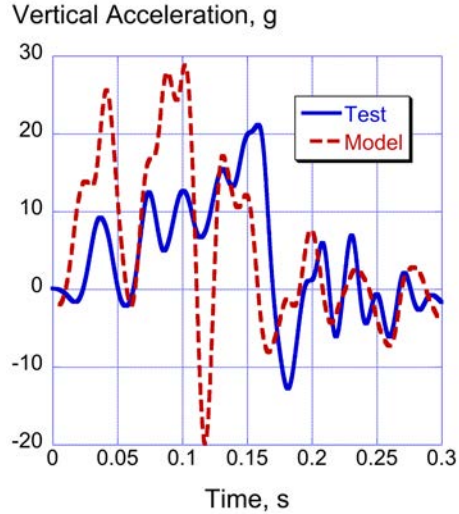
(a) Forward acceleration.

(b) Vertical acceleration.

Figure 42. Test-analysis comparison of ELT3 forward and vertical acceleration responses for Test 2.

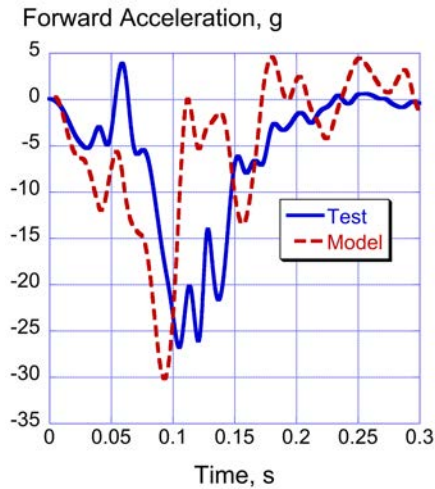


(a) Forward acceleration.

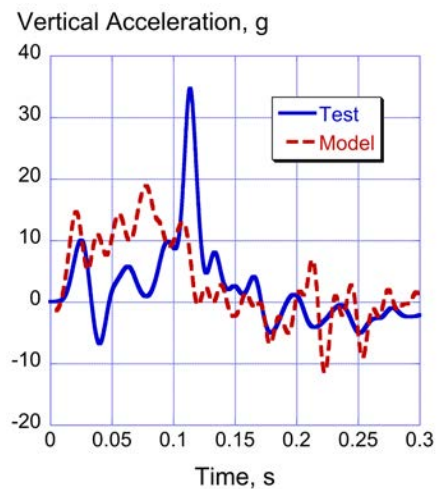


(b) Vertical acceleration.

Figure 43. Test-analysis comparisons of ELT4 forward and vertical acceleration responses for Test 2.



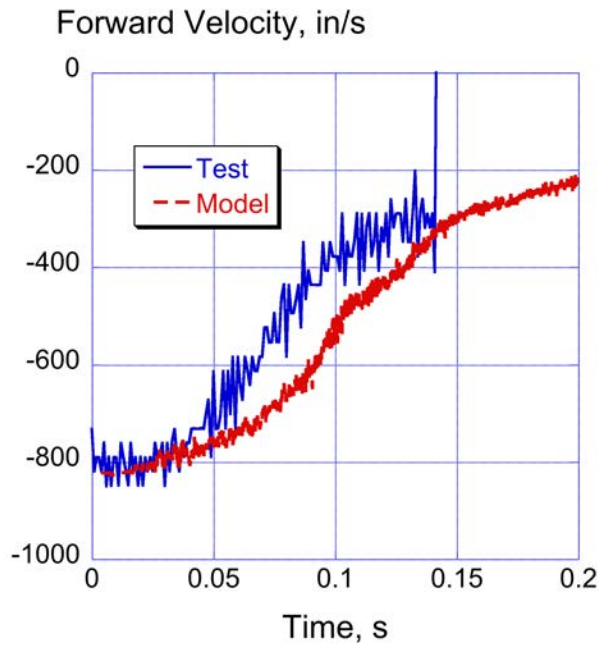
(a) Forward acceleration.



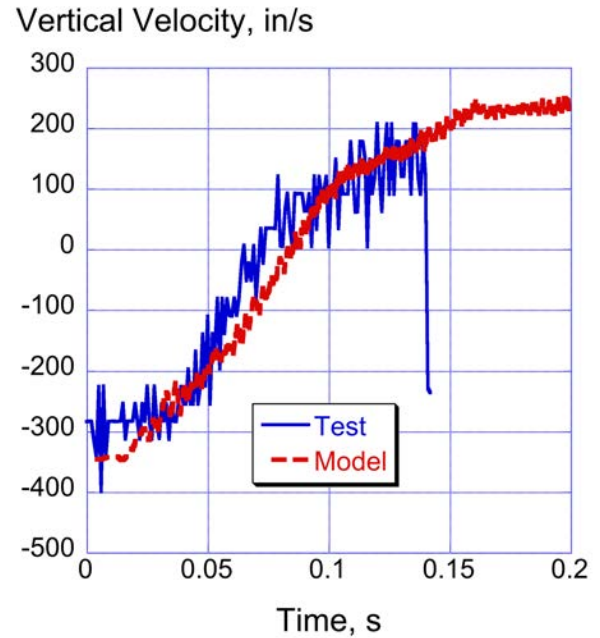
(b) Vertical acceleration.

Figure 44. Test-analysis comparisons of ELT5 forward and vertical acceleration responses for Test 2.

Global CG forward and vertical velocities are plotted versus predicted global responses from a location that is near the CG, as shown in Figure 45. For these plots, the CG test velocities were determined based on photogrammetric analysis. For the forward velocity, the model and CG responses agree up to 0.05-s, at which time the CG velocity response exhibits a fairly sharp change in slope and deviates from the predicted response. By the time the CG data ends at 0.15-s, the two curves are in close agreement once again. In general, the CG vertical velocity response and the predicted response are in better agreement. These results highlight the fact that interaction of the structure with the soil is a complex and challenging modeling task. At best, the properties of the soil can only be approximated for a large soil area such as the impact surface.



(a) Global forward velocity, in/s.



(b) Global vertical velocity, in/s.

Figure 45. Comparison of predicted global velocities at the pilot floor location with photogrammetry data.

Test-analysis calibration metrics for Test 2 are listed in Table 6. Since the integration of the raw acceleration data provided nonphysical results due to large rotation angles, the pulse durations were approximated from the acceleration responses shown in Figures 34-44. Also, for this same reason, delta-V metrics were not calculated and are not listed in Table 6. The results indicate that 32 of 42 metrics are within $\pm 20\%$.

Table 6. Summary of test-analysis comparison metrics for Test 2.

Location	Parameter	Test	Model	%Difference
Pilot Floor	Avg. forward acceleration, g	7.76	7.64	1.6
	Forward pulse duration, s	0.225	0.218	3.1
	Avg. vertical acceleration, g	3.0	4.22	-40.7
	Vertical pulse duration, s	0.194	0.203	-4.6
Copilot Floor	Avg. forward acceleration, g	6.95	8.2	-18.0
	Forward pulse duration, s	0.256	0.25	2.3
	Avg. vertical acceleration, g	2.84	5.69	-100.4
	Vertical pulse duration, s	0.189	0.198	-4.8
DAS Box	Avg. forward acceleration, g	7.57	8.72	-15.2
	Forward pulse duration, s	0.199	0.198	0.5
	Avg. vertical acceleration, g	7.44	9.24	-24.2
	Vertical pulse duration, s	0.166	0.153	7.8
Left Doorframe	Avg. forward acceleration, g	7.0	8.4	-20.0
	Forward pulse duration, s	0.235	0.246	-4.7
	Avg. vertical acceleration, g	6.1	6.35	-4.1
	Vertical pulse duration, s	0.258	0.246	4.7
Right	Avg. forward acceleration, g	6.0	8.25	-37.5

Doorframe				
	Forward pulse duration, s	0.261	0.245	6.1
	Avg. vertical acceleration, g	7.69	7.71	-0.26
	Vertical pulse duration, s	0.137	0.157	-14.6
Tail	Avg. forward acceleration, g	6.98	6.66	4.6
	Forward pulse duration, s	0.179	0.175	2.2
	Avg. vertical acceleration, g	6.54	7.04	-7.6
	Vertical pulse duration, s	0.218	0.218	-
ELT1	Avg. forward acceleration, g	8.36	8.64	-3.4
	Forward pulse duration, s	0.221	0.223	-0.9
ELT2	Avg. forward acceleration, g	5.53	5.21	5.8
	Forward pulse duration, s	0.213	0.22	-3.3
	Avg. vertical acceleration, g	9.66	13.9	-43.9
	Vertical pulse duration, s	0.161	0.142	11.8
ELT3	Avg. forward acceleration, g	6.37	2.33	63.4
	Forward pulse duration, s	0.214	0.209	2.3
	Avg. vertical acceleration, g	7.7	4.7	39.0
	Vertical pulse duration, s	0.187	0.198	-5.9
ELT4	Avg. forward acceleration, g	6.16	4.0	35.1
	Forward pulse duration, s	0.206	0.191	7.3
	Avg. vertical acceleration, g	5.29	7.24	-36.9
	Vertical pulse duration, s	0.224	0.226	-0.9
ELT5	Avg. forward acceleration, g	7.7	6.8	11.7
	Forward pulse duration, s	0.236	0.24	-1.7
	Avg. vertical acceleration, g	5.54	7.0	-26.4
	Vertical pulse duration, s	0.172	0.17	1.2

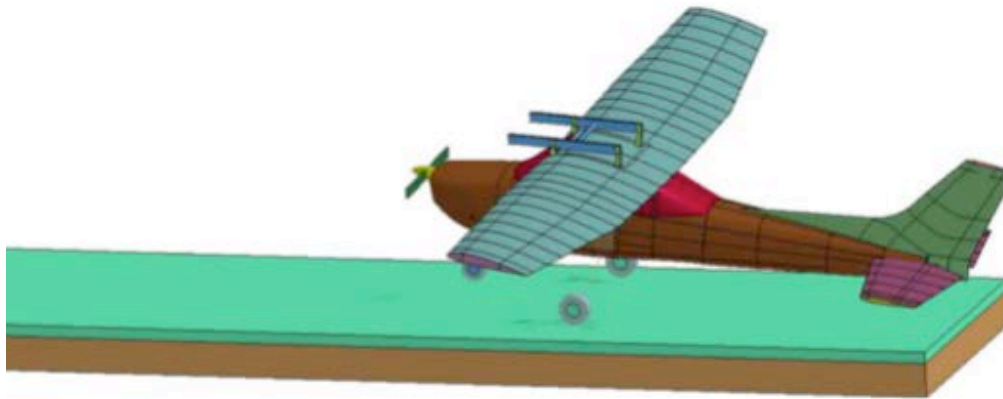
4.6 Modeling and Simulation of Test 3

As mentioned previously, the Test 3 aircraft had several different features as compared with the Test 1 and Test 2 aircraft, including a swept tail, rear windows, and a tubular steel main gear. These configuration changes required modifications to the model that were, again, based on a laser scan of the vehicle geometry. The final LS-DYNA model representing the Test 3 crash is shown in Figure 46. The model consisted of 138,593 nodes; 262 beam elements; 72,804 shell elements; 59,800 solid elements; 53 parts; 21 element masses; 16 material properties; 1 automatic single surface contact; 4 CNRBs; and 41 spot welds. Note that the spot welds were used to replicate the large separation of the tail from the fuselage cabin, which occurred during the test. The model had a nominal element edge length of 1.5-in. The layered soil model was the same as used in the Test 2 simulation. Concentrated masses were used to represent the fuel in the wings and the seats and occupants. Solid elements were used to represent the engine, which had previously been modeled using a concentrated mass.

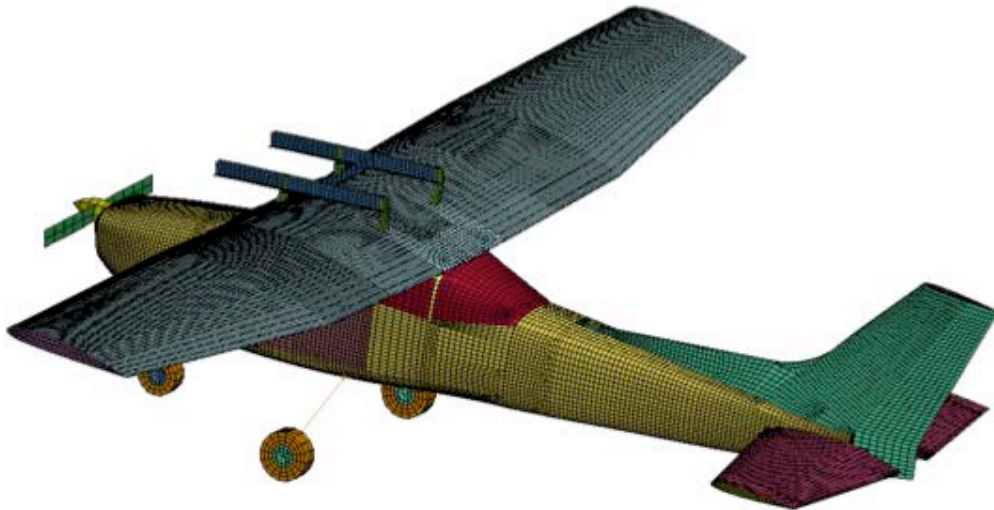
The CG of the aircraft model was assigned an initial condition of 682.8-in/s forward and 283.2-in/s vertical velocities, matching the measured test conditions. In addition, the aircraft model was pitched by 8.0° (nose up) and rolled by 2° (left side down). A pitch angular velocity of +13.3 degrees/s was assigned to the model about its CG. The model was executed on a Linux workstation computer with 8 processors, running LS-DYNA V971 R7.1.2 SMP double precision, and required

approximately 23 hours and 37 minutes of clock time to simulate 0.6 seconds. Nodal output requests for the simulation included vertical and forward acceleration-time histories in the local coordinate systems that were defined at each accelerometer location. Vertical and forward velocity-time-history responses were output from the simulation in the global coordinate system.

Test-analysis comparisons are presented in four categories: inertial properties of the test article and model, a kinematic assessment of the time sequence of events, soil deformations, and time-history plots of vertical acceleration and velocity. For the acceleration time histories, both the test data and analytical predictions (output in the local axis systems) were filtered using a SAE CFC 20-Hz low-pass filter [15]. Since the pitch angle of the aircraft during the time range of interest was not large, the test velocity responses were obtained by integration of the raw acceleration data.



(a) Shaded view of Test 3 model with layered soil.



(b) Discretized view of the Test 3 aircraft without soil.

Figure 46. Test 3 aircraft model.

4.6.1 Test 3 Inertial Properties

Comparisons of test and analysis inertial properties are shown in Table 7. The total weight of the model is 15-lb heavier than the test article, which results in a percentage difference of less than 1%. The CG locations are predicted within 5.9%. These results indicate that the model does a good job of matching the inertial properties of the test article.

Table 7. Test-analysis comparison of inertial properties for Test 3.

Parameter	Model	Test	Difference	%Diff
Weight, lb	2087.0	2072.0	15.0	-0.72
CG _x , in.	42.6	42.5	0.1	-0.24
CG _y , in.	-0.09	0.0	0.09	-
CG _z , in.	53.8	50.8	3.0	-5.9

4.6.2 Test 3 Kinematic Assessment

The time sequence of events, shown in Figure 47, includes four major events: time of initial tail impact, time of nose impact, time of initiation of tail separation, and tail separation at 0.25-s. The model does a good job of matching the times that these events occur, with the exception of the tail impact. In the test, tail impact occurs at 0.03-s; however, in the model it occurs at 0.063-s. The reason for this difference is unknown; however, it is useful to point out that the observed time delay is not evident in the following two events.


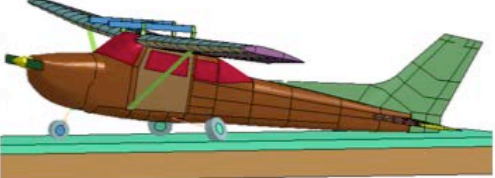

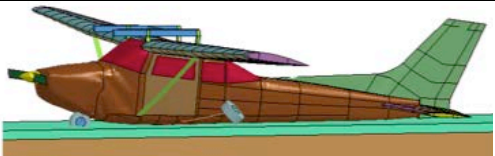

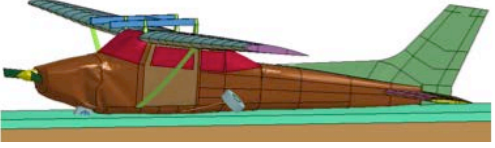

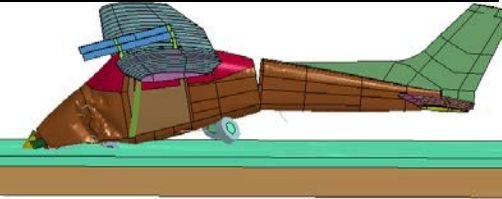
Event	Test	Model
		
Time of initial tail impact, s	0.030-s	0.063-s
		
Time of nose impact	0.116-s	0.120-s
		
Time of initial tail separation	0.138-s	0.135-s
		
Tail separation at 0.25-s	0.25-s	0.25-s

Figure 47. Comparison of time sequence of events for Test 3.

4.6.3 Test 3 Soil Deformation

A photograph is shown in Figure 48(a) depicting the soil deformation pattern post-test. For comparison, a fringe plot of soil deformation in the vertical direction is shown in Figure 48(b) for the model at a time of 0.258-s, which is the time of maximum nose gear deflection. The deepest crater is measured at the point the nose gear digs into the soil. Table 8 shows a comparison of test and analysis soil depth measurements and track distances. In general, the model did a reasonable job of matching the test soil deformation.

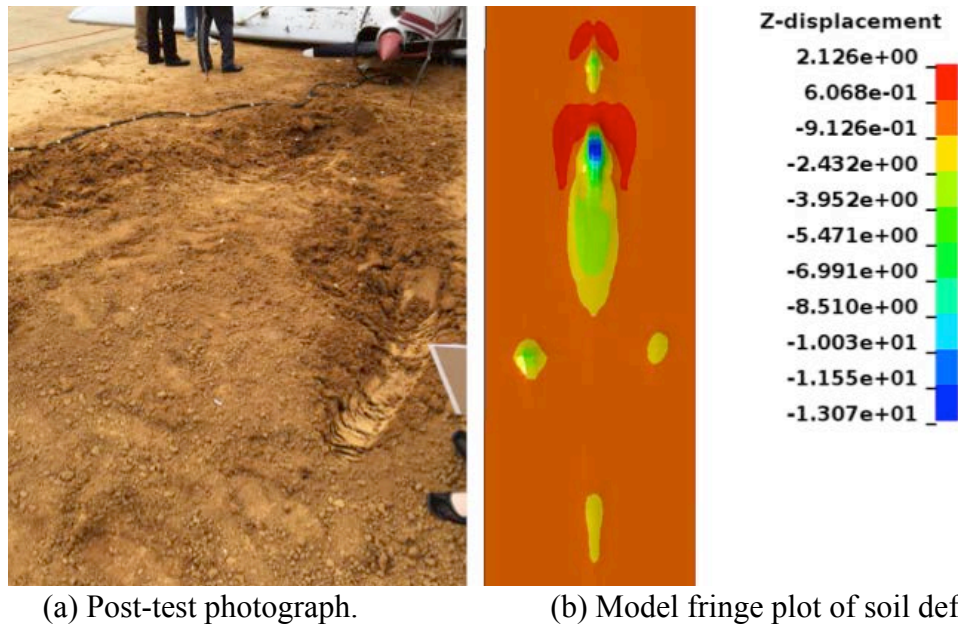


Figure 48. Soil deformation pattern for Test 3.

Table 8. Test-analysis comparison of Test 3 soil depths and track distances.

Parameter	Test	Model	Difference	%Difference
Nose gear hole depth, in.	14	13	1	7.14
Max depth of main gear tire depression, in.	7	5	2	28.6
Distance from tail strike to nose gear hole, in.	299	280	19	6.4
Distance from nose gear hole to spinner post-test, in.	80	63	17	21.75
Distance from the initial main gear tire track to nose gear hole, in.	115	112	3	2.61

4.6.4 Test 3 Time-History Comparisons

Comparisons of vertical and forward acceleration and velocity time-histories are shown in Figures 49-54 for six selected accelerometer locations within the airframe. It should be noted that the experimental and analytical acceleration curves were filtered using an SAE CFC 20-Hz low-pass filter [15]. Experimental velocity data were obtained by integrating the raw acceleration. Analytical velocity data were output directly from the simulation. Analytical accelerations were output in the local coordinate systems defined at each accelerometer location. However, the analytical velocities were output in the global coordinate system. Of the six structural accelerometer locations, the

measured forward velocities, shown in Figures 49(d) through 54(d), do not cross zero velocity, since the plane is still moving forward. Instead, velocity is reduced initially, then at a certain time the forward velocity begins increasing due to rotations of the airframe. The point in time in which the forward velocity starts increasing is different at each location and is most pronounced at the rear of the aircraft as it begins to flip over. For example, it is useful to compare the forward velocity of the DAS box (Figure 51(d)) with the pilot floor location (Figure 49(d)). Likewise, the analytical forward velocity responses approach zero, but do not cross it. Consequently, values of forward pulse duration were estimated based on the forward acceleration and velocity plots. Note that vertical pulse durations were determined using the method shown in Figure 12. Table 9 summarizes the test-analysis data including average acceleration, pulse duration, and delta-V for Test 3. In general, the level of agreement between test and analysis predictions is good for the six structural locations.

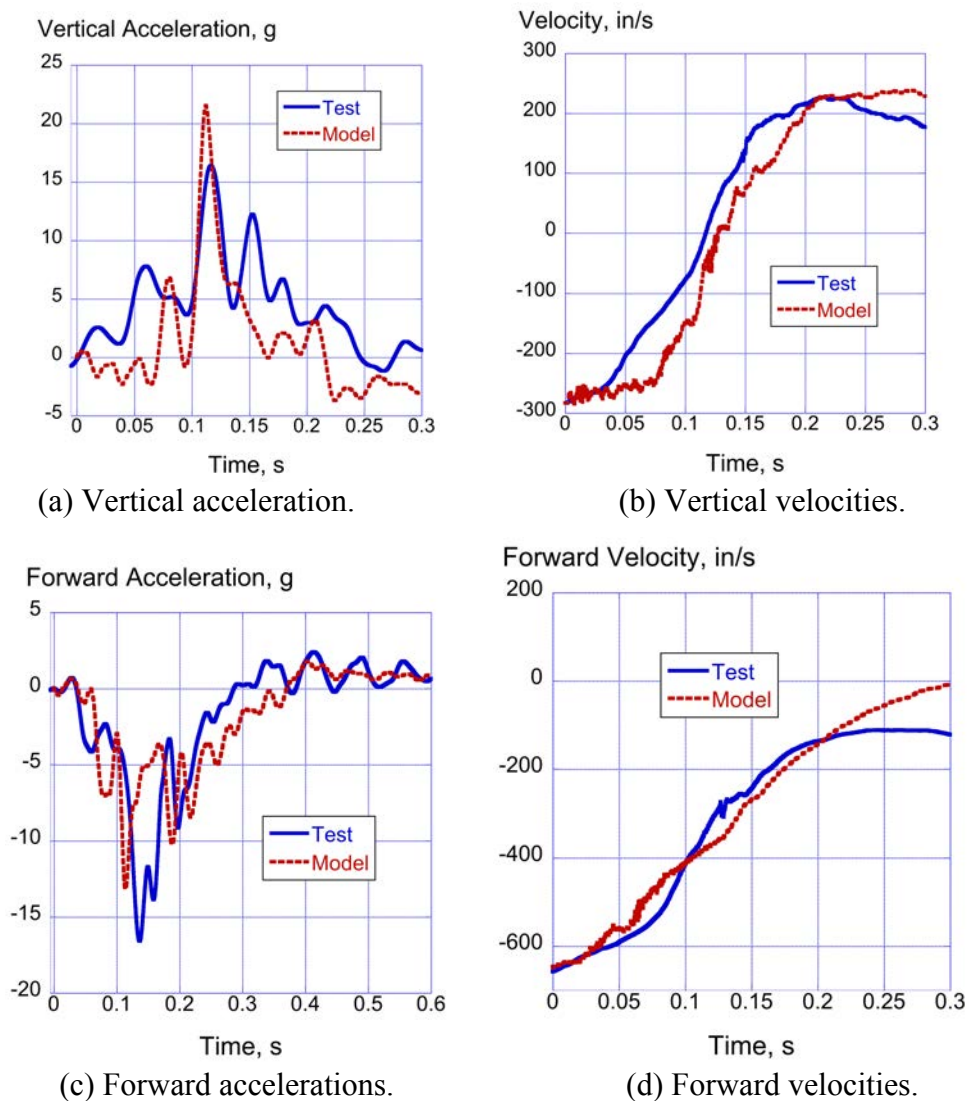
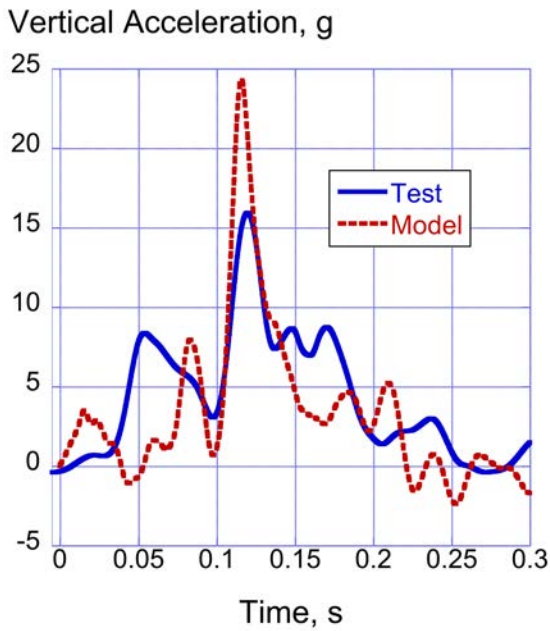
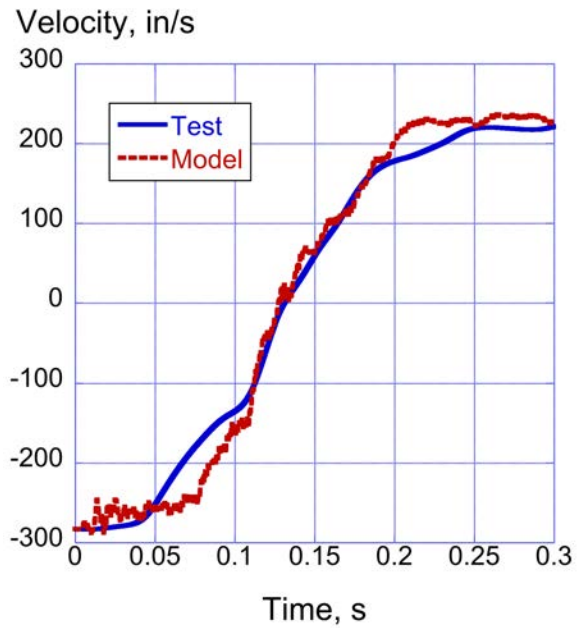


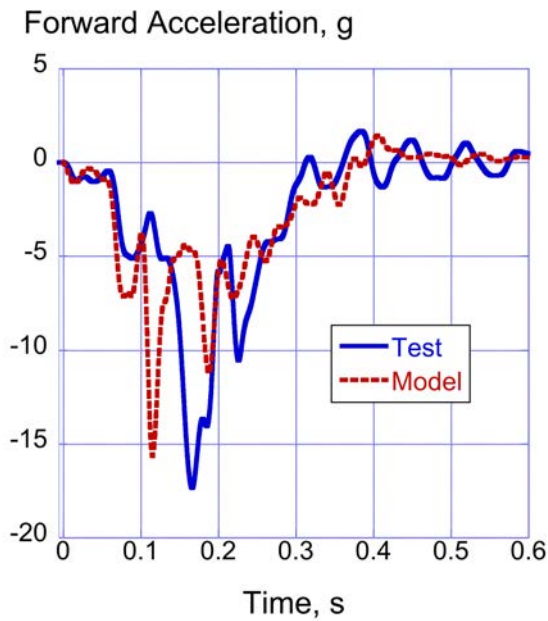
Figure 49. Comparison of vertical and forward acceleration and velocity responses of the pilot floor.



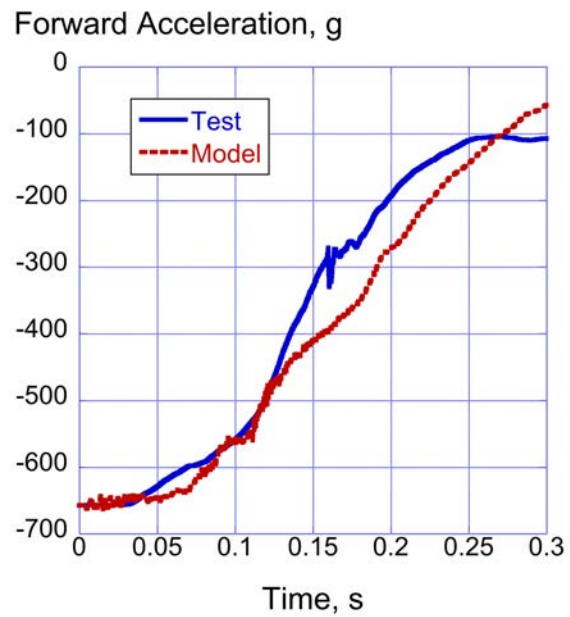
(a) Vertical accelerations.



(b) Vertical velocities.

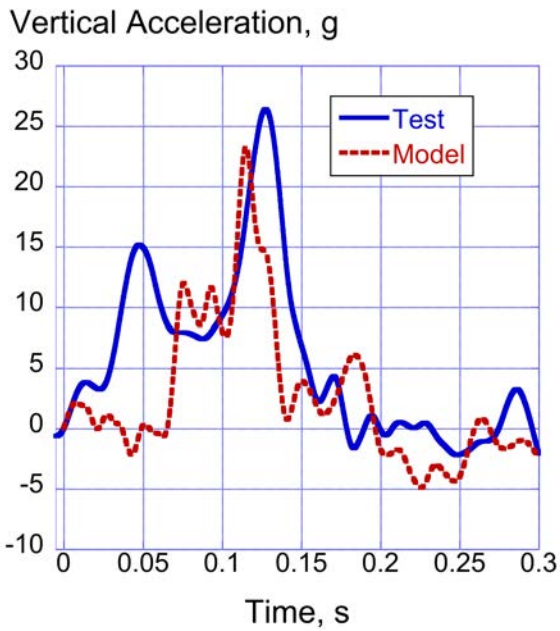


(c) Forward accelerations.

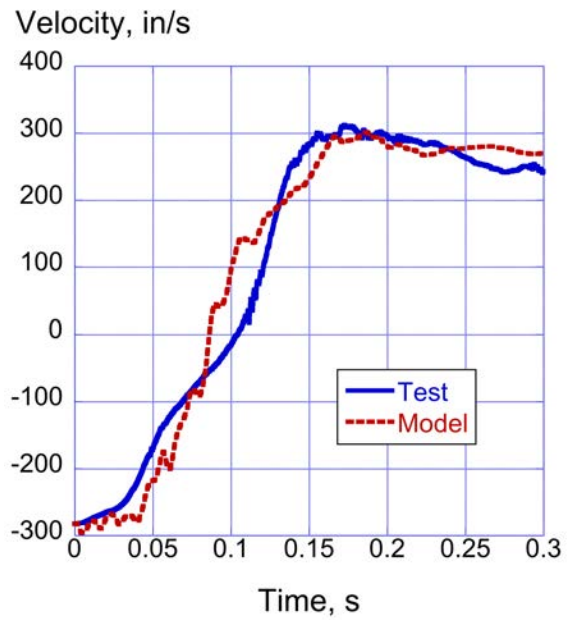


(d) Forward velocities.

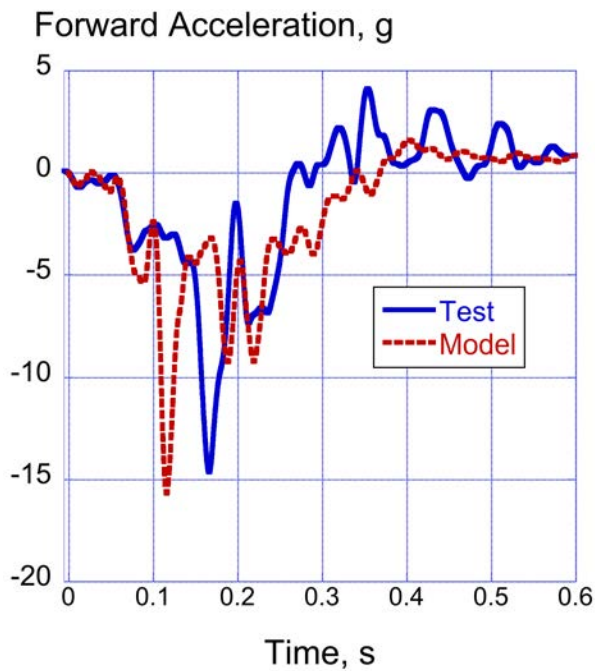
Figure 50. Comparison of vertical and forward acceleration and velocity responses of the copilot floor in Test 3.



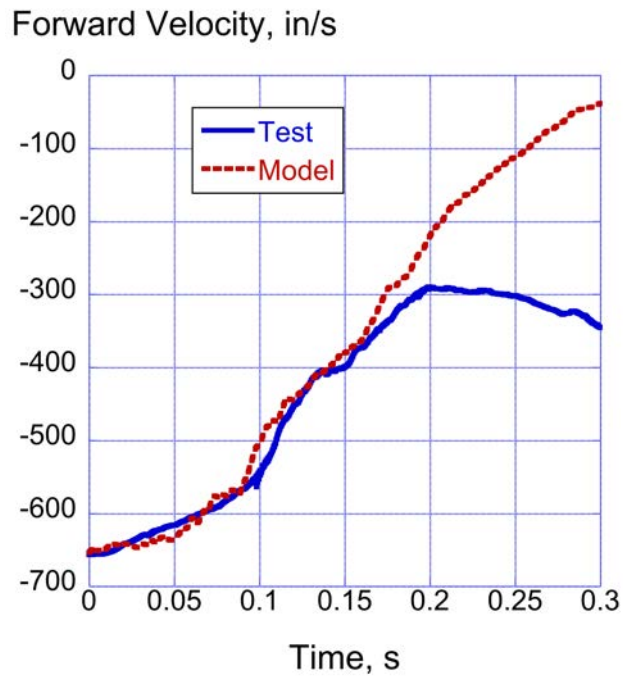
(a) Vertical accelerations.



(b) Vertical velocities.

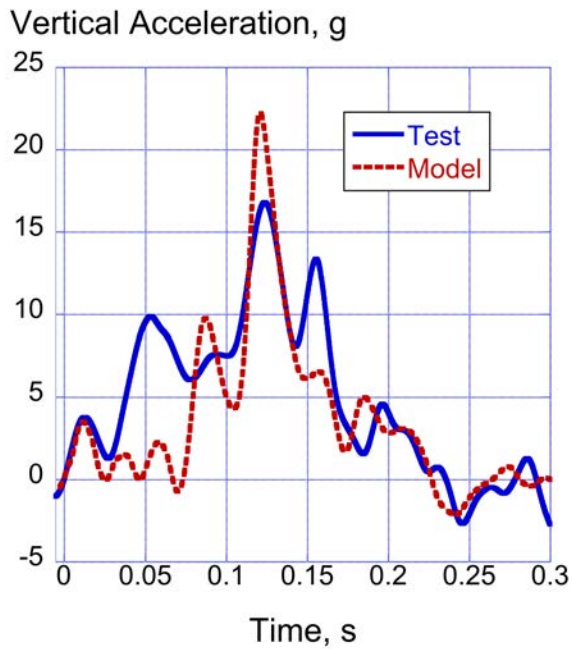


(c) Forward accelerations.

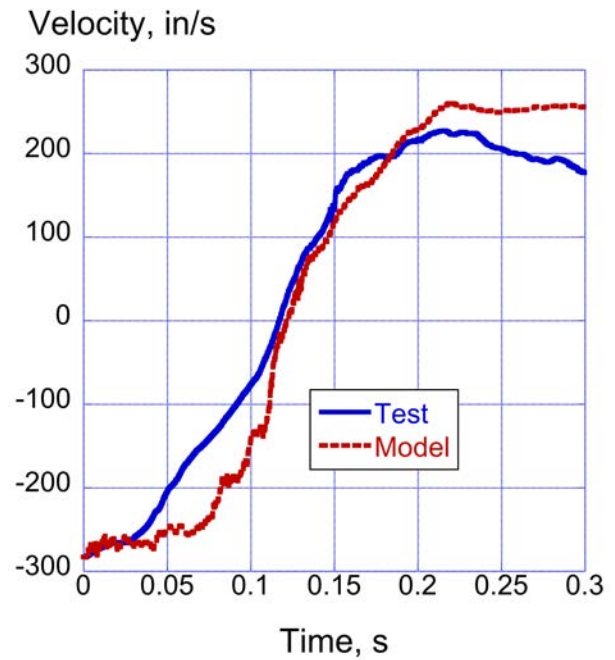


(d) Forward velocities.

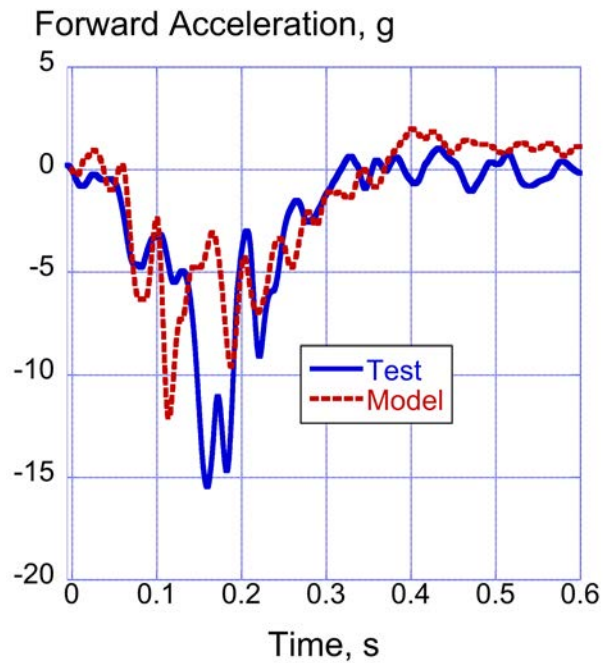
Figure 51. Comparison of vertical and forward acceleration and velocity responses of the DAS box.



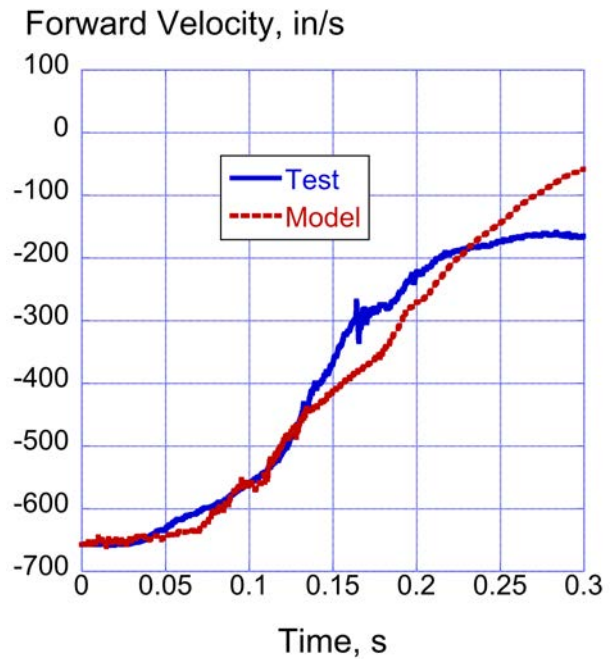
(a) Vertical accelerations.



(b) Vertical velocities.

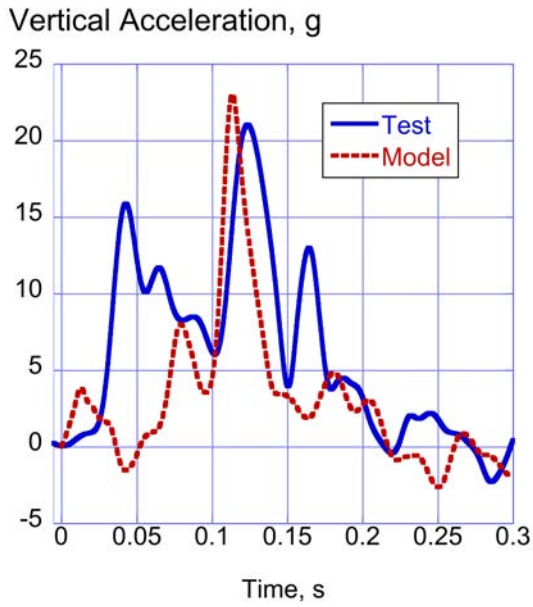


(c) Forward accelerations.

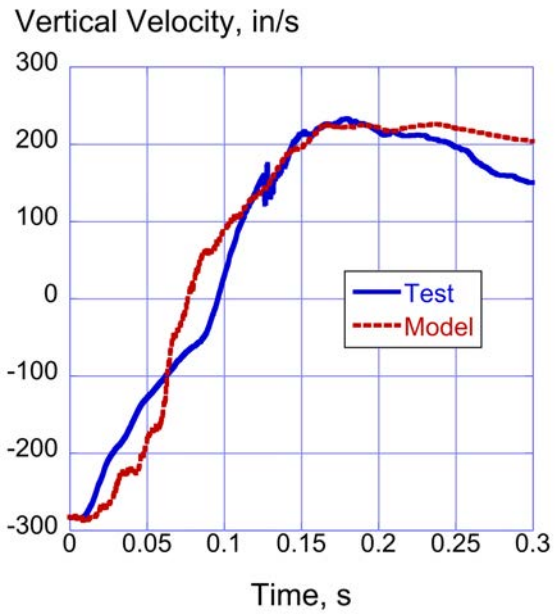


(d) Forward velocities.

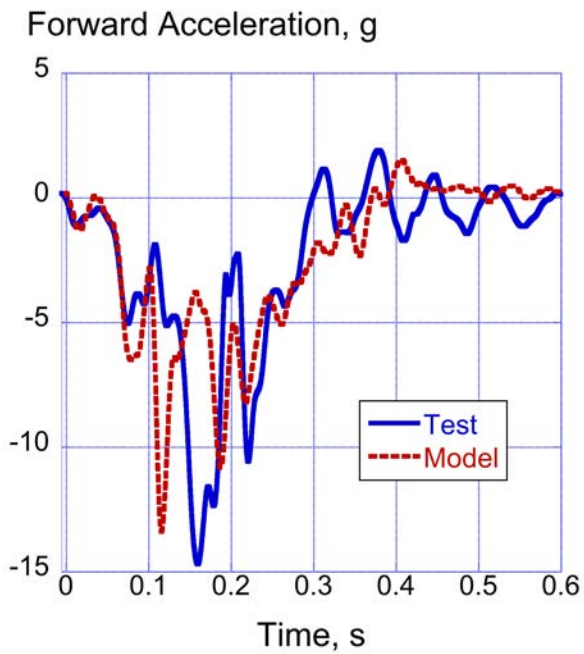
Figure 52. Comparison of vertical and forward acceleration and velocity responses of the left doorframe in Test 3.



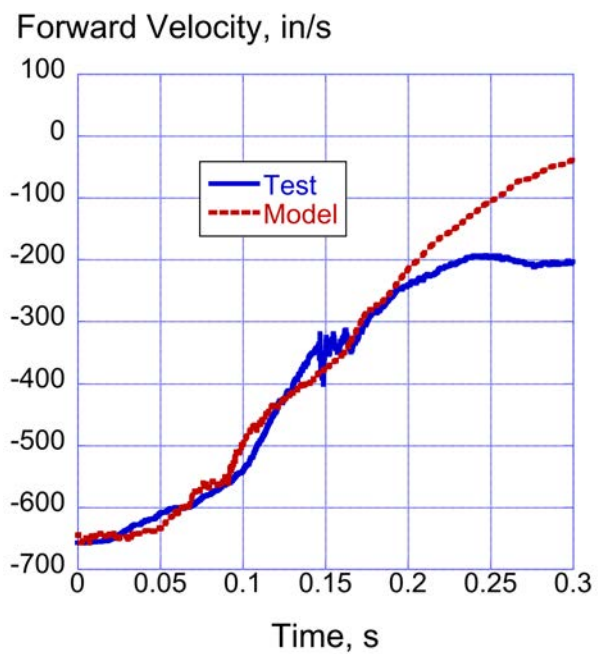
(a) Vertical accelerations.



(b) Vertical velocities.

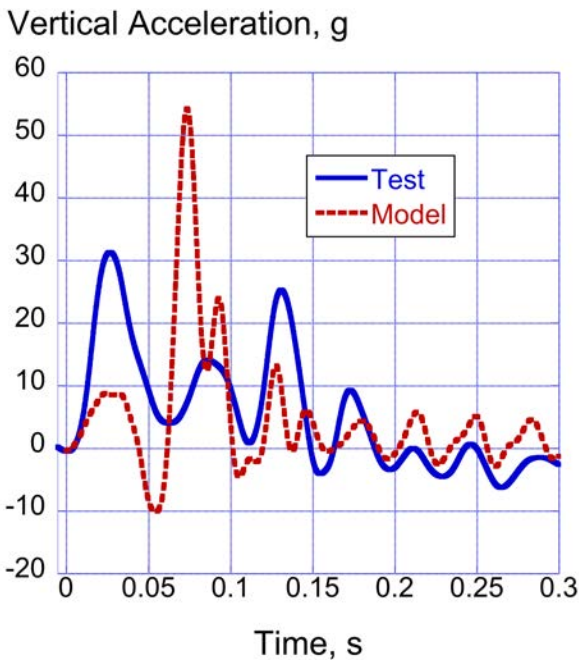


(c) Forward accelerations.

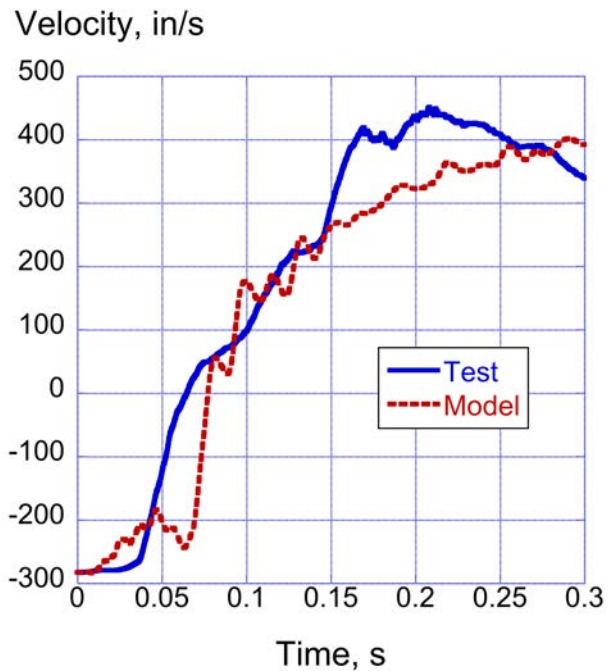


(d) Forward velocities.

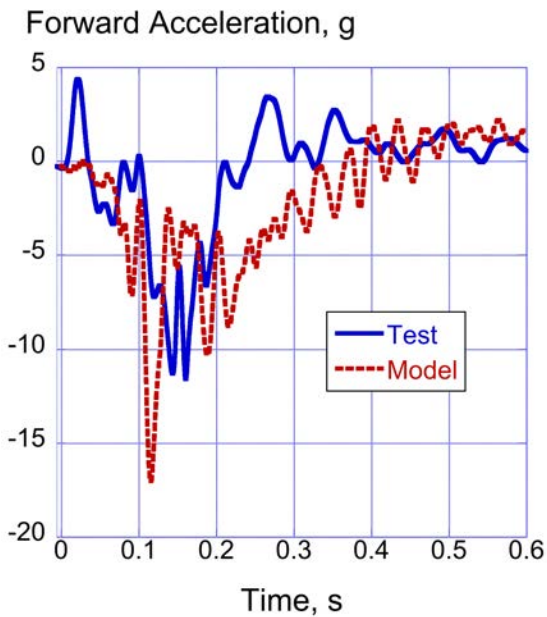
Figure 53. Comparison of vertical and forward acceleration and velocity responses of the right doorframe in Test 3.



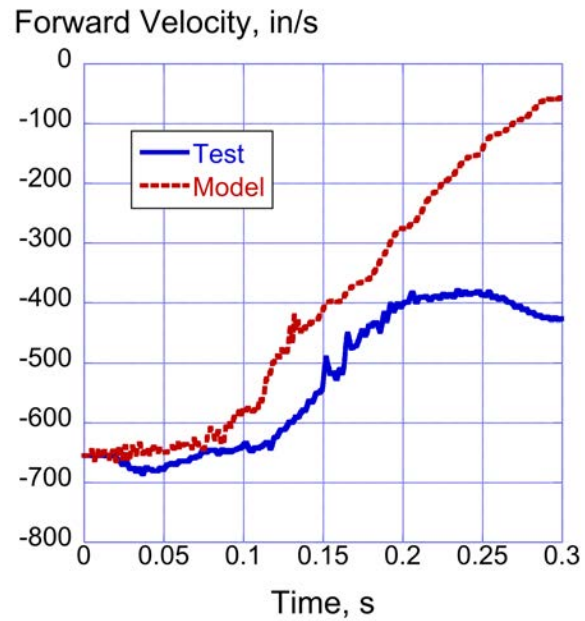
(a) Vertical accelerations.



(b) Vertical velocities.



(c) Forward accelerations.



(d) Forward velocities.

Figure 54. Comparison of vertical and forward acceleration and velocity responses of the tail in Test 3.

Comparisons of the vertical and forward acceleration and velocity responses of the ELTs are shown in Figures 55-59. Once again, the analytical acceleration responses were output in the local coordinate systems defined for each ELT, whereas the velocity responses were output in the global coordinate system. Consequently, the test velocity responses become less accurate as the pitch angle increases due to the gravitational effect on the accelerometers. For ELT numbers and locations, please refer to Figure 9. The level of agreement is better for the sidewall mounted ELTs

than for the floor mounted ELTs; however, overall the predicted responses match the test behavior reasonably well. Note that average accelerations, pulse durations, and delta-V values for both the experimental and analytical velocity responses are included in Table 9. As mentioned previously, forward pulse durations were estimated based on forward acceleration and velocity plots.

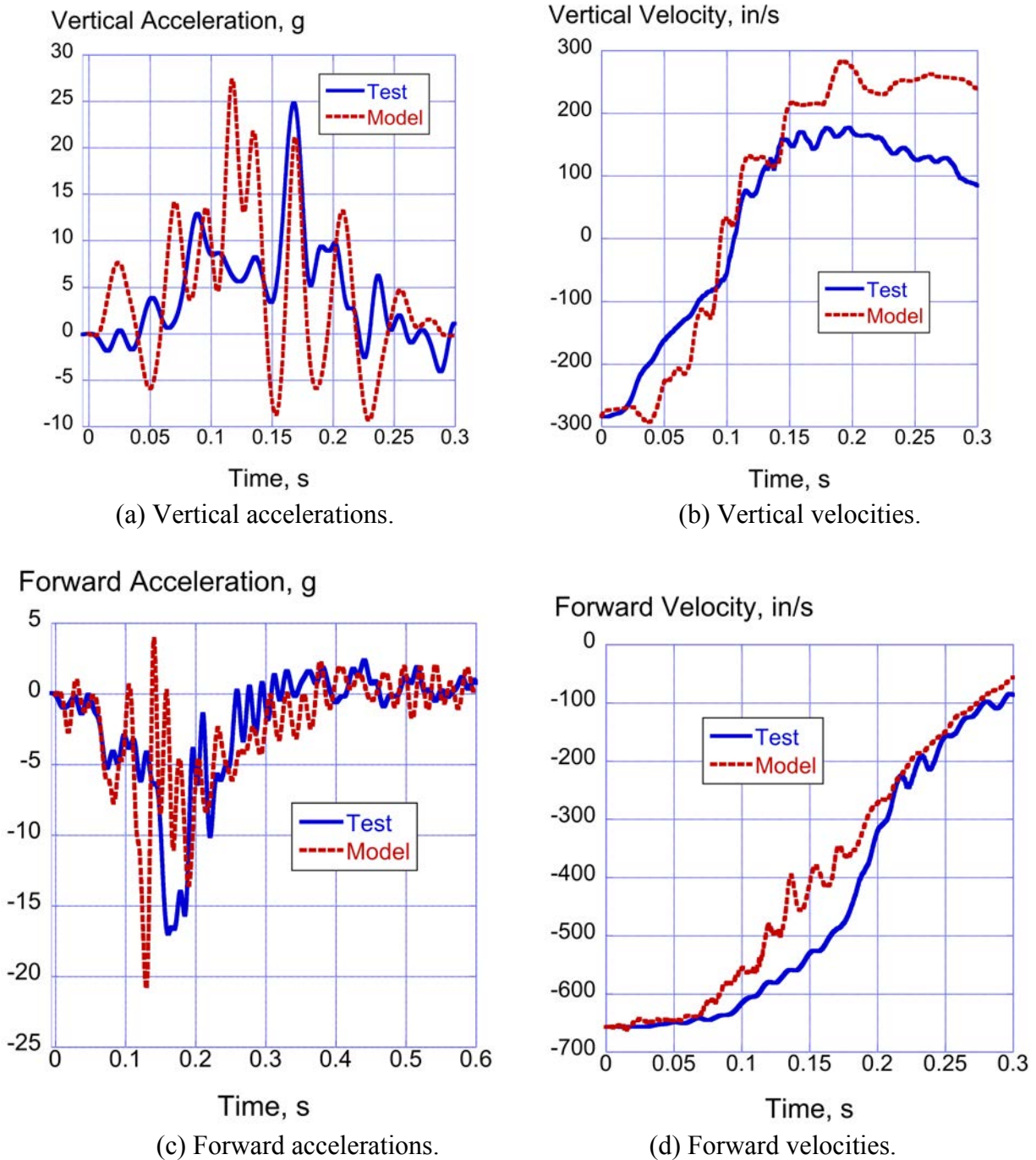
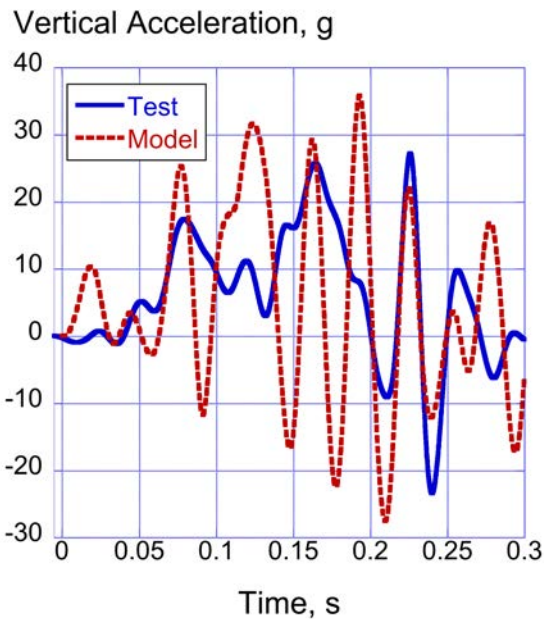
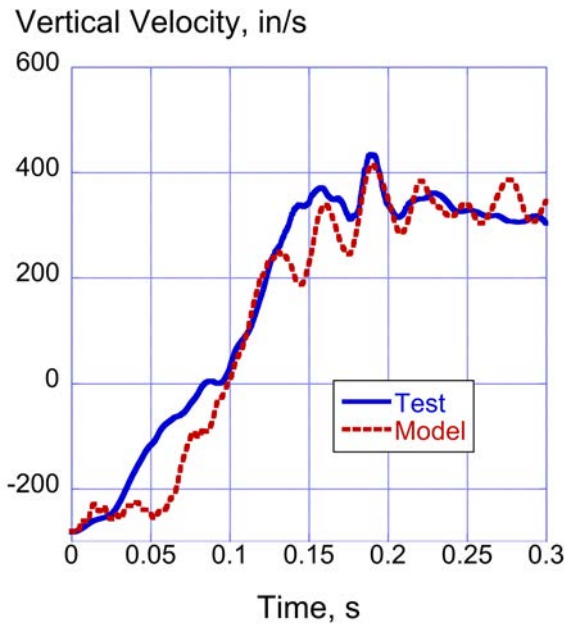


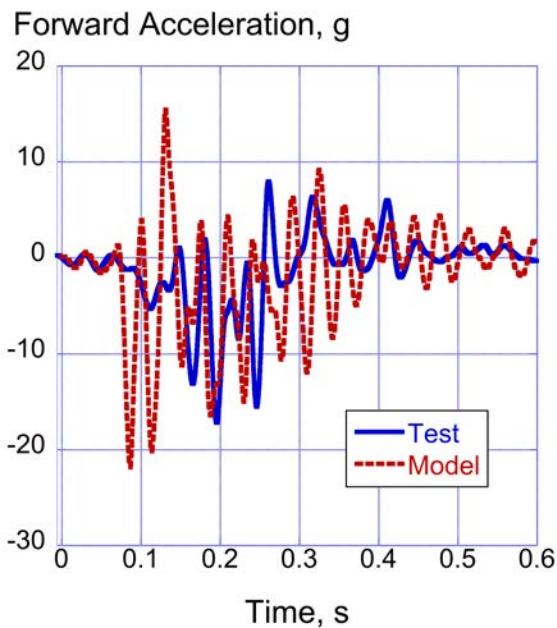
Figure 55. Comparison of vertical and forward acceleration and velocity responses of the left floor ELT1 in Test 3.



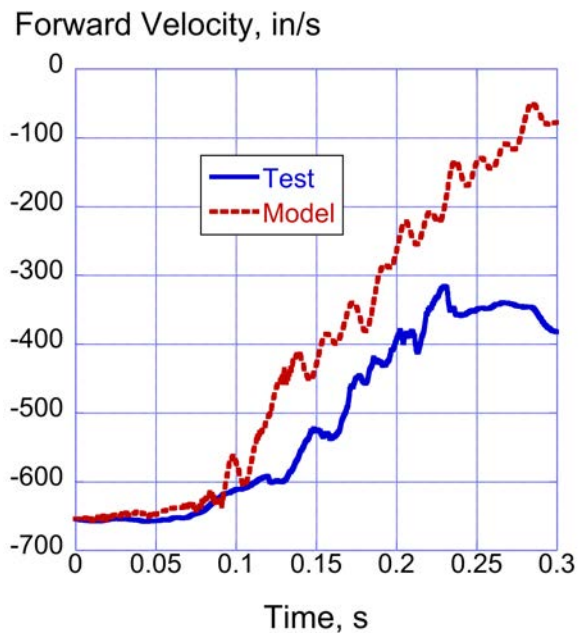
(a) Vertical accelerations.



(b) Vertical velocities.

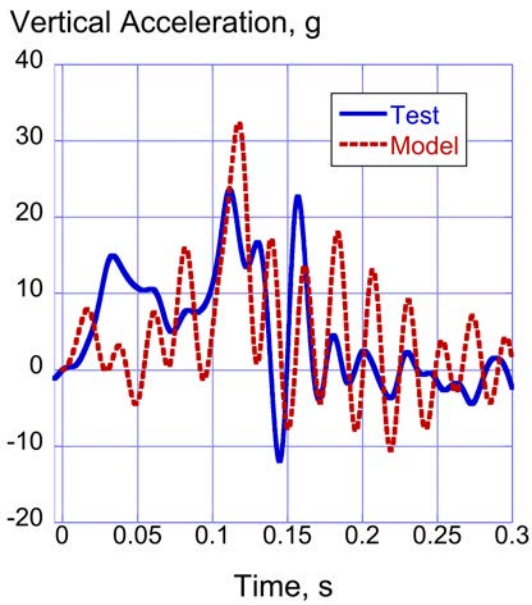


(c) Forward accelerations.

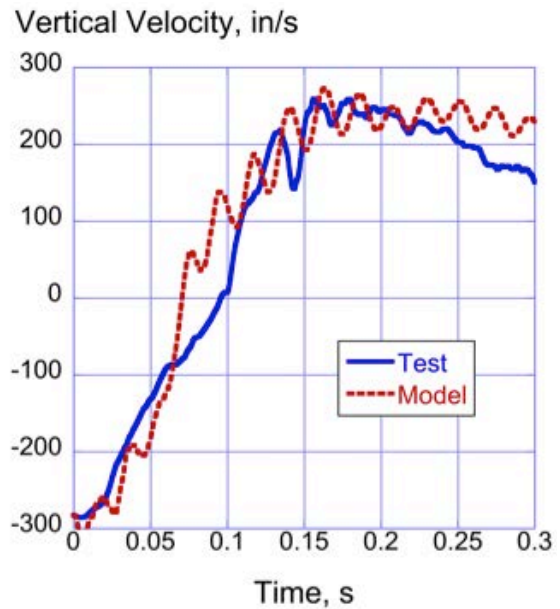


(d) Forward velocities.

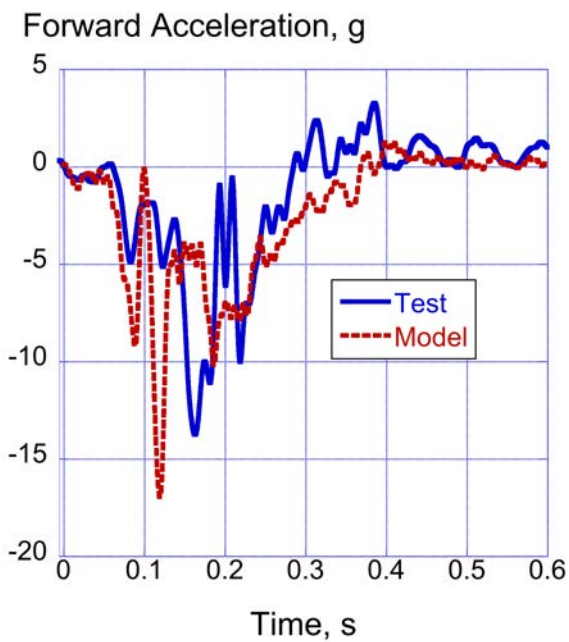
Figure 56. Comparison of vertical and forward acceleration and velocity responses of ELT2 in Test 3.



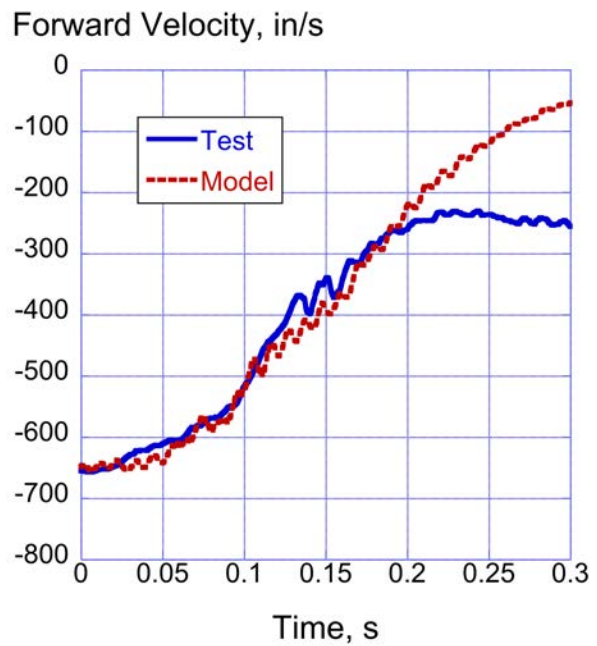
(a) Vertical accelerations.



(b) Vertical velocities.

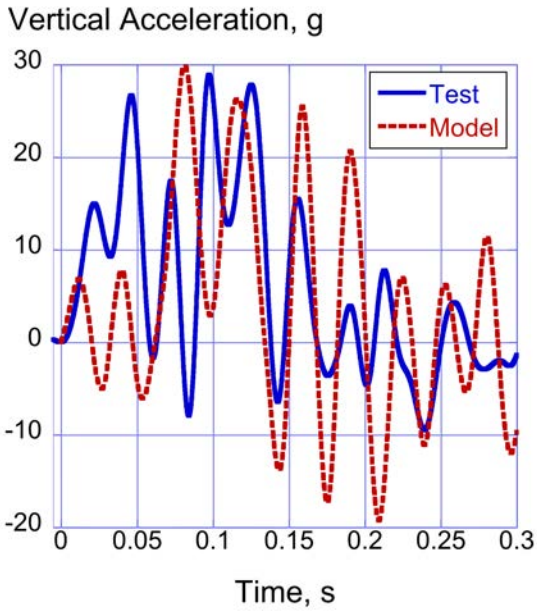


(c) Forward accelerations.

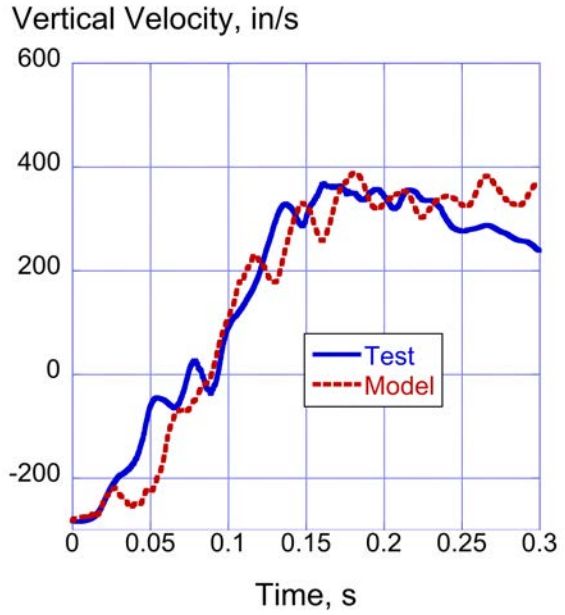


(d) Forward velocities.

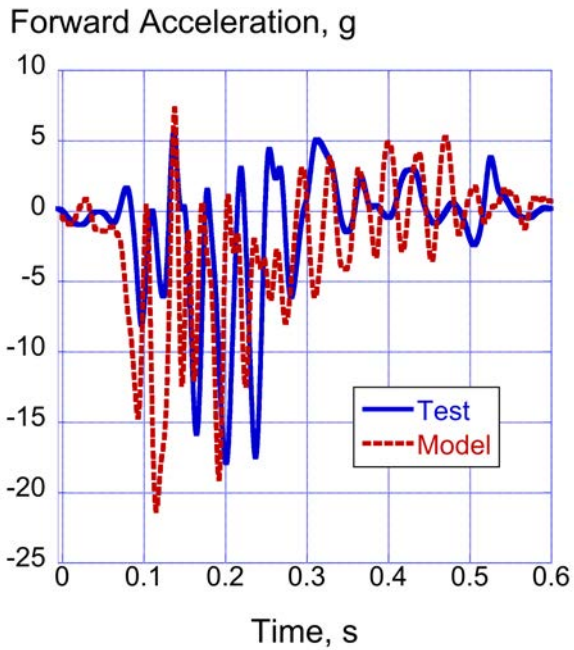
Figure 57. Comparison of acceleration and velocity responses of the right forward sidewall ELT3 in Test 3.



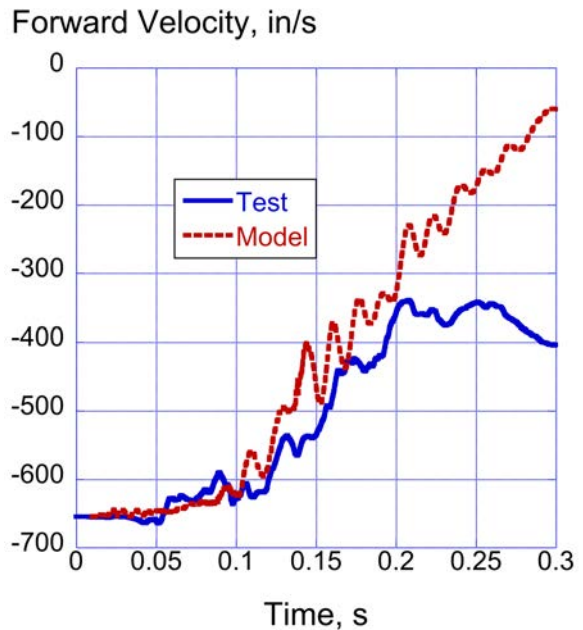
(a) Vertical accelerations.



(b) Vertical velocities.

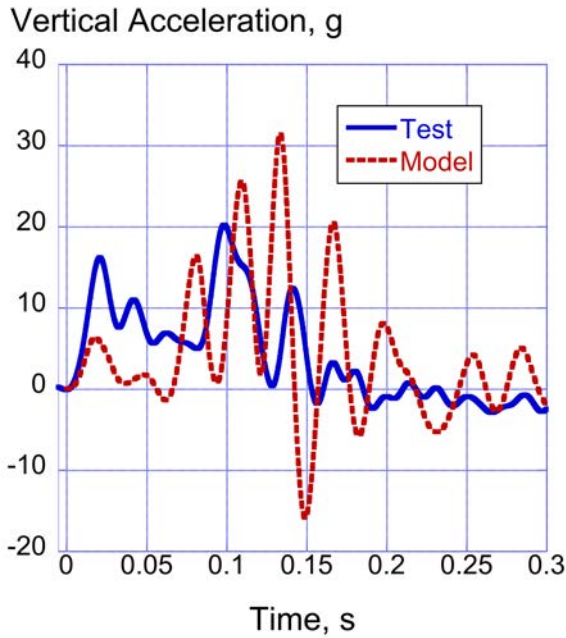


(c) Forward accelerations.

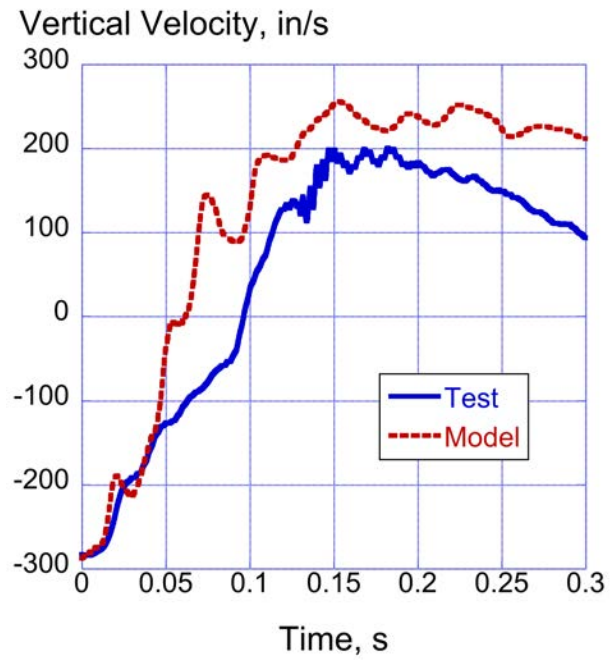


(b) Forward velocities.

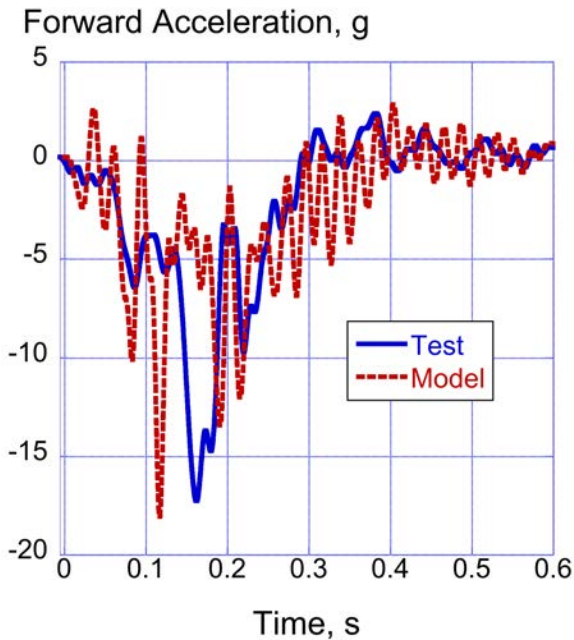
Figure 58. Comparison of acceleration and velocity responses of the left aft sidewall ELT4 in Test 3.



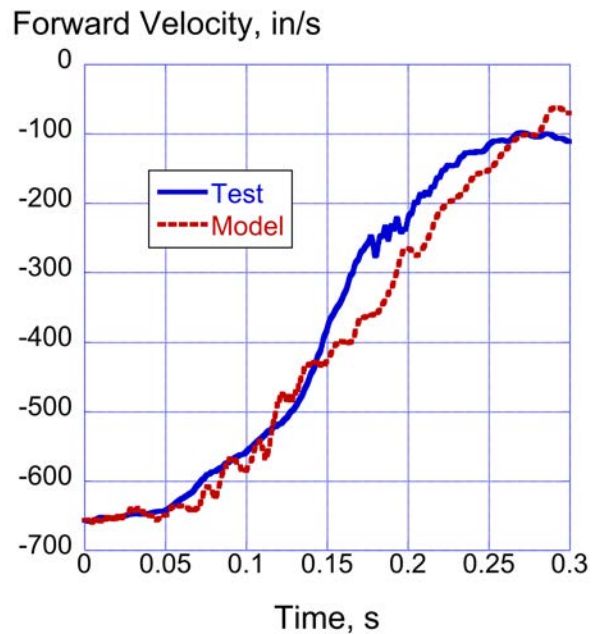
(a) Vertical accelerations.



(b) Vertical velocities.



(c) Forward accelerations.



(b) Forward velocities.

Figure 59. Comparison of vertical and forward acceleration and velocity responses of the right floor ELT5 in Test 3.

Test-analysis metrics for average acceleration, pulse duration, and delta-V are listed in Table 9 for six structural and five ELT channels. For the six structural channels, percentage differences range from a low of -0.65 to a maximum value of -48.7. However, of the 36 parameters listed at these locations, 30 are within $\pm 20\%$. The channels with the highest percentage differences are the average vertical velocity and pulse duration in the tail. These channels are highly sensitive to the

pitch angular velocity, given the fact that the aircraft eventually flipped over. In general, the ELT delta-V responses were well predicted by the model. Of the 10 delta-V parameters listed for ELTs in Table 9, eight are predicted within $\pm 13\%$.

Table 9. Summary of test-analysis comparison metrics for Test 3.

Location	Parameter	Test	Model	% Difference
Pilot Floor	Avg. Vt. Acceleration, g	6.1	6.0	1.6
	Vt. pulse duration, s	0.216	0.22	-1.9
	Vt. delta-V, in/s	509.9	513.2	-0.65
	Avg. Fwd. Acceleration, g	-5.6	-4.5	19.6
	Fwd. pulse duration, s	0.207	0.207	-
	Fwd delta-V, in/s	525.7	525.7	-
Co-pilot floor	Avg. Vt. Acceleration, g	5.0	5.1	-2.0
	Vt. pulse duration, s	0.26	.262	-1.5
	Vt. delta-V, in/s	502.6	516.5	-3.0
	Avg. Fwd. Acceleration, g	-5.78	-5.23	9.5
	Fwd. pulse duration, s	0.269	0.269	-
	Fwd. delta-V, in/s	533.0	533.0	-
Left Doorframe	Avg. Vt. Acceleration, g	6.17	6.4	-3.7
	Vt. pulse duration, s	0.214	0.219	-2.3
	Vt. delta-V, in/s	509.9	541.5	-6.2
	Avg. Fwd. Acceleration, g	-5.1	-4.1	19.6
	Fwd. pulse duration, s	0.276	0.3	-8.7
	Fwd. delta-V, in/s	495.0	598.0	-20.8
Right Doorframe	Avg. Vt. Acceleration, g	7.49	5.01	31.9
	Vt. pulse duration, s	0.178	0.168	5.6
	Vt. delta-V, in/s	514.9	507.4	1.5
	Avg. Fwd. Acceleration, g	-4.9	-4.5	8.2
	Fwd. pulse duration, s	0.19	0.19	-
	Fwd. delta-V, in/s	404.4	404.4	-
DAS Box	Avg. Vt. Acceleration, g	9.8	8.2	16.3
	Vt. pulse duration, s	0.175	0.185	-5.7
	Vt. delta-V, in/s	591.0	583.2	-1.3
	Avg. Fwd. Acceleration, g	3.79	4.19	-10.6
	Fwd. pulse duration, s	0.2	0.2	-
	Fwd. delta-V, in/s	-365.4	-433.49	-18.6
Tail	Avg. Vt. Acceleration, g	8.97	6.1	32.0
	Vt. pulse duration, s	0.21	0.29	-38.0
	Vt. delta-V, in/s	727.6	683.2	6.1
	Avg. Fwd. Acceleration, g	3.49	4.4	-26.1
	Fwd. pulse duration, s	0.2	0.2	-
	Fwd. delta-V, in/s	-255.5	-379.9	-48.7
ELT 1 Pilot Floor	Avg. Vt. Acceleration, g	6.0	6.25	-4.2
	Vt. pulse duration, s	0.197	0.193	2.0
	Vt. delta-V, in/s	458.2	564.9	23.3
	Avg. Fwd. Acceleration, g	3.77	4.06	-7.7

	Fwd. pulse duration, s	0.25	0.25	-
	Fwd. delta-V, in/s	-500.0	-507.8	-1.56
ELT 2 Lt. Aft SW	Avg. Vt. Acceleration, g	7.04	9.2	-30.7
	Vt. pulse duration, s	0.19	0.19	-
	Vt. delta-V, in/s	713.2	695.7	2.4
	Avg. Fwd. Acceleration, g	3.6	4.02	16.3
	Fwd. pulse duration, s	0.23	0.23	-
	Fwd. delta-V, in/s	-335.9	-454.5	-35.3
ELT 3 Rt. Fwd SW	Avg. Vt. Acceleration, g	9.2	6.6	28.3
	Vt. pulse duration, s	0.158	0.16	-1.3
	Vt. delta-V, in/s	538.2	553.2	-2.7
	Avg. Fwd. Acceleration, g	3.81	4.68	-22.8
	Fwd. pulse duration, s	0.2	0.2	-
	Fwd. delta-V, in/s	-395.8	-424.8	-7.3
ELT 4 Rt. Aft SW	Avg. Vt. Acceleration, g	11.6	6.5	44.0
	Vt. pulse duration, s	0.16	0.18	-12.5
	Vt. delta-V, in/s	645.7	668.2	-3.5
	Avg. Fwd. Acceleration, g	2.6	5.54	-113.1
	Fwd. pulse duration, s	0.2	0.2	-
	Fwd. delta-V, in/s	-301.14	-334.11	-10.9
ELT 5 Copilot Flr	Avg. Vt. Acceleration, g	8.8	6.2	29.5
	Vt. pulse duration, s	0.15	0.154	-2.7
	Vt. delta-V, in/s	474.9	536.5	-12.9
	Avg. Fwd. Acceleration, g	5.4	4.75	12.2
	Fwd. pulse duration, s	0.275	0.275	-
	Fwd. delta-V, in/s	-553.85	-556.48	-0.47

Several exterior cameras failed to trigger during Test 3, which limited the amount of photogrammetric data available for analysis. However, following the test, several channels of 3-D photogrammetry data were made available for comparison with global velocity responses from the model. The locations on the airframe where photogrammetry data were analyzed are depicted in Figure 60.

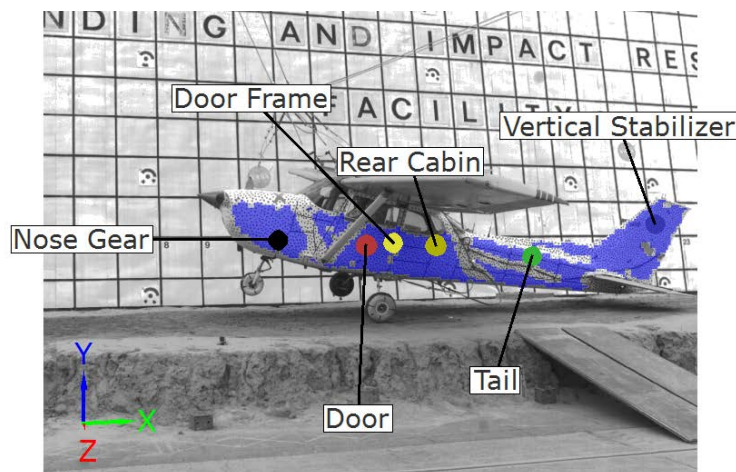


Figure 60. Locations where 3-D photogrammetry data were collected and analyzed.

Test-analysis comparison plots of forward and vertical velocity responses for the doorframe and the tail are shown in Figures 61 and 62, respectively. For these plots, the test velocity responses were obtained from 3-D photogrammetry and the model responses were obtained in the global coordinate system by following the responses of nodes in the model whose locations approximately matched the locations shown in Figure 60. Note that the doorframe location, as shown in Figure 60, is close to the CG of the aircraft.

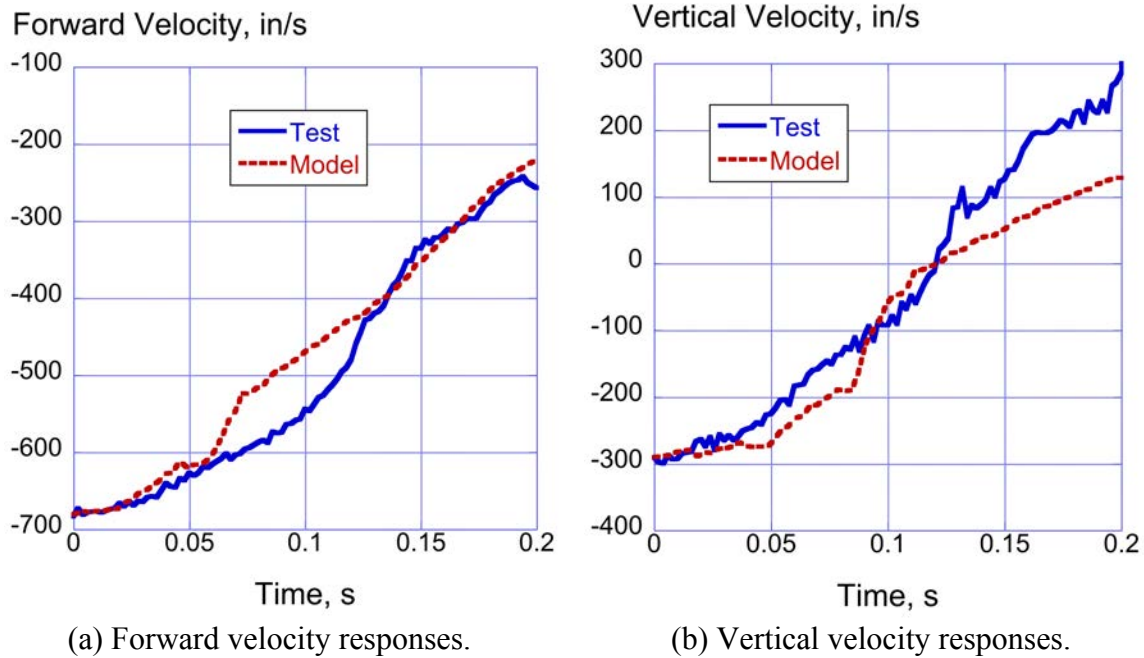


Figure 61. Test-analysis comparisons of forward and vertical velocity responses of the doorframe.

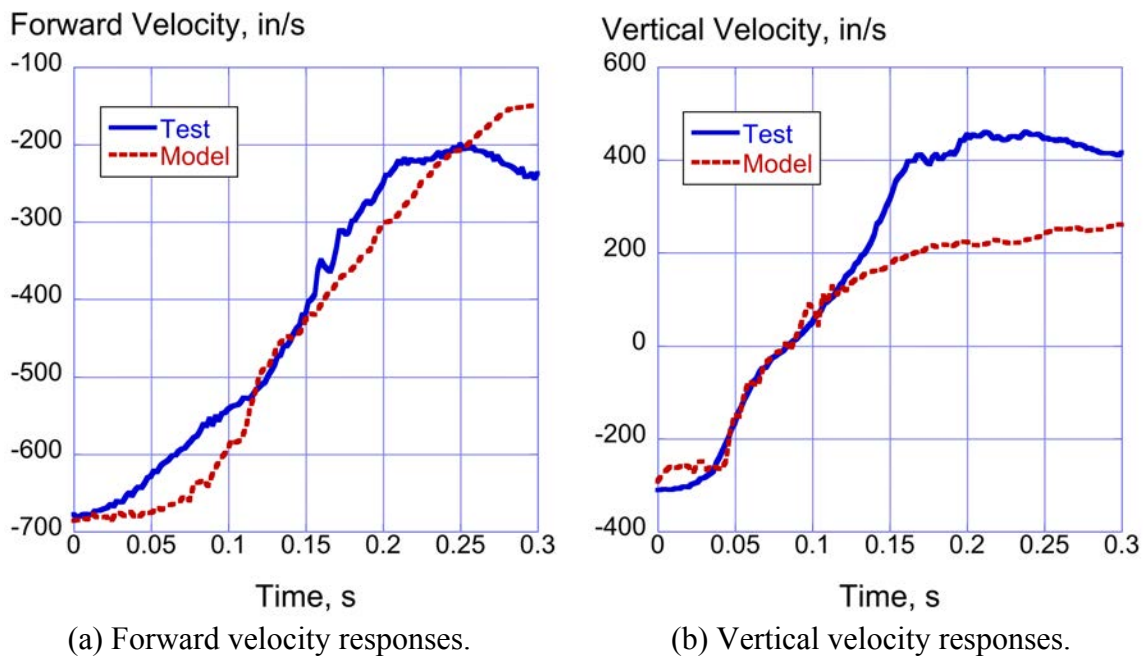


Figure 62. Test-analysis comparisons of forward and vertical velocity responses of the tail.

Reasonable agreement is obtained between the photogrammetry data and the predicted responses for forward and vertical velocity at two locations (the doorframe and the tail) on the airframe. The doorframe responses show generally better agreement than for the tail, mainly because the model under predicts the magnitude of the rebound velocity in the vertical direction. Of course, the tail responses are highly sensitive to the rotational velocity of the vehicle.

5.0 DISCUSSION OF RESULTS

One of the primary objectives of the ELTSAR Study was to develop finite element models of the test articles, to execute simulations replicating the test conditions, and to calibrate the models through extensive test-analysis comparisons. The calibration process was conducted by comparing test-analysis results in four categories: inertial properties, kinematic assessment of the time sequence of events; soil deformation (Test 2 and Test 3 only); and, acceleration and velocity time-history responses. In general, the model calibration was successful. However, it is useful to understand the sources of modeling uncertainty and to list assumptions and approximations used in developing and executing the models. In addition, it is important to understand that other model calibration approaches exist for comparing the level of agreement between two curves, and to provide a rationale for application of the calibration approach used in this study.

5.1 Modeling Uncertainty

Some of the approximations and assumptions used in the models/simulations included:

- While the 3-D laser scan was able to generate accurate outer mold line geometry representing the aircraft, interior structures had to be modeled using hand measurements.
- Rivets, doublers, cutouts, and other detailed features in the model were not included and were instead accounted for by using average thicknesses.
- Lumped masses: Each seat and occupant was simulated as a single lumped mass that was attached to seat tracks on the floor using rigid connections. This approximation is crude as the test dummies are free to move within a limited range, thus changing the load path on the floor. For example, during the swing phase of the drop tests, the occupant's buttocks actually lift off of the seat pans and then slam back down upon impact. This behavior cannot be simulated using the current modeling approach. However, modeling the occupant responses was out of the scope of this study that focused on ELT performance.
- Recall that in Test 2, the nose gear was fixed and attached to the firewall with CNRB's. This representation of the nose gear was an efficient, though not accurate, approach to simulating the actual nose gear in the test article, which was locked into place and not allowed to deform (telescope). The modeling approach does not allow for deformation and failure of the gear support structure. Also, it is important to note that the response of the oleo-pneumatic nose gear is highly velocity dependent. In the Test 1 and Test 3 models, this behavior was only approximated.
- Layered soil was represented as homogeneous within each layer. Cone penetrometer data showed considerable scatter in soil bearing strength with depth. Moisture in the soil changes its properties considerably.
- Following best practices for modeling and simulation, a mesh discretization study should have been performed. However, given the limited amount of time for model development, a mesh discretization study was not performed.

- Soil properties were determined following Test 2 and Test 3. While soil characterization testing was ongoing, people were walking on the soil bed to access and secure the test article. This disturbance of the soil can alter its top-layer properties due to compaction.
- To compare with test, all model accelerations are output in the appropriate accelerometer local-axis system. However, velocities must be compared in the global coordinate system due to problems with integration of the rotating local coordinate system in a gravitational field. This issue was primarily a problem with Test 2 due to the large angles involved; however, velocity comparisons were affected for Test 3, as well.
- Finally, one source of error is that locations in the model for which output were requested did not always match the accelerometer locations in the test article. The DAS box is a worst case example. The DAS box accelerometer for Test 3 is shown in Figure 63(a). The DAS box is essentially an open crate with shelves to hold data acquisition equipment. It was held in place using angle brackets that were attached to fuselage frames. The accelerometer was attached to a vertical frame forming the DAS box crate. In the model, the DAS box was represented as a rigid box made of solid elements, as shown in Figure 63(b). The box in the model was much lower in height than the actual DAS box; however, the material properties assigned to the rigid box matched the total weight of the actual DAS box (106-lb). As shown in Figure 63(b), nodal output was requested from a node located at the mid-point of the top surface of the rigid box. The nodal location does not match the accelerometer location. However, to correct the error would require detailed modeling of the DAS box, which was not done due to time constraints.

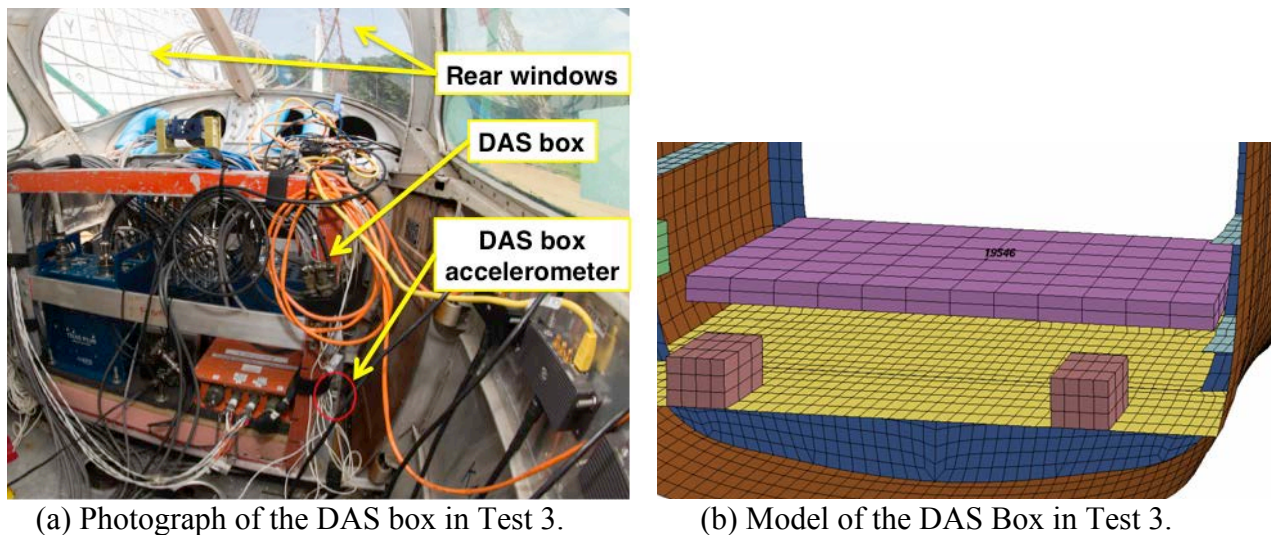


Figure 63. DAS box instrumentation and nodal output comparisons.

5.2 Model Calibration of Time History Responses

There are many approaches available to assess the similarity of two curves. Quantitative correlation metrics in this paper were based on simple percentage differences of parameters including average acceleration, pulse duration and delta-V. While this approach is valid, it should be noted that the level of agreement is magnitude and phase dependent. For example, a test response might have an average magnitude of 5-g, while the corresponding analysis response has an average acceleration of 4-g, a difference of only 1-g. However, the percentage difference between these two values is 20%. Now, consider the case in which the test response had an average acceleration of 50-g and the

corresponding predicted average acceleration was 49-g, again a difference of 1-g. This time the percentage difference is 2%. Thus, an improvement is seen based on the magnitudes of the values being compared. The average vertical accelerations of the six structural accelerometer locations listed in Tables 3, 6, and 9 for Tests 1-3, respectively, were averaged. The results indicate that the average of the average accelerations for Test 1 is 3.98-g, for Test 2 is 5.6-g and for Test 3 is 7.25-g. At these magnitudes, the percentage difference values will be extremely sensitive to minor variations between test and analysis. Finally, it should be noted that some researchers have preferred to use peak acceleration comparisons [13], which were not included in this study.

Time history responses could also be evaluated using the Roadside Safety Verification and Validation Program (RSVVP) [22, 23], which is a software program that automatically assesses the similarities of two curves as part of the validation process of a numerical model. The program allows pre-processing of the two curves, including filtering, phasing, and timing adjustments, etc. Sixteen different metrics are included that are classified into 3 categories: (1) magnitude-phase-comprehensive (MPC) metrics, (2) single-value metrics, and (3) analysis of variance (ANOVA) metrics.

In past simulations, the MPC metric developed by Sprague and Geers [24, 25], which provides a measure of the “goodness of fit” between two curves, was used. Three parameters are calculated over a specified time interval: Sprague and Geers Magnitude (SGM), Sprague and Geers Phase (SGP), and Sprague and Geers Comprehensive (SGC), which is a combination of magnitude and phase. Generally, a value of less than 40 for SGM, SGP, or SGC is considered passing the criteria. Regarding the Sprague and Geers approach, it is important to note that the magnitude and phase metrics are independent of one another. For example, if changes are made to the magnitude of one curve, but the phase information remains the same, only the magnitude metric will change, and visa versa. It should also be noted that if two identical curves are being compared, all three metric values would be zero. Consequently, metric values close to zero are desired. MPC metrics to assess time history comparisons could have been used. However, past experience has shown that the simple percentage difference approach may be a more stringent requirement. Consequently, the percentage difference approach was used.

6.0 CONCLUSIONS

During the summer of 2015, three full-scale crash tests were performed on Cessna 172 aircraft for the purpose of evaluating the impact response of Emergency Locator Transmitters (ELTs) and to generate test data for finite element model calibration. Each test was performed under severe, but potentially survivable, conditions at the Landing and Impact Research facility at NASA Langley Research Center in Hampton, VA. The first test (Test 1) represented a flare-to-stall emergency or hard landing onto a rigid surface. The second test (Test 2) represented a controlled-flight-into-terrain (CFIT) with a nose down pitch attitude of the aircraft, which impacted onto soft soil. The third test (Test 3) also represented a CFIT with a nose up pitch attitude of the aircraft, which resulted in a tail strike condition. Test 3 was also conducted onto soft soil. Each aircraft was configured with two crew seats, two Anthropomorphic Test Devices (ATDs), and 4 to 5 ELTs mounted throughout the interior of the airframe.

Finite element models of the Cessna 172 aircraft were developed for simulation using the commercial nonlinear, transient dynamic finite element code, LS-DYNA[®]. The baseline models were developed from a laser scan of the hardware, and the resulting point cloud was converted to a

geometry file, which was then discretized to a finite element model. The models were then configured to represent the specific test article and impact conditions.

Test 1 essentially represented a “hard” landing. Initially the nose gear tire impacted the concrete, followed closely by impact of the main gear tires. The main landing gear spread outward, as the nose gear stroked vertically. The only fuselage contact with the concrete surface was a slight impact of the rearmost portion of the lower tail. After this impact, the airframe rebounded upward. Acceleration levels for this test were low, ranging from 3.57-g at the pilot floor location to 4.98-g in the tail. The predicted average accelerations showed excellent agreement with the test data, also indicating a range of 3.67-g for the pilot floor location and 4.96-g at the tail. Comparisons of vertical velocity responses were particularly close, with the model capturing the significant change in slope of the vertical velocity response of the tail.

Test 2 represented a 12.2° nose down impact onto soft soil. During the test, the spinner and propeller dug into the soil and served as a pivot point, allowing the entire aircraft to rotate and eventually flip over, coming to rest upside down. A layered soil model was developed for the simulation and several additional changes were made to the Test 1 model to better represent the Test 2 conditions. Test-analysis comparisons were made in four categories: comparison of inertial properties, kinematic assessment, soil deformation, and time-history responses. Findings are listed, as follows:

- The total weight and inertial properties of the model were within 3.3% of the test.
- Kinematic responses were predicted within 0.004-s and overall behavior including tail buckling was captured.
- Soil depths and track distances were predicted within 13%.
- Test-analysis acceleration responses in both the forward and vertical directions were generally well predicted. The analytical responses were obtained from local coordinate systems defined at each nodal position where output was requested,
- Comparison plots of global photogrammetric velocity at the Center-of-Gravity (CG) versus predicted responses from locations near the model CG were plotted. In general, the CG vertical velocity response and the predicted response are in better agreement than the forward velocity responses.

Test 3 was also conducted onto soft soil at an 8° nose up condition. The Test 3 aircraft was a newer model, which contained several features that were different from the Test 1 and Test 2 airframes. These differences included a swept tail versus a straight tail, rear windows, and a tubular steel main gear. The finite element model was modified to account for these and other changes. As before, test-analysis comparisons were made in four categories: comparison of inertial properties, kinematic assessment, soil deformation, and time-history responses. Findings are listed, as follows:

- Total weight and inertial properties of the model matched the test article within 5.9%.
- Four major events were included in the kinematic assessment. The model did a good job of matching the times that these events occur, with the exception of the tail impact. In the test, tail impact occurs at 0.03-s; however, in the model it occurs at 0.063-s. The reason for this difference is unknown; however, it is useful to point out that the observed time delay is not evident in the following two events.
- Soil depths and track distances were predicted within 28.6%.
- Comparisons of local vertical acceleration responses were generally good.
- For Test 3, test-analysis comparisons of the global vertical velocity responses of the ELTs were good. However, the level of agreement is better for the sidewall mounted ELTs than

for the floor mounted ELTs.

- Limited photogrammetric data were obtained during Test 3 due to camera triggering problems. However, photogrammetric forward and vertical velocity data were compared with predicted responses at the doorframe and tail. The predicted responses were obtained from the model in the global coordinate system. Generally good comparison between test and analysis was achieved, except that the model under predicted the vertical rebound velocity at both locations.

This exercise in development and calibration of finite element models to predict full-scale aircraft response during severe, but potentially survivable, crash conditions was successful. Prediction of ELT responses was particularly good. Calibration metrics (average vertical acceleration, pulse duration, and delta-V) were assessed for Test 1 and all metrics were found to compare (test and analysis) within 9.9% for the six structural accelerometer locations. For these same six channels in Test 3, percentage differences range from a low of -0.65 to a maximum value of -48.7. However, of the 36 parameters listed at these locations, 30 were predicted within $\pm 20\%$. In addition, of the 10 delta-V parameters listed for ELTs in Test 3, eight are predicted within $\pm 13\%$. Based on the level of test-analysis agreement demonstrated, the models were used to assess ELT responses under a variety of impact conditions and surfaces not feasible for testing within resource constraints.

7.0 ACKNOWLEDGEMENTS

The ELTSAR Study under the Search and Rescue Program located at NASA Goddard Space Flight Center funded this research. Thanks to the SAR Program and ELTSAR management for their support and all of the engineers and technicians at the NASA LandIR facility for working with the utmost competence and efficiency to achieve three successful tests within an 8-week time period.

8.0 REFERENCES

1. Stimson C.M., Littell J. D., Annett M. S., Jackson K. E., Mason B. H., Templeton J.D., and Fasanella E. L., "Emergency Locator Transmitter Survivability and Reliability Study," NASA-TM-2016-000000, In Publication.
2. Annett M.A., Littell J. D., Stimson C. M., Jackson K.E., and Mason B.H., "Full-Scale Crash Tests and Analyses of Three High-Wing Single Engine Aircraft," Aerospace Structural Impact Dynamics International Conference, Seville, Spain, November 17-19, 2015.
3. Littell J. D., "Crash Tests of Three Cessna 172 Aircraft at NASA Langley Research Center's Landing and Impact Research Facility," NASA/TM-2015-218987, November 2015.
4. Littell J. D., and Stimson C. M., "Emergency Locator Transmitter System Performance During Three Full-Scale General Aviation Crash Tests," NASA/TM-2016-000000. In publication.
5. Littell J. D. and Annett M. S., "ATD Occupant Responses from Three Full-Scale General Aviation Crash Tests," NASA/TM-219175-2016, March 2016.
6. Littell J. D., "Experimental Photogrammetric Techniques used on Five Full-Scale Aircraft Crash Tests," NASA/TM-219168-2016, March 2016.

7. Hallquist J. Q., "LS-DYNA Keyword User's Manual," Volume I, Version 971, Livermore Software Technology Company, Livermore, CA, August 2006.
8. Hallquist J. Q., "LS-DYNA Keyword User's Manual," Volume II Material Models, Version 971, Livermore Software Technology Company, Livermore, CA, August 2006.
9. Cessna Skyhawk Information Manual, 1980 Model 172N, Cessna Aircraft Company, Wichita, Kansas, 1991.
10. https://en.wikipedia.org/wiki/Cessna_172.
11. Thomson R. G., and Goetz R. C., "NASA/FAA General Aviation Crash Program – A Status Report," *Journal of Aircraft*, Vol. 17, No. 8, pp. 584-590, August 1980.
12. Vaughan V.L., and Hayduk R. J., "Crash Tests of Four Identical High-Wing Single-Engine Airplanes," NASA TP-1699, August 1980.
13. Wittlin G., Gamon M. A., and LaBarge W. L., "Full-Scale Crash Test Experimental Verification of a Method of Analysis for General Aviation Airplane Structural Crashworthiness," FAA-RD-77-188, February 1978.
14. Jackson K. E., and Fasanella E. L., "Crash Simulation of Vertical Drop Tests of Two Boeing 737 Fuselage Sections," DOT/FAA/AR-02/62, August 2002.
15. Society of Automotive Engineering (SAE) J211-1 Instrumentation for Impact Test – Part 1- Electronic Instrumentation, Revision March 1995, SAE International, 400 Commonwealth Drive, Warrendale, PA.
16. Jackson K. E., and Fasanella E. L., "Crash Testing and Simulation of a Cessna 172 Aircraft: Hard Landing Onto Concrete," Proceedings of the 14th International LS-DYNA Users Conference, Dearborn, MI, June 13-14, 2016.
17. RTCA DO-204A/EUROCAE WG-98, "Aircraft Emergency Locator Transmitters (ELTs)," May 1, 2014, Annapolis, MD.
18. Fasanella E. L., and Jackson K.E., "Crash Testing and Simulation of a Cessna 172 Aircraft: Pitch Up Impact onto Soft Soil," Proceedings of the 14th International LS-DYNA Users Conference, Dearborn, MI, June 13-14, 2016.
19. Thomas M. A., Chitty D. E., Gildea M. L., and T'Kindt C. M. "Constitutive Soil Properties for Unwashed Sand at Kennedy Space Center," NASA/CR-2008-215334, Applied Research Associates, Inc., Albuquerque, NM, 2008.
20. Heymsfield, E., Fasanella, E. L., Hardy, R. C., and Boitnott, R. L., "Assessment of Soil Modeling Capability for Orion Contingency Land Landing," ASCE Journal of Aerospace Engineering, Vol. 25, No. 1, pp. 125-131, January 2012.

21. Fasanella, E. L., Jackson, K. E., and Kellas, S. "Soft Soil Impact Testing and Simulation of Aerospace Structures," Proceedings of the 10th International LS-DYNA Users Conf., Dearborn, MI, Livermore Software Technology Corp., Livermore, CA, 2008.
22. Mongiardini M., Ray M.H., Anghileri M., "Development of a Software for the Comparison of Curves During the Verification and Validation of Numerical Models," Proceedings of the 7th European LS-DYNA Conference, Salzburg, Austria, May 14-15, 2009.
23. Marzougui D., Kan C-D, and Opiela K.S., "Comparison of the Crash Test and Simulation of an Angle Impact of a 2007 Chevrolet Silverado Pick-Up Truck into a New Jersey-Shaped Concrete Barrier for MASH Conditions," National Crash Analysis Center NACA 2010-W-001 Working Paper, July 2012.
24. Sprague M.A., and Geers T. L., "Spectral Elements and Field Separation for an Acoustic Fluid Subject to Cavitation," *Journal of Computational Physics*, Vol. 184, 2003, pp: 149-162.
25. Schwer L.E., "Validation Metrics for Response Histories: Perspectives and Case Studies," *Engineering with Computers* (2007), 23:295-309.

APPENDIX A

Coaxial Cable Responses

The ELTSAR management team was interested in simulating ELT antenna and coaxial cable responses. An LS-DYNA model was constructed to simulate the coaxial cable that is used to connect the ELT to its antenna. The goal of the model was to provide dynamic inertial forces in the cable due to the impact and to calculate tensile forces that might occur due to structural deformations of the airframe.

A beam element model was constructed in LS-DYNA for the Harbour Industries M17/60-RG142 cable that is manufactured according to military standard MIL-DTL-17. The cable is 0.195-in. in diameter. The density of the cable was calculated by weighing a 10-in.-long cable and dividing by the volume. In the English system, the consistent system of units are mass (weight in lbf/g), i.e. lbf-s²/in, length in inches, and time in seconds. Thus, the weight density is 0.1 lb/cubic in., but the LS-DYNA model requires input of the mass density, and hence the weight density must be divided by $g=386.4 \text{ in/s}^2$. Consequently, the mass density of the cable is $2.84 \text{ e-4 lbf-s}^2/\text{in}^4$. The coaxial cable model is simplified to be a smeared model, meaning that the inner copper wire, the inner insulator, the outer copper sheath, and the outer plastic cover (jacket) were not modeled individually. The elastic modulus was determined from the Amphenol catalog W1 (Reference A1) of a similar radio frequency Teflon-based coaxial cable. The smeared Young's Modulus of 60,000 psi (similar to Teflon) and the density were the two primary properties in the model. Failure was added by using a *MAT_ADD_EROSION card that can delete elements once a given property is exceeded. For the cable, the failure strain and the maximum tensile strength are the logical properties for erosion. A failure strain of 15% was assumed and a maximum strength of 2000 psi was found in the Amphenol catalog. A simple calculation would indicate that the failure force for the 0.195-in.-diameter cable would be approximately 60 pounds sustained force. The cable model could not be compared with any direct experimental data as the ELT's were active and the coaxial cable could not be cut to insert a force transducer. However, in some tests, dummy ELT's were used with cables that were split with an inline force transducer. These force transducers produced dynamic vibratory forces in the same range as the simulations (generally with high frequency peaks under 20 pounds).

The Test 1 impact (not including the restraining net forces) did not produce accelerations or deformations that would overstress the coaxial cables. Several of the actual cables in Test 2 were modeled with the cables routed as closely as possible to those in the aircraft. Some of the cables were routed through holes in the aircraft frames (see Figure A1). Modeling side contact of the beam-element cable with a shell element adjacent to the hole is not trivial. Dummy beam elements had to be inserted around the perimeter of the hole or else the beam did not recognize contact with the shell element. Also, note the two cables between the second and third frames in Figure A1. One cable is taut (straight) and the other is curved (slack). The vibratory forces on the slack cable are actually higher and at lower frequency as can be seen in Figure A2. The cable behaves like a guitar string where a tight string vibrates at a higher frequency. Although Test 2 into soil was a severe crash with major tail buckling, the coaxial cables did not go into tension, see Figure A3. Instead, the long cable that goes between frames where the buckle occurred actually goes slack when the tail buckles. This behavior is illustrated in Figure A4 where the outer skin has been removed so that the coaxial cables can be viewed. The inertial dynamic vibratory forces were insufficient to produce failure [1, 4]. Note that a failure based on strain is superior to failure based

on stress. A material can withstand high stresses (forces) for a short amount of time (milliseconds) if very little strain results.

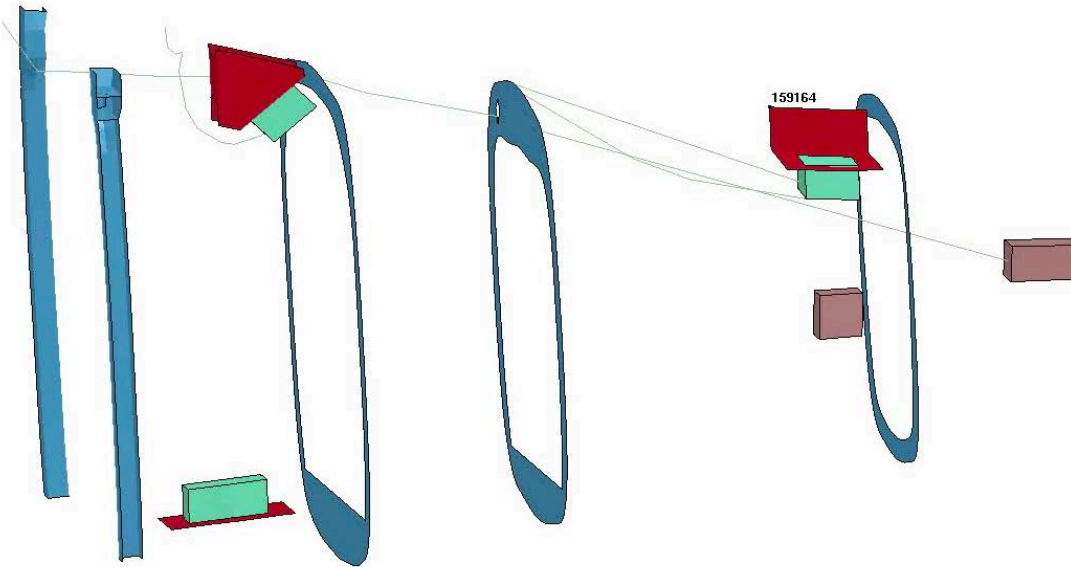


Figure A1. Note various coaxial cables modeled for Test 2 including cable running through a hole in the middle frame. Also, note some of the cables have considerable slack built in.

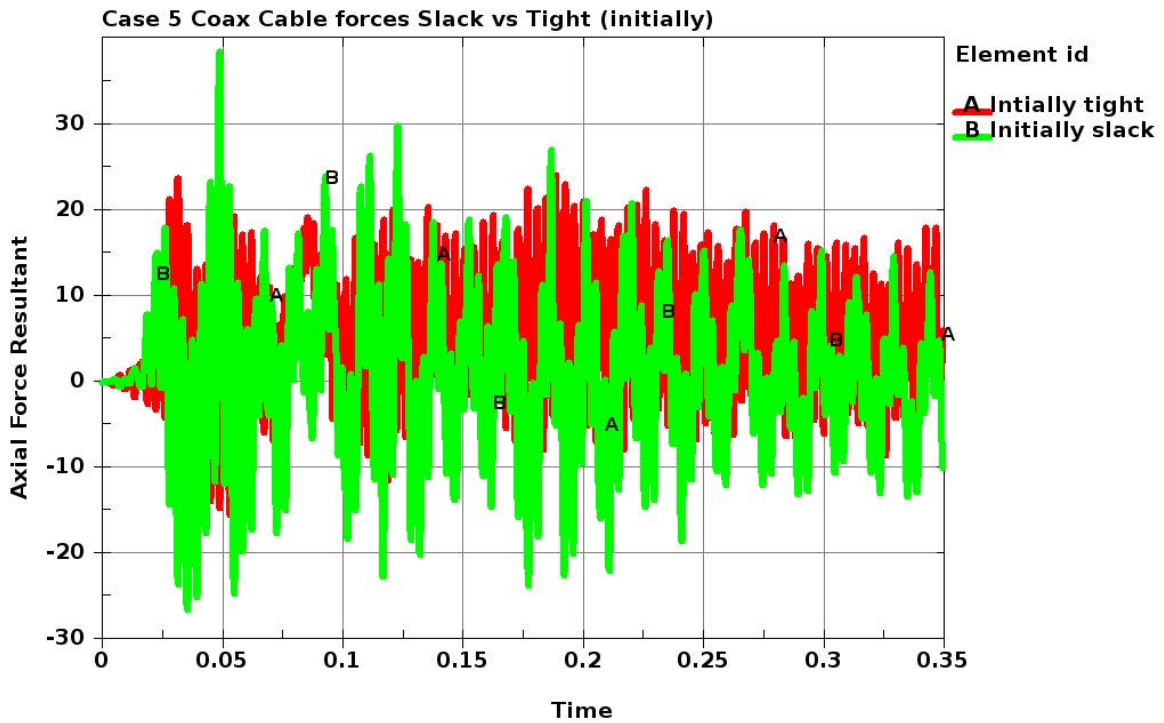


Figure A2. Dynamic force and frequency response, taut coax vs slack.

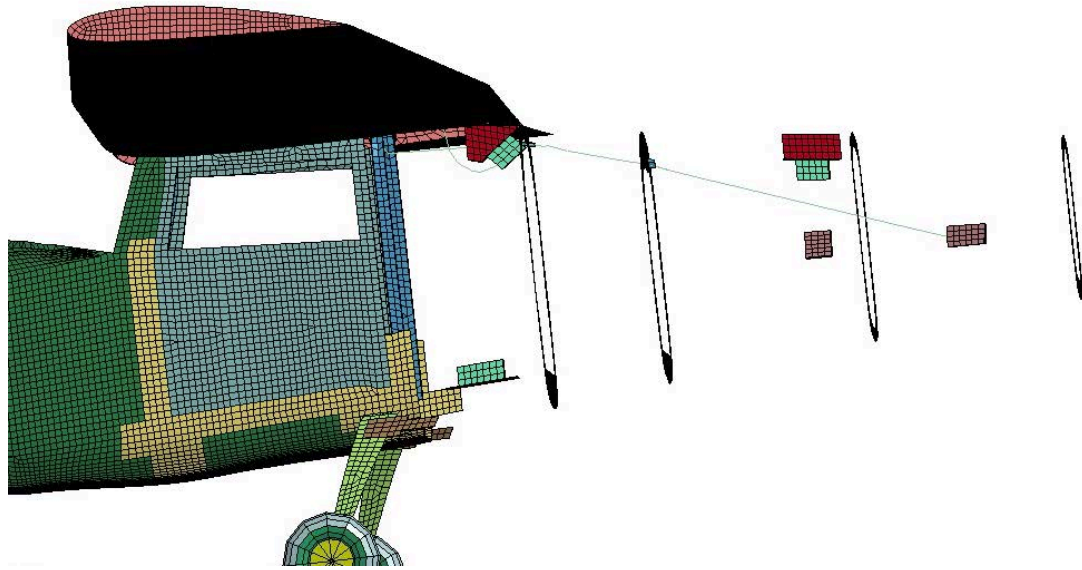


Figure A3. Test 2 with coaxial cables modeled between the ELT and antenna. Note the long cable that lies between the ELT in the rear tail and the antenna in the cockpit area is taut at time 0.021-s.

The only test scenario that produced forces, i.e., strains, sufficient to break the coaxial cable (or pull the cable from the connector) was Test 3 where the aluminum skin “unzips” along rivet lines behind the rear window, and the tail opens up and nearly separates from the rest of the fuselage. Thus, only Test 3 onto soil and various analysis scenarios based on Test 3 impact conditions, such as impact onto concrete, produced tail failure with large tensile forces capable of breaking the coaxial cable.

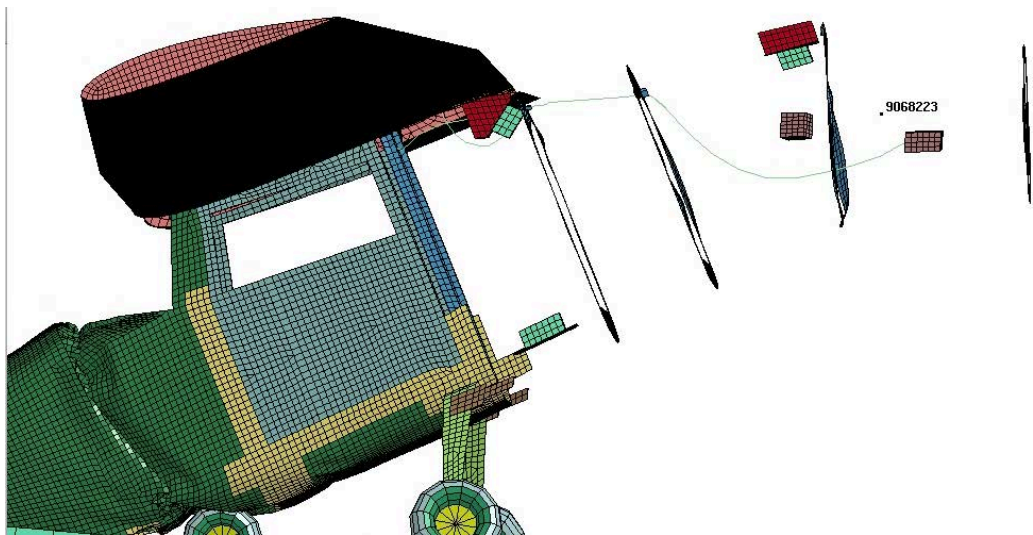
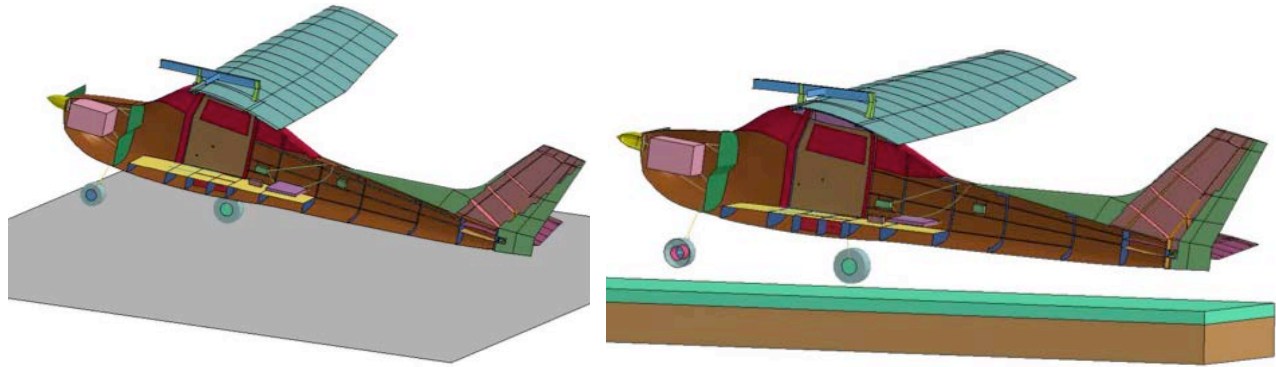


Figure A4. Test 2 showing the long cable going slack at time 0.156 seconds after the tail buckled.

To illustrate the influence of taut-versus-slack cables, two cases were executed representing Cases 7 and 8. As a reminder, Case 7 is the swept tail model representing Test 3 executed onto a rigid surface, and Case 8 is the Test 3 condition with the impact occurring onto layered soil. Pictures of the models for Cases 7 and 8, sliced in half, are shown in Figure A5 illustrating that two cables were included. One cable is taut and the other is slack. Both cables are attached to a sidewall mounted ELT on one end and to a point on the upper surface of the tail on the other.



(a) Case 7 half model.

(b) Case 8 half model.

Figure A5. Models of the swept tail aircraft with two cables (taut and slack) included.

Resultant axial forces in the cables are plotted in Figure A6 for Case 7. As can be seen, the taut cable exhibits a peak force of 55-lb and fails at 0.175-s. In contrast, the cable with 10-in. of slack exhibits oscillations and survives. Next, the Case 8 model was simulated onto layered soil with a taut cable and a 13-in. slack cable. Resultant axial forces are plotted in Figure A7 for Case 8. For this case, the taut cable exhibits a nearly identical load behavior as it does in Case 7. A peak load of 60-lb is achieved and the taut cable fails at 0.165-s. For Case 8, the cable with 13-in. of slack also fails, due to tail separation. The peak load is again 60-lb and failure occurs at 0.4-s. Thus, the addition of slackness in the cable provided an extra 0.2-s of time in this scenario, during which signals might be propagated.

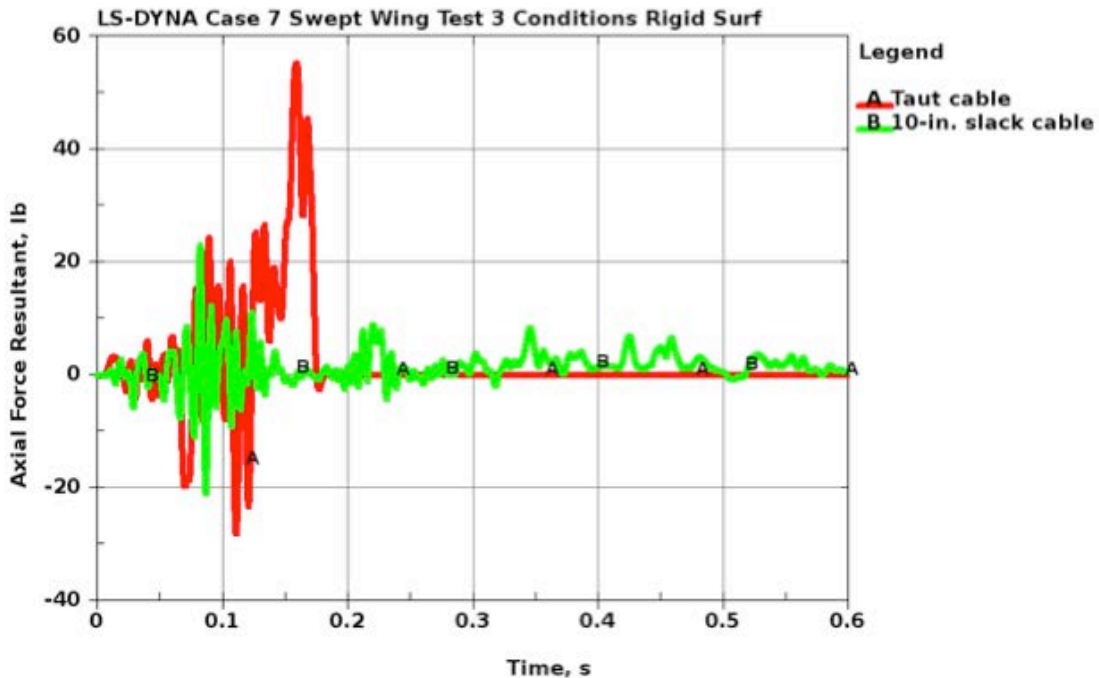


Figure A6. Resultant axial forces for taut and 10-in. slack cables for Case 7 onto a rigid surface.

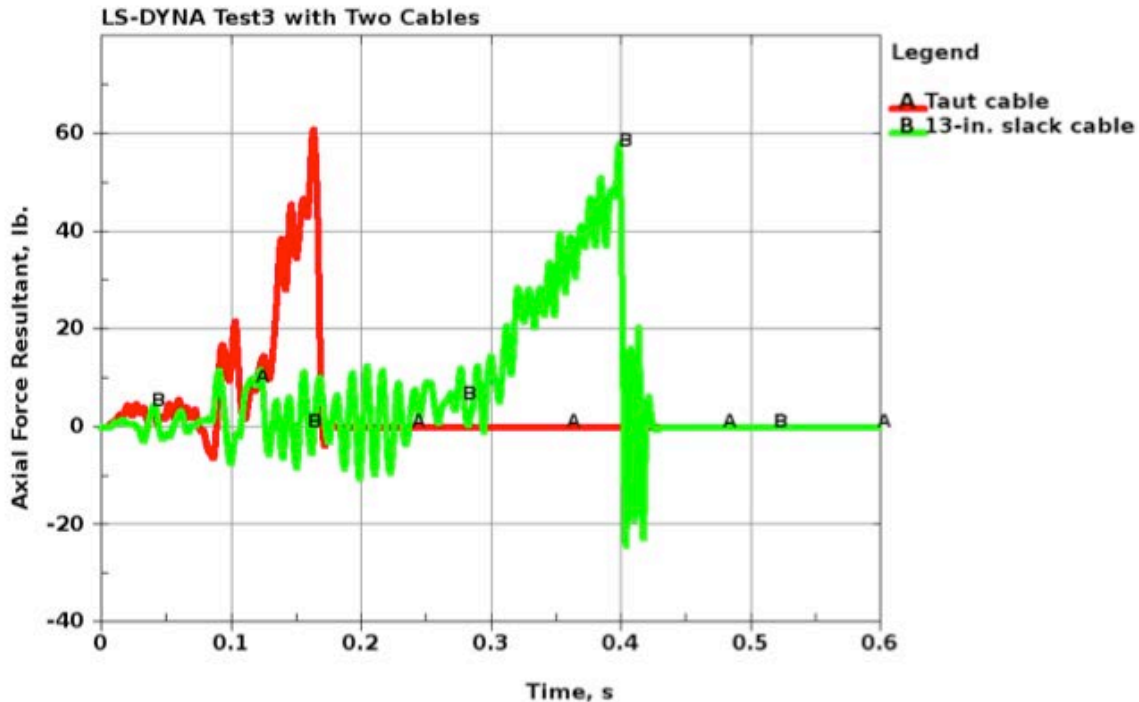


Figure A7. Resultant axial forces for taut and 13-in. slack cables for Case 8 onto soil.

A series of simulations were executed to determine the influence of pitch attitude. The Test 3 model (Case 8) was executed for three pitch angles: 6° , 8° , and 10° , as shown in Figure A8. Each model contained two cables, one taut and the other with 13-in. of slack. Resultant axial forces are plotted versus time for each simulation, as shown in Figures A9, A10, and A11. For the 6° pitch model, the taut cable failed, but the 13-in. slack cable did not. For the 8° pitch model, both cables failed with failure of the 13-in. slack cable occurring approximately 0.2-s later in time. However, with the 10° pitch model, the slack cable did not fail, but the taut cable did. Thus, findings from this study are: the taut cable failed in each simulation, whereas the slack cable did not fail at 6° and 10° pitch, but did fail at 8° pitch. Therefore, it can be stated that cable slackness will not always protect the ELTs and their connectors such that the dynamic forces and cable strain remain below the failure limit. However, it does show the benefit of including a reasonable amount of slack in that the probability of cable survival is increased.

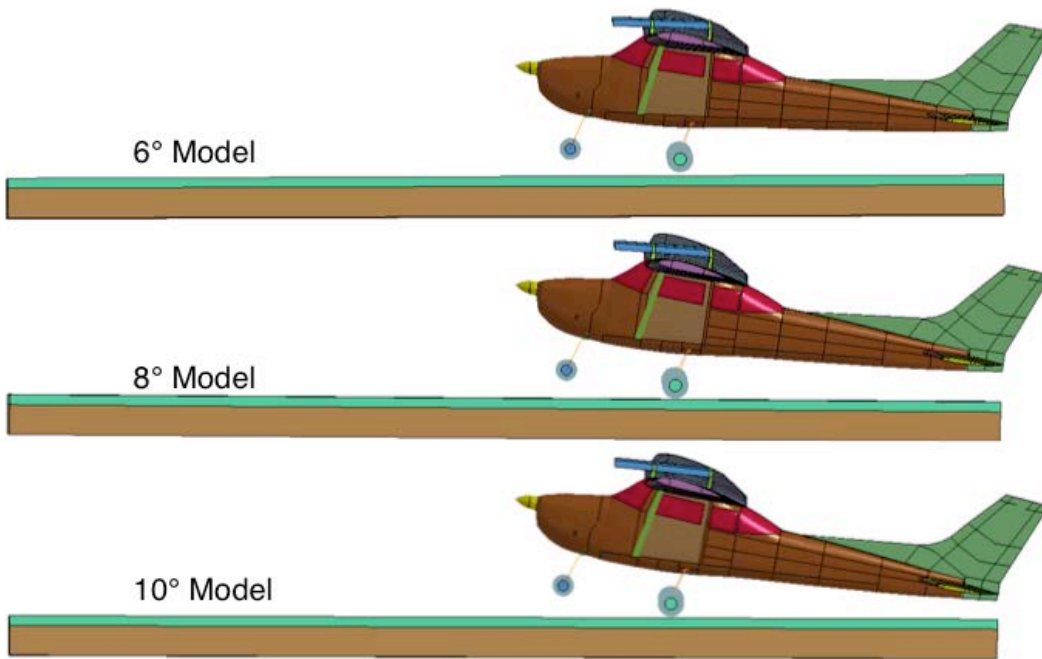


Figure A8. Influence of pitch angle using Case 8.

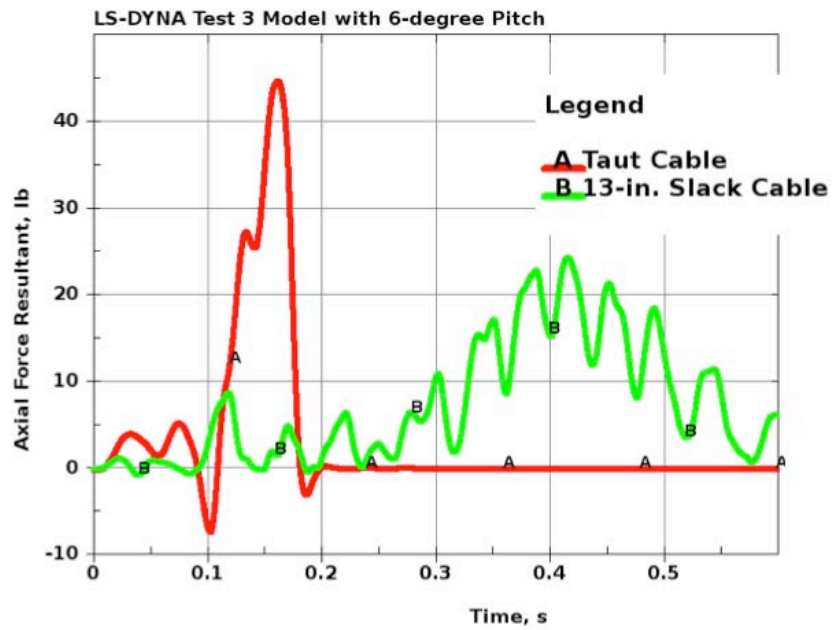


Figure A9. Resultant axial force versus time for the Case 8 model with 6° pitch.

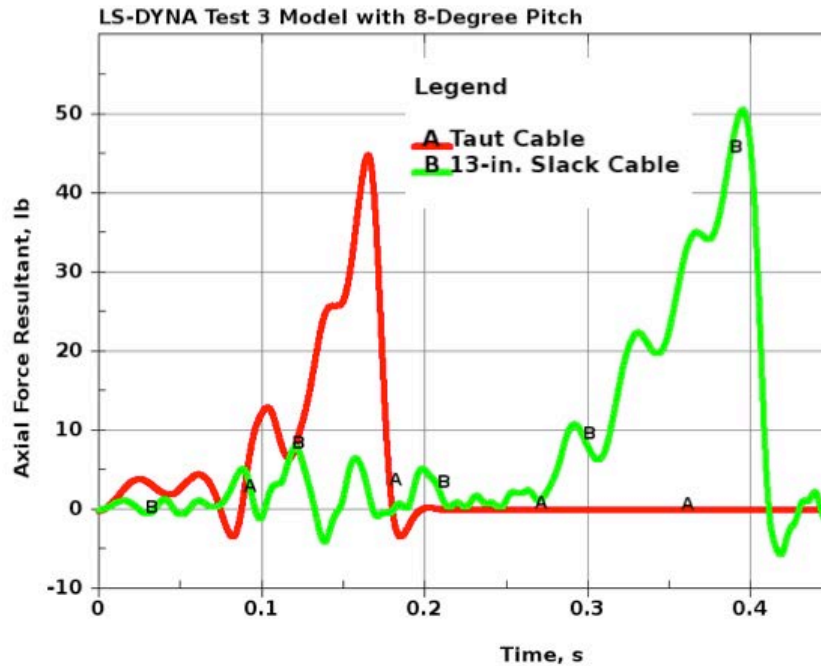


Figure A10. Resultant axial force versus time for the Case 8 model with 8° pitch.

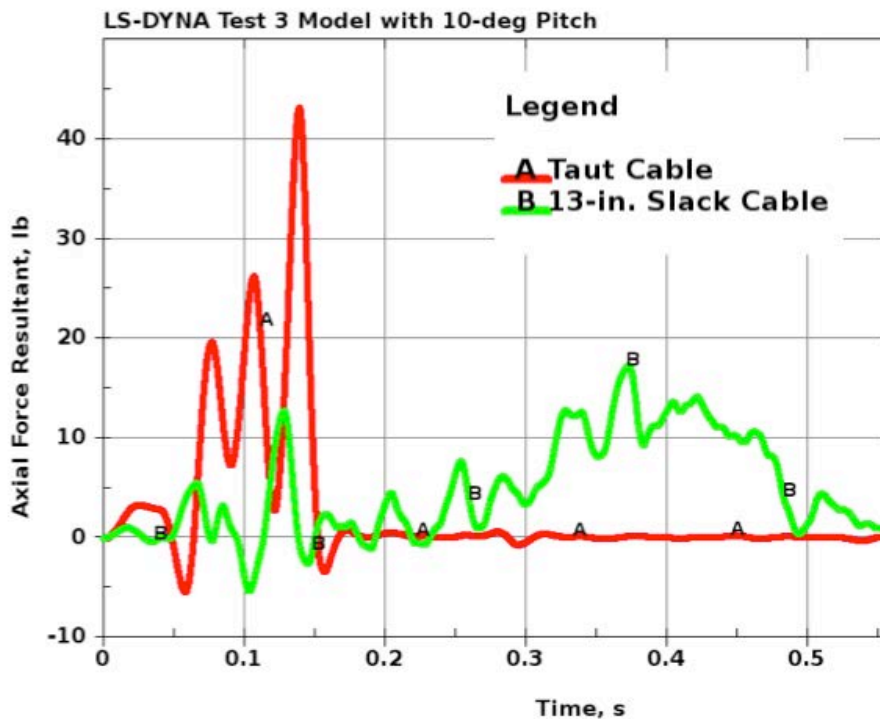


Figure A11. Resultant axial force versus time for the Case 8 model with 10° pitch.

For comparison purposes only, the measured axial force in Dummy cable 1 from Test 2 is plotted in Figure A12. The force response, which is quite “noisy” is similar in appearance to the responses predicted by the models in Figures A9, A10 and A11, though the magnitude of the test response is lower (15-lb compared with 42-lb). It should be noted that the dummy cable did not fail during the test [4].

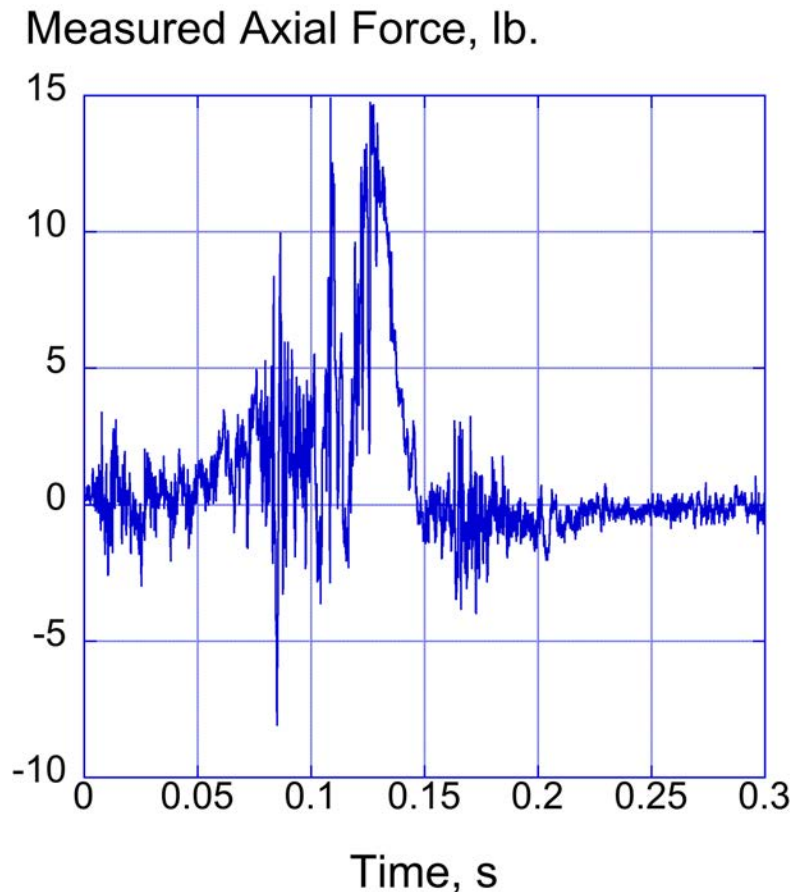


Figure A12. Plot of measured axial force versus time of the Dummy Cable 1 in Test 2.

Prior to discussing the results of Analysis Case simulations, it is useful to understand the regulatory guidance regarding installation of ELTs in GA aircraft. DO-204A [17] requires “some slack” in antenna cable installation, but no quantifiable amount or minimum value is provided for guidance. FAA AC 43.12-1b [Reference A2] suggests a minimum bend radius of no less than 6x the outer diameter of the coaxial cables onboard the aircraft. For a 0.25-in.-outer-diameter coaxial cable, the bend radius equates to 9.4-in. of cable dedicated to create a complete strain relief loop. Instead of modeling the cable loop explicitly, 10- or 13-in. of slack was added to the cable length in the model.

Analysis Matrix of Crash Scenarios

Following the model calibration effort described in the main body of the report, the ELTSAR management team requested that several analysis cases be executed to evaluate varying impact velocities and impact surfaces. Using the models developed for the straight tail C-172 (Test 1 and Test 2) and swept tail C-172 (Test 3), a series of simulations were performed, as shown in Table A1. Note that Case 1 is the Test 1 condition, Case 6 represents Test 2, and Case 8 represents Test 3. These three cases have been addressed in the main report and will not be repeated in this Appendix. The remaining cases are pure simulations without any test data to support the results. As with any simulation, care must be taken when the input conditions are outside the range that has been compared with test. Thus, the high velocity cases at cruise (2400 in/s) may or may not be valid and the results should be viewed with caution. Summary results of each analysis matrix simulation will be presented in subsequent sections of the appendix.

Table A1. Proposed analysis cases following model calibration.

Case	Pitch	V _x , in/s	V _z , in/s	V _R , in/s	Surface	Airframe
1*	+1.5°	720	276	771	Rigid	Straight tail
2	+1.5°	720	276	771	Layered soil	Straight tail
3	+1.5°	2400	312	2424	Rigid	Straight tail
4	+1.5°	2400	312	2424	Layered soil	Straight tail
5	-12.2°	823.2	344.4	892.3	Rigid	Straight tail
6 [§]	-12.2°	823.2	344.4	892.3	Layered soil	Straight tail
7	+8.0°	682.8	283.2	739.2	Rigid	Swept tail
8 [#]	+8.0°	682.8	283.2	739.2	Layered soil	Swept tail
9	+8.0°	2400	312	2424	Rigid	Swept tail
10	+8.0°	2400	312	2424	Layered soil	Swept tail

*Case 1 represents Test 1, §Case 6 represents Test 2, and #Case 8 represents Test 3

Case 2: Test 1 Impact Conditions onto Soil

The Case 2 simulation is of the straight tail Cessna 172 Test 1 scenario with the rigid impact surface replaced with soil, as shown in Figure A13. The LS-DYNA airplane model for Test 2 was used for this simulation as the Test 2 model has a propeller and spinner, which are needed to simulate soil impact. When the impact occurred on the rigid surface, the “crash” was a very survivable hard landing with only minor damage. However, a landing onto soft soil is very different. First, the main landing gear digs into the soil, which produces a pitching moment, and shortly afterwards the nose gear slaps down into the soil and fails like the Test 2 condition (Case 6). Although the forward and vertical velocities are less than the Test 2 condition, the airplane still behaves similar to Test 2 and flips over landing upside down. However, the tail does not buckle for this case due to the lower velocity.

A plot of vertical acceleration time history from the mid-cabin floor is shown in Figure A14 for Case 2. This plot indicates that the floor vertical acceleration, except for a peak of 12 g’s, is relatively low in magnitude with an average acceleration of about 5-g and has a pulse duration of approximately 0.25-s. Note that the average vertical floor-level accelerations for Test 1 were approximately 4-g.

In contrast to Test 1, the forward accelerations for the impact into soft soil are much higher. For Test 1, the forward accelerations were low in magnitude. However, for the impact into soil the forward acceleration response, shown in Figure A15, has a peak of 15 g’s and produces an overturning moment that causes the plane to land upside down (see Figure A16).

Case 3: Test 1 Straight Tail Aircraft Impacting at Cruise Velocity onto Rigid Surface

This simulation used the Test 1 straight tail aircraft model with the pitch unchanged at +1.5 degrees, but with the forward velocity increased from stall to cruise speed. The sink velocity was increased approximately 13% from 276 in/s to 312 in/s. The model for Case 3 is depicted in Figure A17.

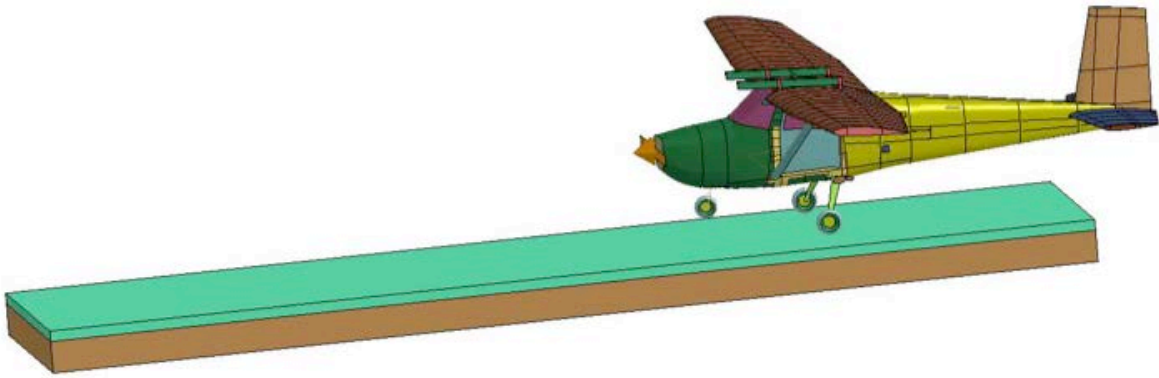


Figure A13. Case 2 simulation representing Test 1 crash impact onto soil.

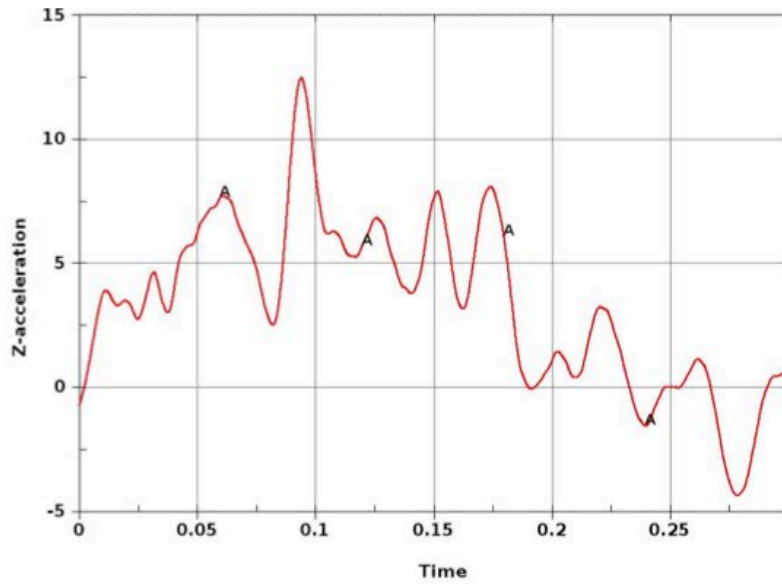


Figure A14. Vertical acceleration on the outer seat track, mid-cabin, right side for Case 2.

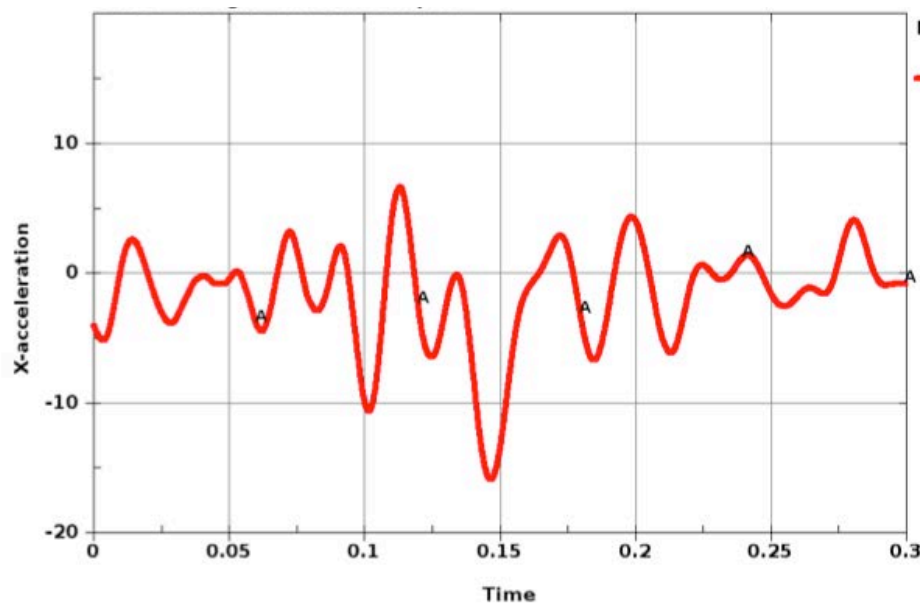


Figure A15. Forward acceleration on the outer seat track, mid-cabin, right side for Case 2.

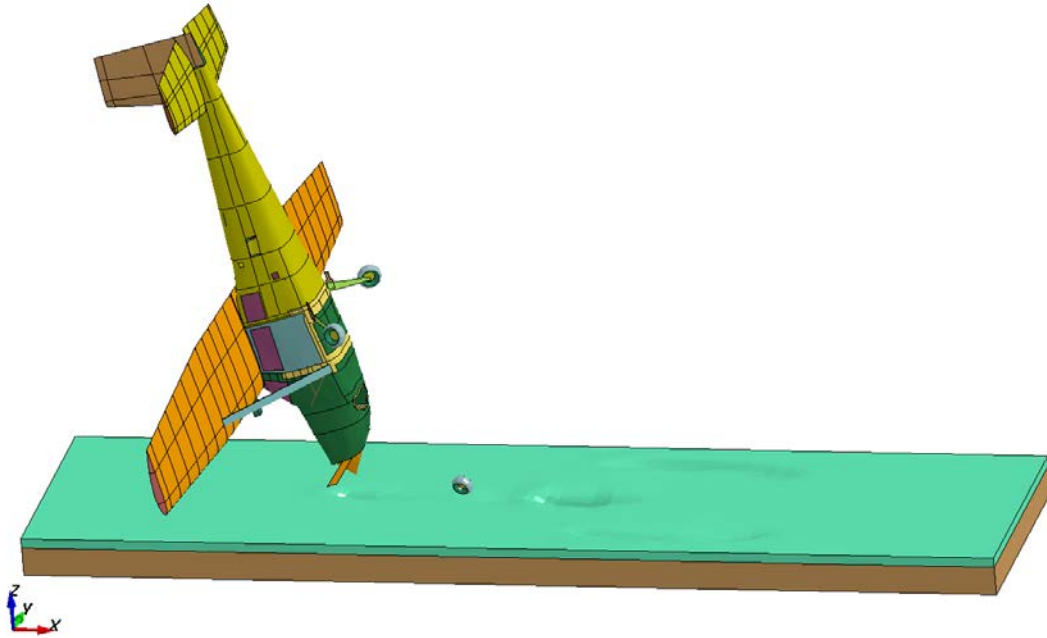


Figure A16. Aircraft starting roll over onto its back.



Figure A17. Case 3 model, straight tail aircraft impacting rigid surface at cruise velocity.

Plots of the vertical and forward accelerations of the outer seat track at the mid-cabin level are shown in Figures A18 and A19, respectively, for Case 3. Once again, the vertical acceleration response oscillates about 5-g, until about 0.1-s, at which time the floor experiences an impact causing the acceleration to peak at 22.5-g at 0.145-s due to failure of the nose gear and contact of the bottom of the plane with the concrete as can be seen in Figure A20. But, unlike Test 1, the forward acceleration is much higher due to bottom contact with the concrete at 0.145 seconds. The friction coefficient of 0.8 produces a corresponding forward acceleration of about 15 g's. The model was executed to 0.7 seconds. The plane slides on the cowling and the tail rotates upward by about 10 to 15 degrees, but by 0.7 seconds the plane was more or less stable and did not flip over.

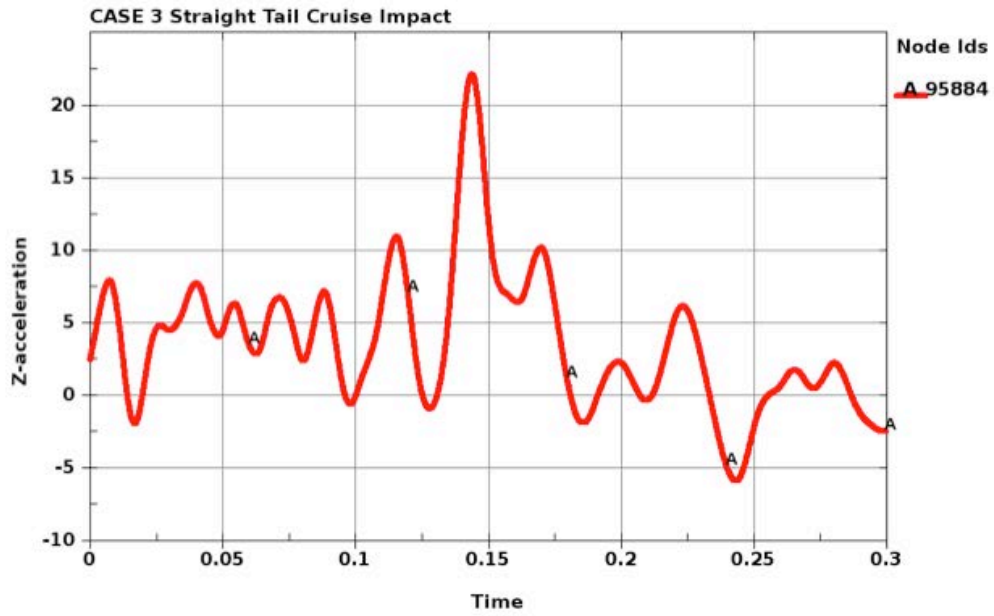


Figure A18. Vertical acceleration response of the mid-cabin floor for Case 3.

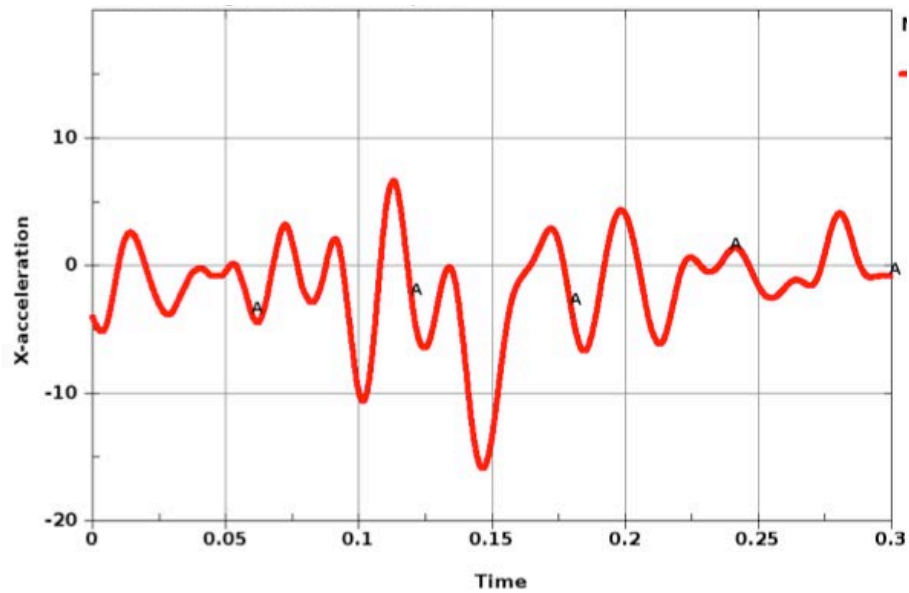


Figure A19. Forward acceleration of the mid-cabin floor for Case 3.

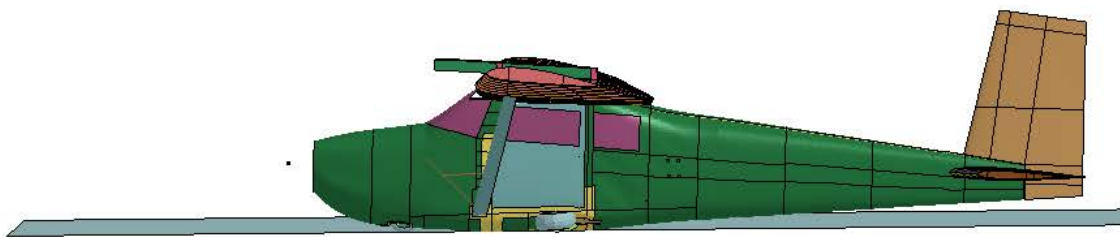


Figure A20. Model deformation at a time of 0.145-s after impact, maximum contact, maximum acceleration.

Case 4: Straight Tail at Cruise Velocity onto Soil

For this simulation, the Case 2 model was used with the velocity magnitudes increased to the cruise condition of 2400-in/s in the forward direction and a sink velocity of 312 in/s. Hence, refer to Figure A13 for the initial orientation of the aircraft. A picture of the model is shown in Figure A21. Due to the high forward velocity, the soil impact surface was lengthened. This impact is catastrophic. A fringe plot of vertical soil deformation is shown in Figure A22. Maximum displacement of the nose gear tire into the soil is 8.64-in. Finally, a picture showing model deformation at 0.3-s is shown in Figure A23. The tail has buckled and the aircraft has lost the nose and main gear tires and is close to flipping upside down. Due to massive deformations, the soil model began to lose integrity shortly after 0.3 seconds and the simulation was terminated. Peak accelerations filtered at 20 Hz were noted to be over 30 g's in the forward direction.

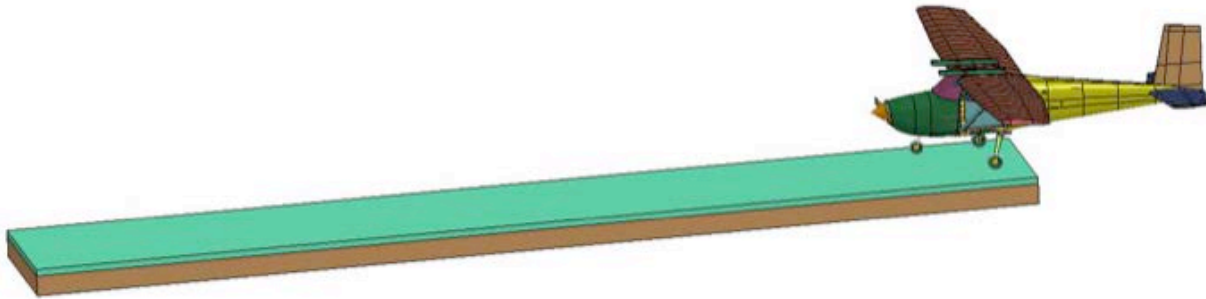


Figure A21. Model representing Case 4.

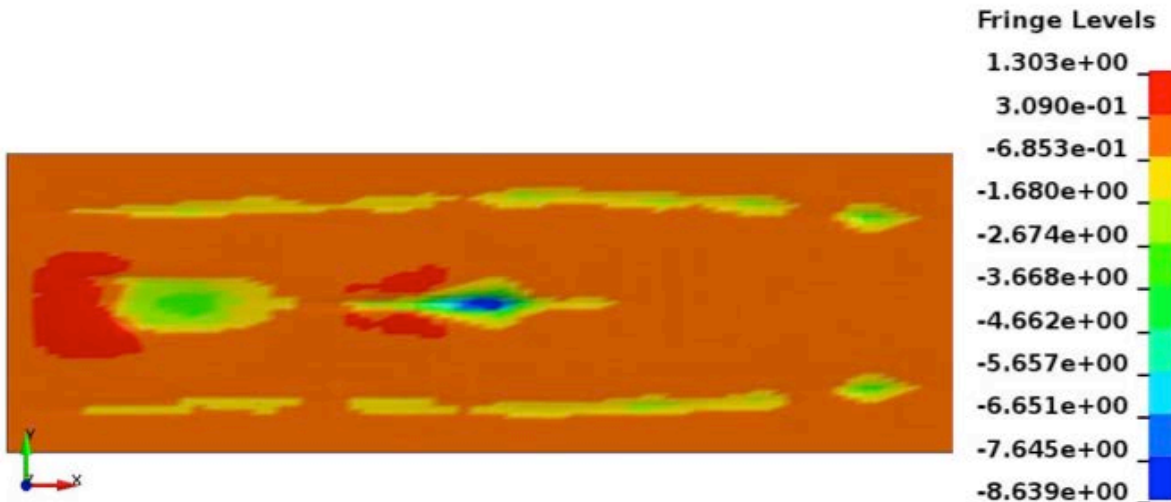


Figure A22. Soil deformation pattern for Case 4.

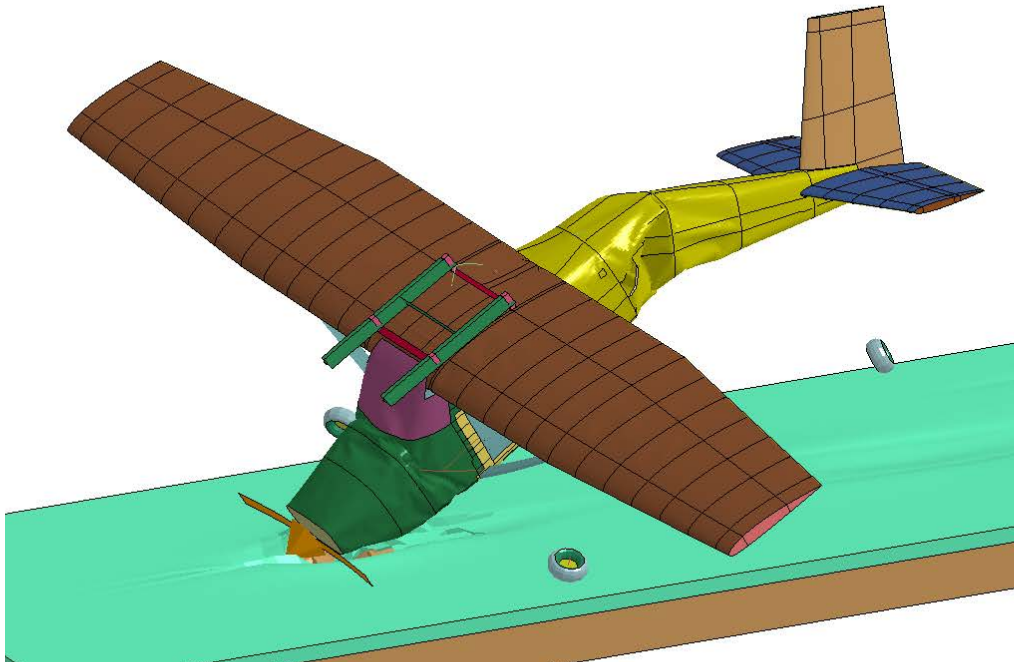


Figure A23. Case 4 model at 0.3-s.

Case 5: Straight Tail Test 2 Condition onto Rigid Surface

Case 5 represents the Test 2 condition with the layered soil replaced with a rigid surface. Note that, unlike Test 1 with the nose pitched up as in a landing, this flight path angle is a 12.2° nose down condition and at a higher forward and vertical velocity than Test 1. Even though the soft soil has been removed, a bad outcome is still expected for this impact condition. The model at impact with the rigid surface for Case 5 is shown in Figure A24. Note that the friction coefficient for contact between the aircraft and the concrete surface was assumed to be 0.8. By 0.2 seconds, the nose gear had failed, the cowling was dragging on the surface, and the maximum buckle of the tail for this case had formed as is shown in Figure A25. Finally, as can be seen in Figure A26, by 1.2 second the aircraft is about to flip over. The vertical acceleration of the impact reached 22 g's at 0.07 seconds as can be seen in Figure A27. From observing the trace in Figure A28, the forward acceleration pulse is also quite high reaching a peak of over 20 g's by 0.1 seconds.

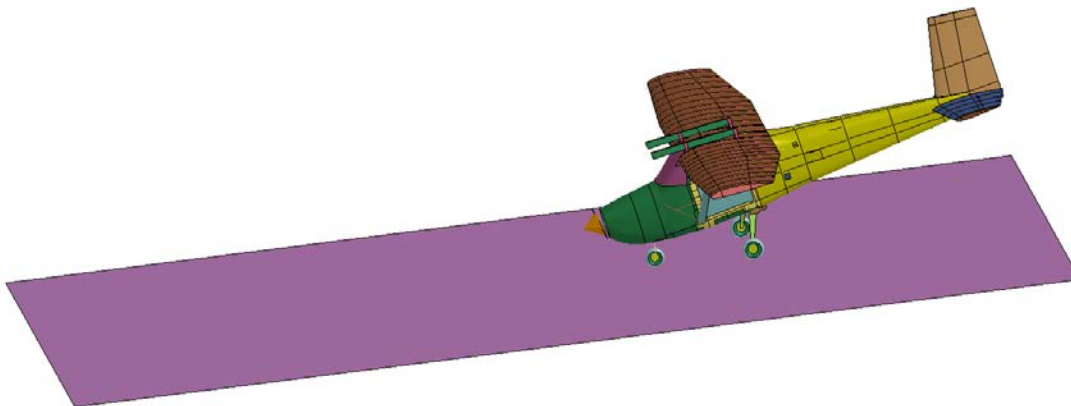


Figure A24. Case 5 model representing the Test 2 condition onto a rigid surface.

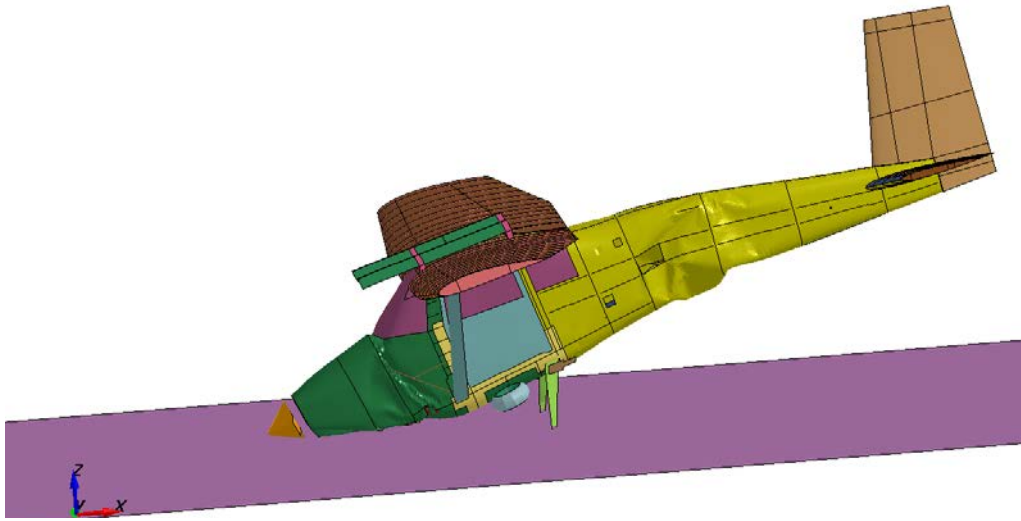


Figure A25. Buckle in tail and wheel axel failure occurring at approximately 0.2 seconds.

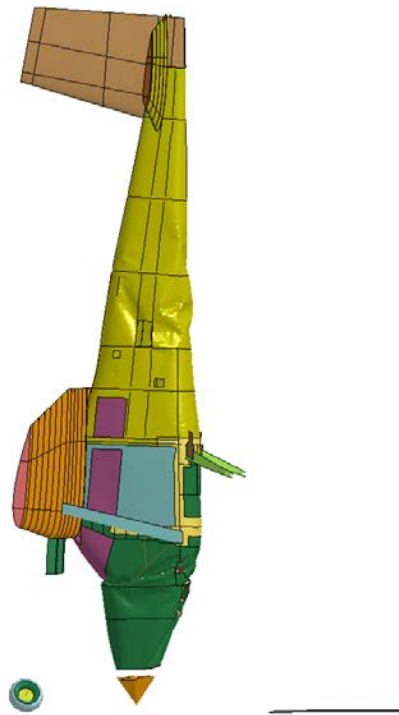


Figure A26. Aircraft about to flip over at approximately 1.2-seconds after impact.

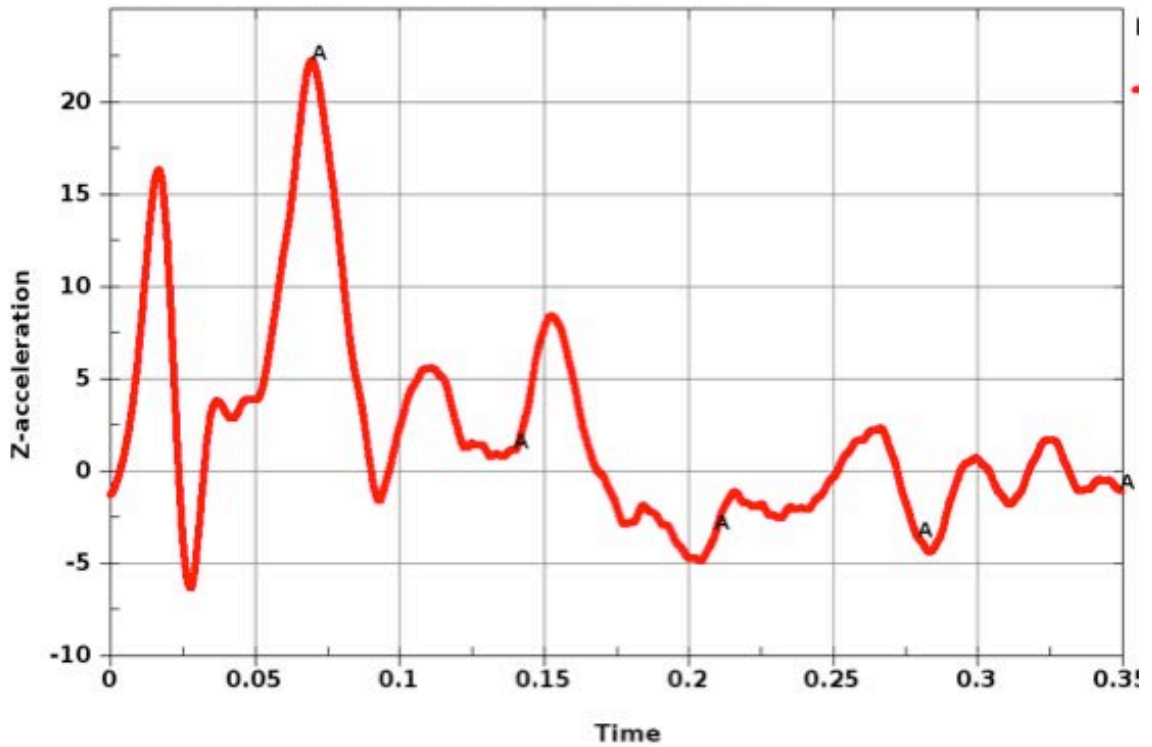


Figure A27. Vertical acceleration response of the mid-cabin floor for Case 5.

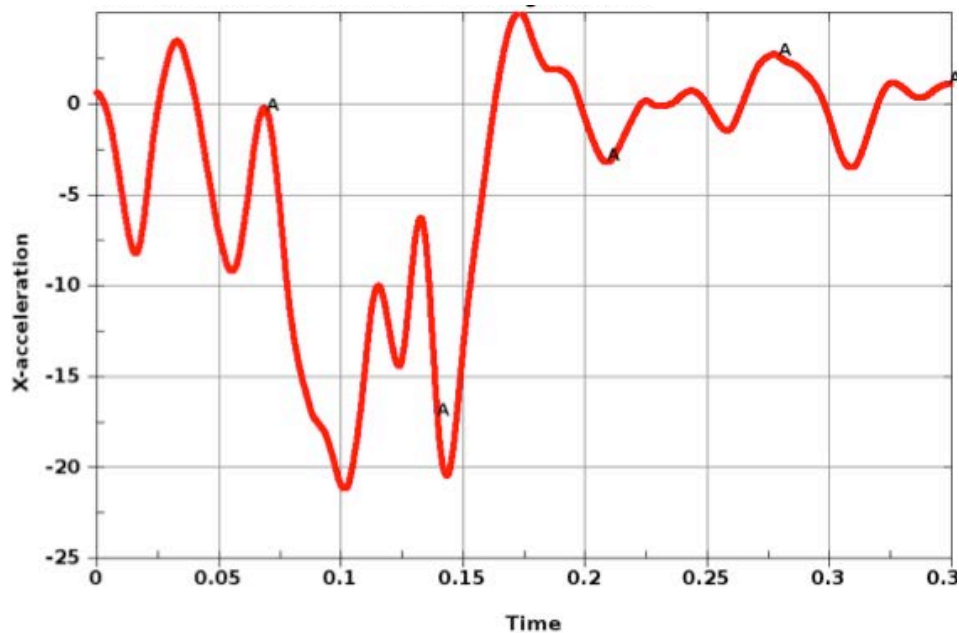


Figure A28. Forward acceleration of the mid-cabin floor for Case 5.

Case 7: Swept Wing Model onto Rigid Surface at Stall Speed

Figure A29 shows the swept wing model (Test 3) making initial contact onto a rigid surface at the same velocity and attitude as crash Test 2. At a time of 0.3 seconds, the nose gear has stroked fully, the engine compartment has deformed after contact with the rigid surface, and the failure behind the rear window is evident in Figure A30. By 0.6 seconds after impact, the aircraft has rotated to

approximately 20 degrees as depicted in Figure A31. Forward and vertical accelerations for this condition are shown in Figures A32 and A33, respectively. The maximum forward acceleration peak is 10 g's while the maximum vertical acceleration is 25 g's. These accelerations could lead to injuries for the occupants, but would likely be survivable.

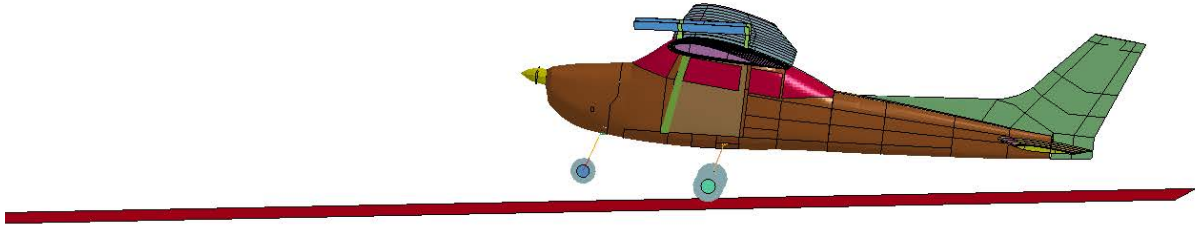


Figure A29. Case 7 Model in impact condition.

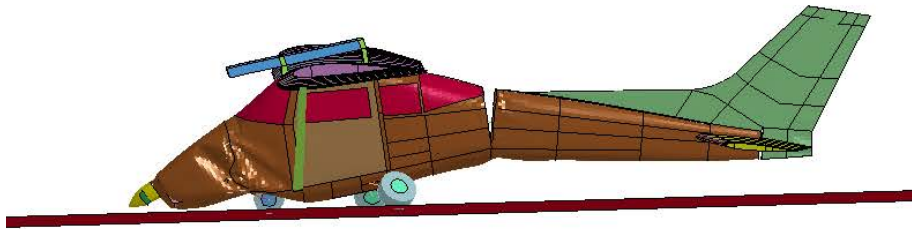


Figure A30. Swept wing model 0.3 seconds after impact.

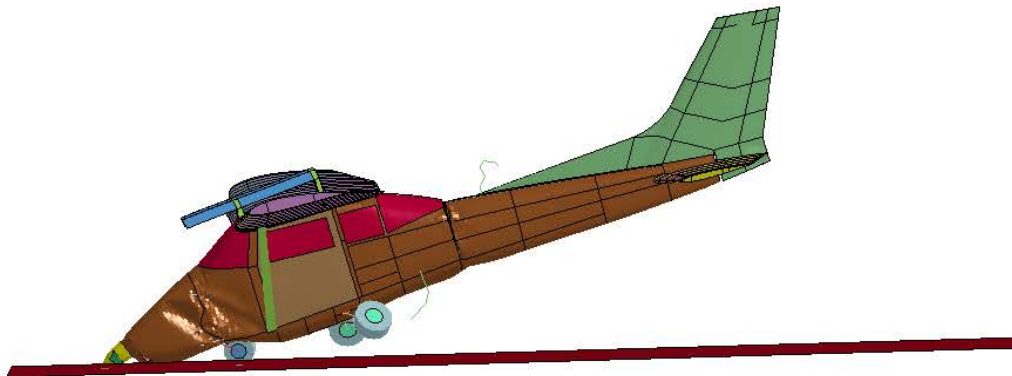


Figure A31. Swept wing model 0.6 seconds after impact.

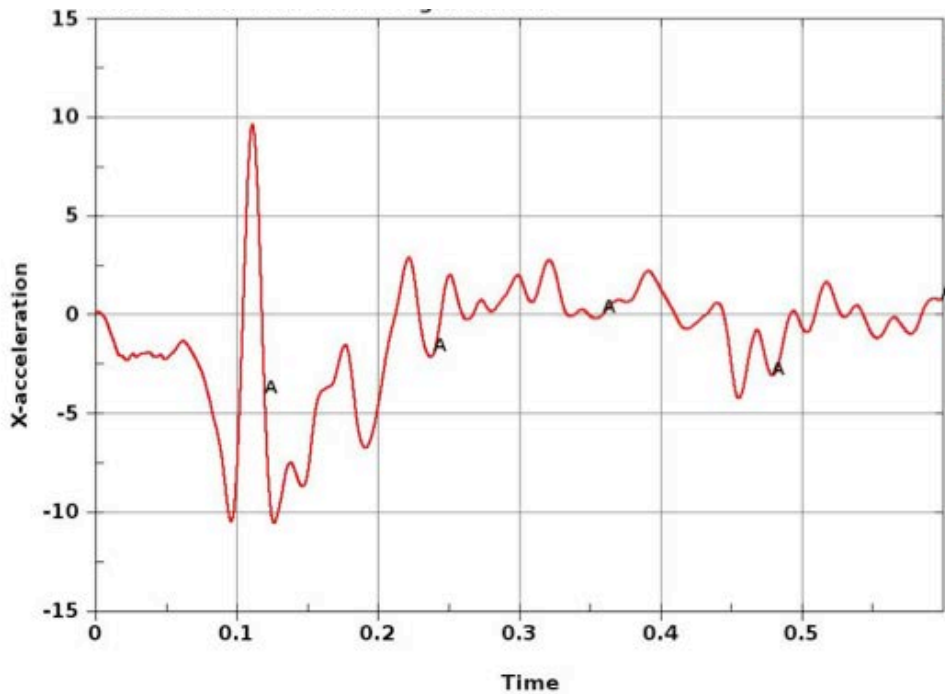


Figure A32. Forward acceleration of the mid-cabin floor for Case 7.

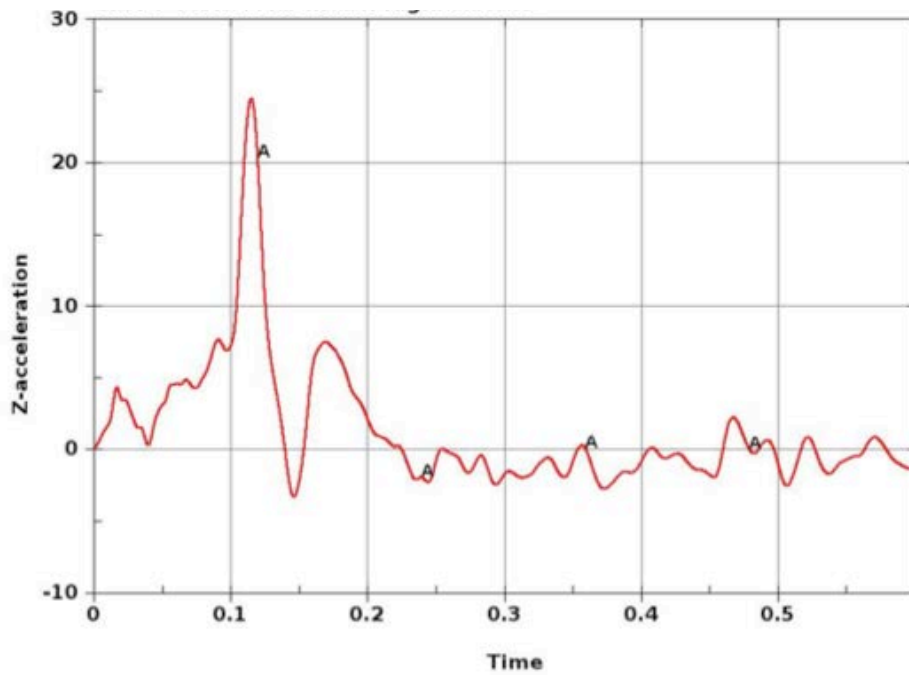


Figure A33. Vertical acceleration of the mid-cabin floor for Case 7.

Case 9: Swept Wing Model at Cruise Speed Impacting onto a Rigid Surface

The attitude of the aircraft model and surface (rigid) at impact (Figure A34) is the same as Case 7. However, the airplane is impacting the rigid surface at cruise speed. The tail breaks behind the window and by 0.3 seconds the aircraft is starting to rotate as is seen in Figure A35. By 0.6 seconds after impact, the aircraft has rotated to an angle of approximately 45 degrees (Figure A36). The forward acceleration peaked at 25 g's near 0.1 seconds (Figure A37), while the vertical acceleration

was even higher at approximately 32 g's (Figure A38). This crash scenario is potentially survivable, but injuries are highly likely.

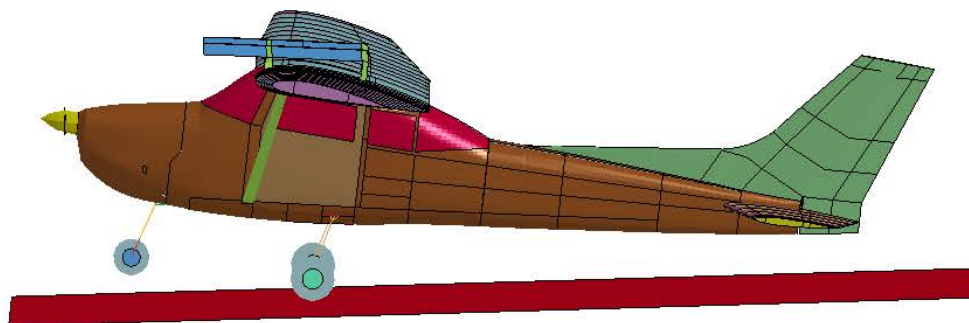


Figure A34. Initial attitude for swept wing model at cruise speed onto rigid surface.

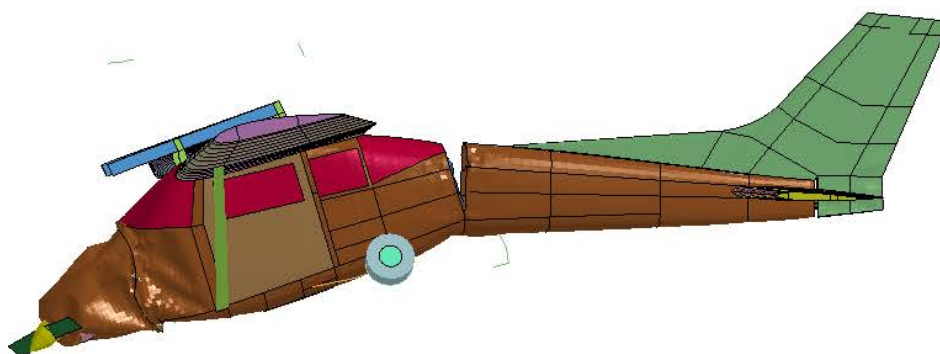


Figure A35. Swept wing at cruise impacting onto a rigid surface at 0.3 seconds after impact.

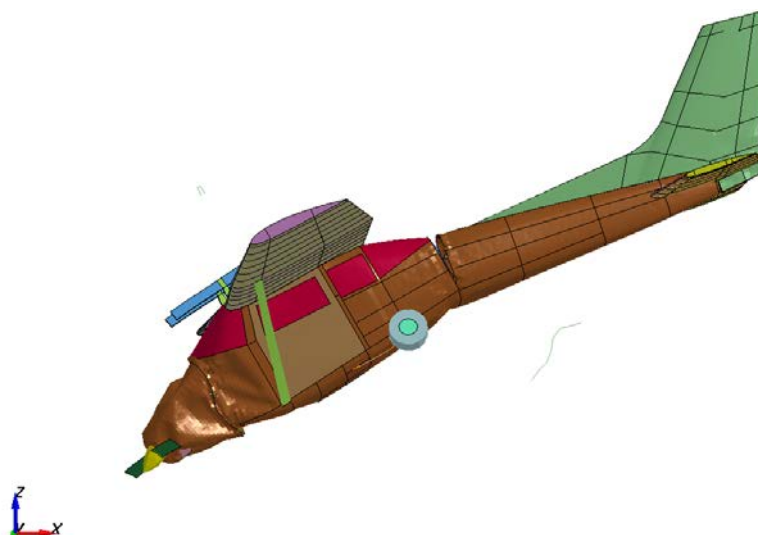


Figure A36. Swept wing at cruise impacting onto rigid surface at 0.6 seconds after impact.

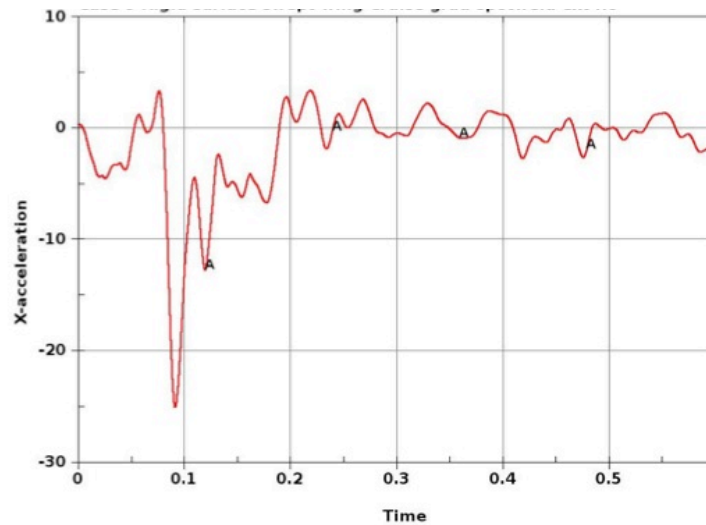


Figure A37. Forward acceleration of the mid-cabin floor for Case 9.

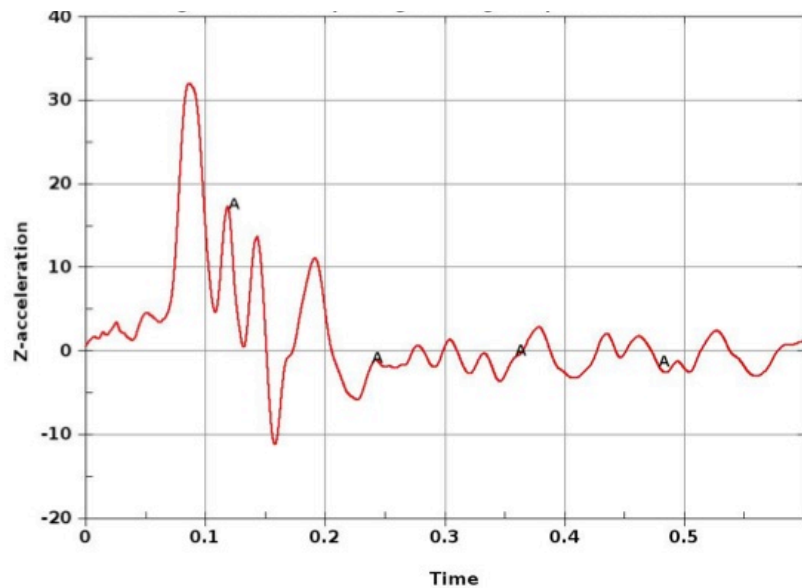


Figure A38. Vertical acceleration of the mid-cabin floor for Case 9.

Case 10: Swept Wing Model onto Layered Soil Surface at Cruise Speed

This case of the swept wing model onto soft soil at cruise speed (Figure A39) is another catastrophic crash simulation that must be viewed with caution. In addition to the tail failure behind the rear window, the engine compartment is severely damaged early in the simulation. In the picture shown in Figure A40, by 0.36 seconds after impact, the engine has broken loose and the entire engine compartment has disintegrated. Before the end of the simulation, the soil model becomes unstable and the simulation must be stopped. The acceleration pulse in both the vertical and forward directions is short in duration and high in magnitude. In Figure A41, the forward peak acceleration is over 30 g's at a time of 0.11 seconds, while in Figure A42 the vertical acceleration reaches almost 40 g's at the same time. Any occupants in this crash would likely have received serious injuries, if they survived at all due to cabin encroachment of the engine compartment into the livable volume required for survival.

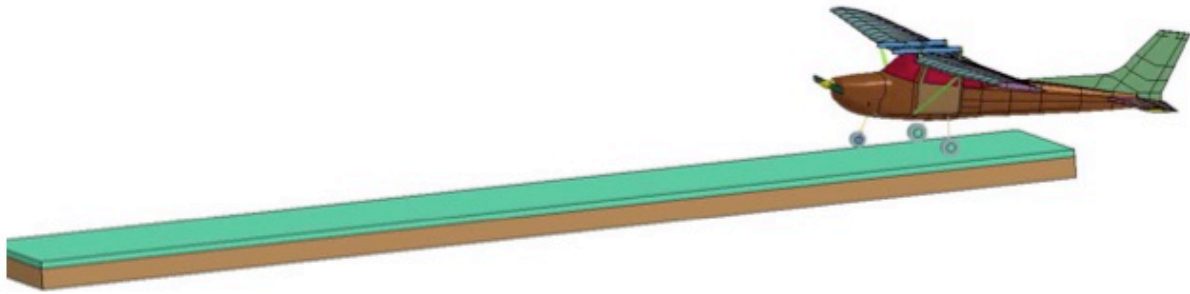


Figure A39. Initial attitude for swept wing model at cruise speed onto layered soil.

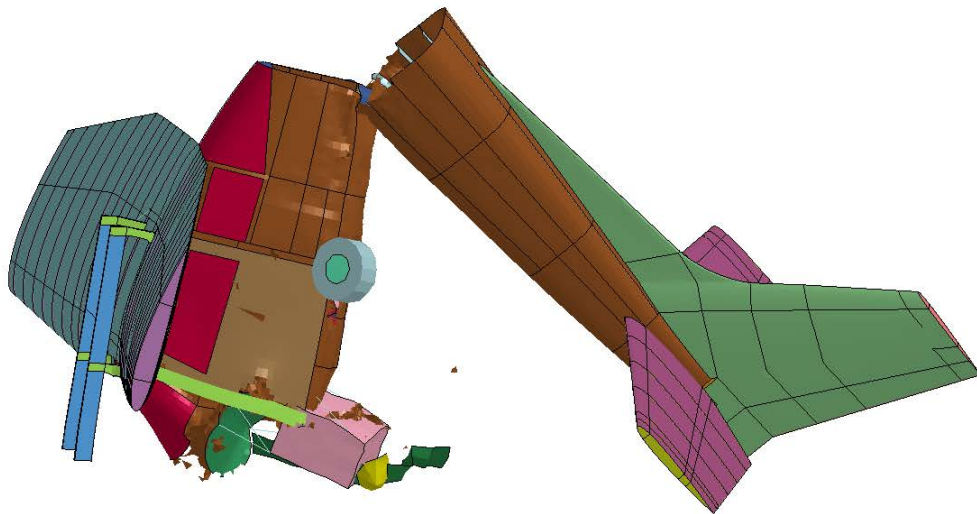


Figure A40: Deformation of swept wing aircraft at approximately 0.36 seconds after impact.

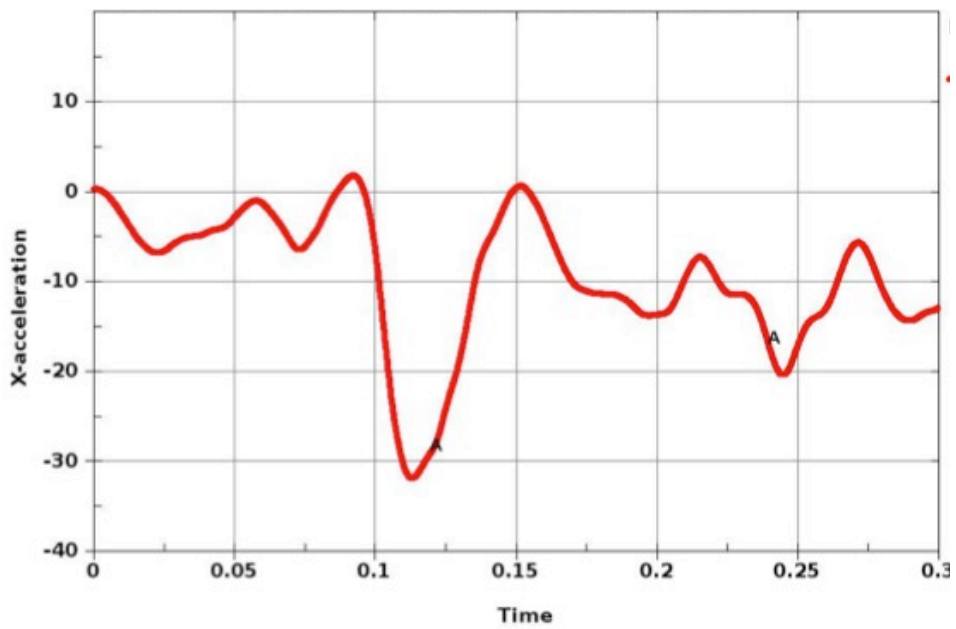


Figure A41. Forward acceleration of the mid-cabin floor for Case 10.

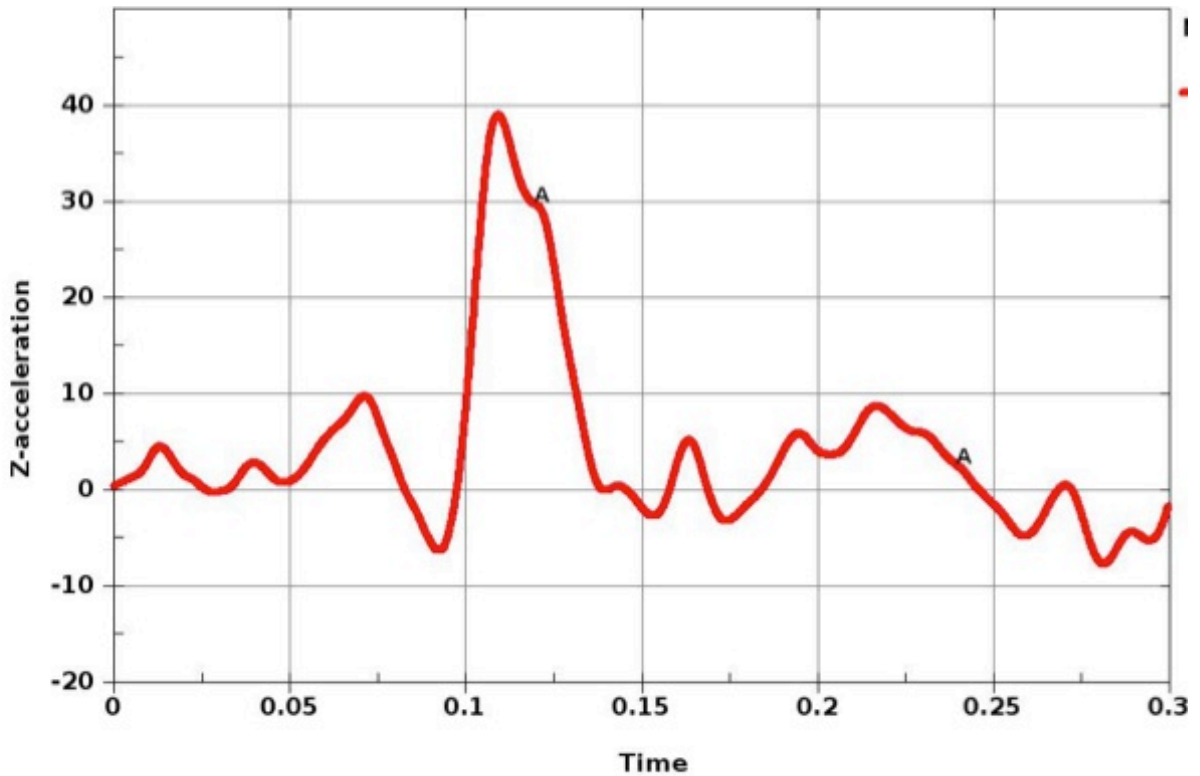
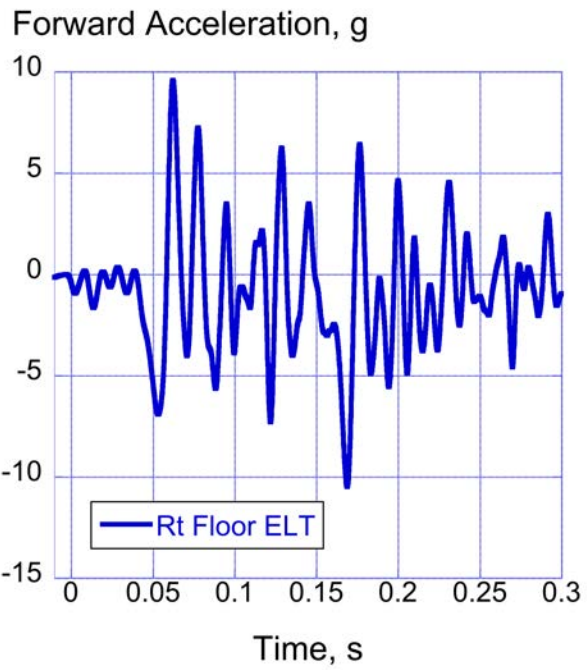


Figure A42. Vertical acceleration of the mid-cabin floor for Case 10.

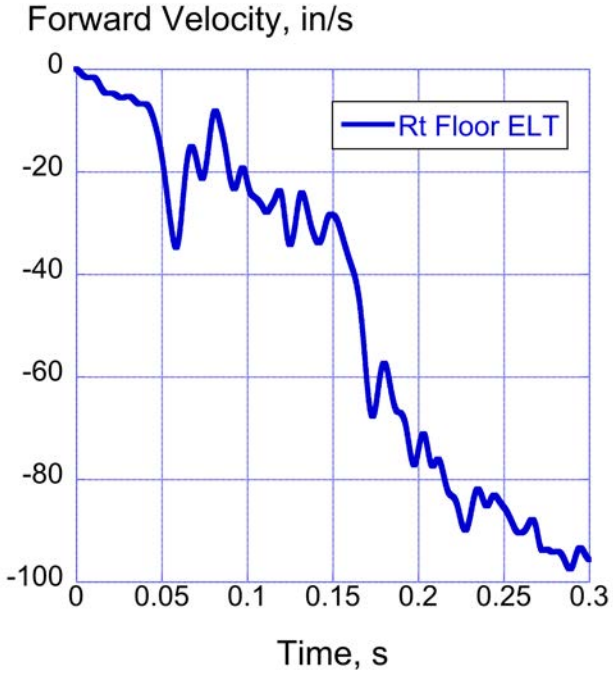
ELT Activation

As mentioned in the main body of the paper, forward acceleration and velocity responses measured for Test 1 were low in magnitude. As an example, the CFC20-filtered acceleration response of the right side floor-mounted ELT is shown in Figure A43(a) and the integrated velocity response is shown in Figure A43(b). The acceleration curve contains many oscillations, even after filtering. However, the overall magnitude is low.

The values of velocity at discrete time intervals of 0.05-s were obtained from the plot of Figure A43(b). The velocity data were used to determine an average acceleration at each of the discrete time values. The average acceleration is plotted in Figure A44. As can be seen, the average acceleration values are low, less than 1-g at each time step. This data is useful given the ELT activation chart, shown in Figure A45. The chart shows a 2-g activation threshold, which this accelerometer did not exceed, based on average acceleration values. However, as a reminder, forward accelerations for Test 1 experienced a sharp spike when the aircraft hit the restraining net, likely causing ELT activation at that time. Also, ELT acceleration responses for Test 2 and Test 3 were well within the activation range, according to Figure 45. Additional information regarding ELT activation rates during Tests 1-3 may be found in Reference 4.



(a) Forward acceleration.



(b) Forward velocity.

Figure A43. Forward acceleration and velocity responses of the right floor ELT during Test 1.

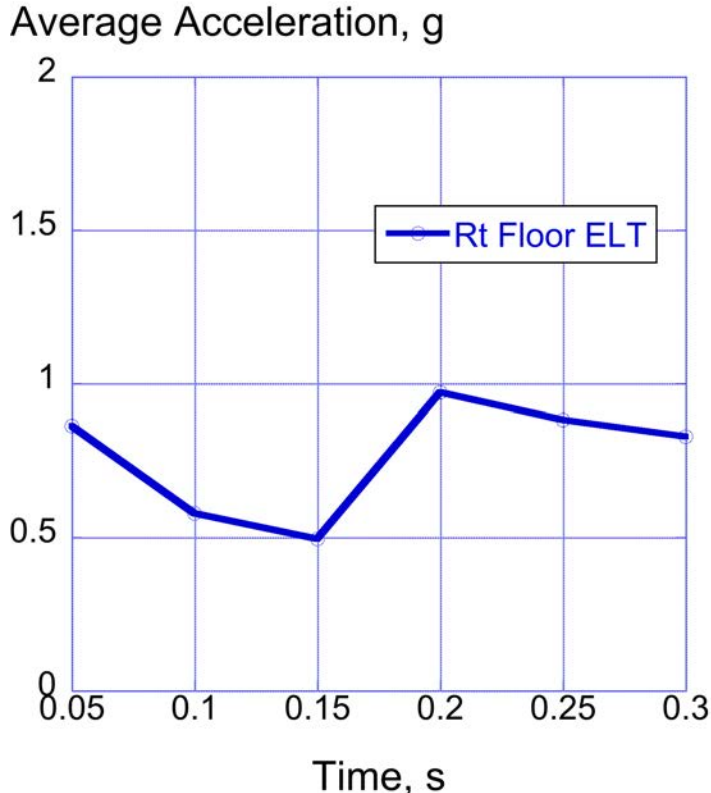


Figure A44. Plot of discrete average acceleration for the right floor ELT in Test 1.

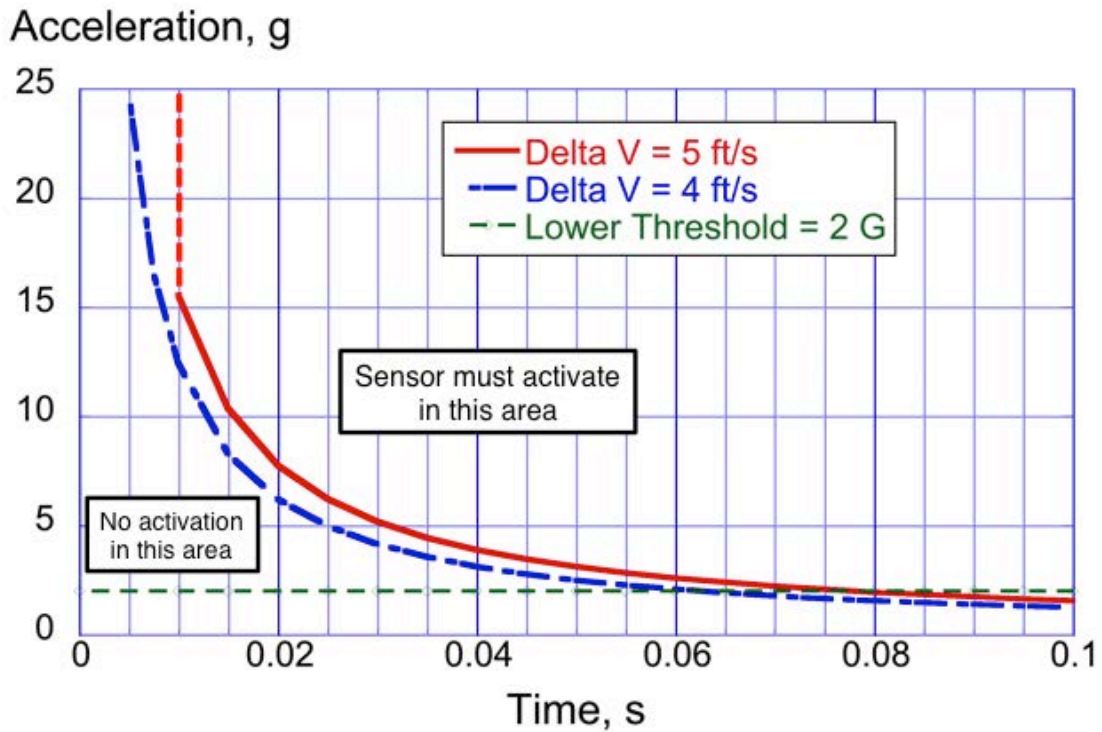


Figure A45. ELT acceleration threshold chart for activation.

Appendix References

- A1. Amphenol catalog W1, Radio Frequency Coaxial Cables and Transmission Lines, American Phenolic Corporation, Chicago 50, Illinois.
- A2. Federal Aviation Administration (FAA) Advisory Circular (AC) FAA AC 43.12-1b Acceptable Methods, Techniques, and Practices - Aircraft Inspection and Repair, September 8, 2008.

REPORT DOCUMENTATION PAGE

Form Approved
OMB No. 0704-0188

The public reporting burden for this collection of information is estimated to average 1 hour per response, including the time for reviewing instructions, searching existing data sources, gathering and maintaining the data needed, and completing and reviewing the collection of information. Send comments regarding this burden estimate or any other aspect of this collection of information, including suggestions for reducing the burden, to Department of Defense, Washington Headquarters Services, Directorate for Information Operations and Reports (0704-0188), 1215 Jefferson Davis Highway, Suite 1204, Arlington, VA 22202-4302. Respondents should be aware that notwithstanding any other provision of law, no person shall be subject to any penalty for failing to comply with a collection of information if it does not display a currently valid OMB control number.
PLEASE DO NOT RETURN YOUR FORM TO THE ABOVE ADDRESS.

1. REPORT DATE (DD-MM-YYYY) 01-07-2017		2. REPORT TYPE Technical Memorandum		3. DATES COVERED (From - To)	
4. TITLE AND SUBTITLE Simulating the Impact Response of Three Full-Scale Crash Tests of Cessna 172 Aircraft				5a. CONTRACT NUMBER	
				5b. GRANT NUMBER	
				5c. PROGRAM ELEMENT NUMBER	
6. AUTHOR(S) Jackson, Karen E.; Fasanella, Edwin L.; Littell, Justin D.; Annett, Martin S.; Stimson, Chad M.				5d. PROJECT NUMBER	
				5e. TASK NUMBER	
				5f. WORK UNIT NUMBER 664817.02.07.03.02.01	
7. PERFORMING ORGANIZATION NAME(S) AND ADDRESS(ES) NASA Langley Research Center Hampton, VA 23681-2199				8. PERFORMING ORGANIZATION REPORT NUMBER L-20829	
9. SPONSORING/MONITORING AGENCY NAME(S) AND ADDRESS(ES) National Aeronautics and Space Administration Washington, DC 20546-0001				10. SPONSOR/MONITOR'S ACRONYM(S) NASA	
				11. SPONSOR/MONITOR'S REPORT NUMBER(S) NASA-TM-2017-219599	
12. DISTRIBUTION/AVAILABILITY STATEMENT Unclassified Subject Category 39 Availability: NASA STI Program (757) 864-9658					
13. SUPPLEMENTARY NOTES					
14. ABSTRACT During the summer of 2015, a series of three full-scale crash tests were performed at the Landing and Impact Research Facility located at NASA Langley Research Center of Cessna 172 aircraft. The first test (Test 1) represented a flare-to-stall emergency or hard landing onto a rigid surface. The second test (Test 2) represented a controlled-flight-into-terrain (CFIT) with a nose down pitch attitude of the aircraft, which impacted onto soft soil. The third test (Test 3) also represented a CFIT with a nose up pitch attitude of the aircraft, which resulted in a tail strike condition. Test 3 was also conducted onto soft soil. These crash tests were performed for the purpose of evaluating the performance of Emergency Locator Transmitters and to generate impact test data for model calibration. Finite element models were generated and impact analyses were conducted to simulate the three impact conditions using the commercial nonlinear, transient dynamic finite element code, LS-DYNA®. The objective of this paper is to summarize test-analysis results for the three full-scale crash tests.					
15. SUBJECT TERMS Airframe structures; Explicit transient dynamic; Finite element modeling; Full-scale crash testing; Impact testing; LS-DYNA; Nonlinear					
16. SECURITY CLASSIFICATION OF:			17. LIMITATION OF ABSTRACT	18. NUMBER OF PAGES	19a. NAME OF RESPONSIBLE PERSON
a. REPORT	b. ABSTRACT	c. THIS PAGE			STI Help Desk (email: help@sti.nasa.gov)
U	U	U	UU	94	19b. TELEPHONE NUMBER (Include area code) (757) 864-9658